IMPROVEMENT OF THE CLINICAL USE OF COMPUTED RADIOGRAPHY
FOR MOBILE CHEST IMAGING: IMAGE QUALITY AND PATIENT DOSE

By

LYNN NEITZEY RILL

A DISSERTATION PRESENTED TO THE GRADUATE SCHOOL
OF THE UNIVERSITY OF FLORIDA IN PARTIAL FULFILLMENT
OF THE REQUIREMENTS FOR THE DEGREE OF
DOCTOR OF PHILOSOPHY

UNIVERSITY OF FLORIDA

2001

As my committee cochairmen, Libby Brateman and Manuel Arreola put in countless hours. I thank them for their guidance, teaching and their red ink.

As my best friend and as my personal counselor, Shannon Mihalko has been an inspiration to me throughout our friendship. Her faith in me and her willingness to listen to my dissertation woes helped me reach the finish line. When we are old, gray, purple-wearing neighbors, we will both be doctors as well.

My family has always been a source of constant and unconditional love. My parents taught me that I could be anything that I wanted to be. They have always supported me and had faith that one day I would finish with school. Throughout our lives my sister, Lisa, has helped me succeed in many areas. Her faith in me surpasses my own.

Lastly, my husband, Matt, has supported me in so many ways throughout this endeavor: physically, emotionally, and lately financially. His faith in me allowed me to persevere through countless obstacles along the way. I look forward to our life together.

TABLE OF CONTENTS

Abstract of Dissertation Presented to the Graduate School
of the University of Florida in Partial Fulfillment of the
Requirements for the Degree of Doctor of Philosophy

IMPROVEMENT OF THE CLINICAL USE OF COMPUTED RADIOGRAPHY
FOR MOBILE CHEST IMAGING: IMAGE QUALITY AND PATIENT DOSE

By

Lynn Neitzey Rill

August 2001

Chair: Libby F. Brateman
Cochair: Manuel Arreola
Major Department: Nuclear and Radiological Engineering

Chest radiography is technically difficult because of the wide variation of tissue

attenuations in the chest and limitations of screen-film systems. Mobile chest

radiography, performed bedside on hospital inpatients, presents additional difficulties due

to geometrical and equipment limitations inherent to mobile x-ray procedures and the

severity of illness in patients.

Computed radiography (CR) offers a new approach for mobile chest radiography

by utilizing a photostimulable phosphor. Photostimulable phosphors are more efficient in

absorbing lower-energy x rays than standard intensifying screens and overcome some

image quality limitations of mobile chest imaging, particularly because of the inherent

latitude. This study evaluated changes in imaging parameters for CR to take advantage of

differences between CR and screen-film radiography.

ix

Two chest phantoms, made of acrylic and aluminum, simulated x-ray attenuation for average-sized and large-sized adult chests. The phantoms contained regions representing the lungs, heart and subdiaphragm. Acrylic and aluminum disks (1.9 cm diameter) were positioned in the chest regions to make signal-to-noise ratio (SNR) measurements for different combinations of imaging parameters. Disk thicknesses (contrast) were determined from disk visibility. Effective dose to the phantom was also measured for technique combinations. The results indicated that using an anti-scatter grid and lowering x-ray tube potential improved the SNR significantly; however, the dose to the phantom also increased.

An evaluation was performed to examine the clinical applicability of the observed improvements in SNR. Parameter adjustments that improved phantom SNRs by more than 50% resulted in perceived image quality improvements in the lung region of clinical mobile chest radiographs. Parameters that produced smaller improvements in SNR had no apparent effect on clinical image quality.

Based on this study, it is recommended that a 3:1 grid be used for mobile chest radiography with CR in order to improve image quality. Using a higher kVp (+15 kVp) did not have a detrimental effect on image quality and offered a patient dose savings, including effective dose and breast dose. Higher kVp techniques should be considered when using a grid is not possible.

CHAPTER 1
INTRODUCTION

1.1 Prologue

X-ray projection radiography is the oldest clinical imaging modality in radiology. To this day, it still accounts for the largest percentage of all radiological studies performed in the US (1). In particular, chest radiography is the most frequently performed radiological exam because it aids in the diagnosis of a variety of clinical disorders, as serious as myocardial infarction or as minor as a productive cough. With the development of sophisticated imaging technologies like CT and MRI, the "chest radiograph remains the mainstay of detecting and localizing pleural abnormality" (2). For decades, a combination of fluorescent intensifying screens and photosensitive films has been used to capture these projection radiographic images. Calcium tungstate was the light-emitter initially used in intensifying screens. Later, rare-earth intensifying screens were developed and implemented into clinical use because of their quantum detection efficiency and x-ray-to-light conversion characteristics (3).

Various clinical applications impose requirements on the x-ray spectra and scatter conditions that can be utilized with these screens in order to generate images with appropriate spatial resolution and contrast for the required diagnostic tasks. For this reason, parameters that can be adjusted during x-ray projection radiography that affect the x-ray spectra and factors that affect the amount of scattered radiation reaching the phosphor are critical to the quality of the image produced with these screen-film systems.

1

Radiography of the chest is technically difficult due to the wide range of tissue attenuations in the thorax. This variation in attenuation of the chest presents difficulty in obtaining a screen-film chest image that is optimal for both the lung and the mediastinum. Some screen-film systems that contain two different types of intensifying screens have been developed solely to address this problem for chest radiography. The Kodak InSight® asymmetric film-screen system uses two different intensifying screens, a high contrast screen on the front and regular screen on the back, to capture a lung-field image on the anterior side and an image of the mediastinum on the other side of double-emulsion film (4,5).

In addition to technical difficulties related to attenuation that are common to all chest radiography, high quality mobile chest radiography is even more challenging. Mobile chest radiography is performed at the patient's bedside with a mobile x-ray unit rather than in the radiology department with fixed equipment. Automatic exposure control (AEC) systems are used to terminate x-ray exposures after a certain amount of exposure reaches the image receptor. The use of AEC produces chest radiographs with consistent film densities. The absence of AEC in mobile screen-film radiography often results in inconsistent film densities. Unfortunately, consistency is especially important for mobile chest imaging because of the reliance of the interpreter on image comparisons to assist in monitoring patient conditions.

Computed radiography (CR), which was first presented in 1981 and is now widely commercially available, represents a new approach to x-ray projection radiography. CR utilizes photostimulable phosphors (rather than fluorescence) to capture the incident x rays. Upon exposure to x rays, photostimulable phosphors trap a fraction of the incident

energy in a quasi-stable state, as a latent image. In the readout process, the trapped energy is emitted as visible light upon stimulation with a scanning laser beam. This emitted light is collected by a photomultiplier tube, which generates an electronic signal that is digitized to form a digital image. The image is subsequently processed and displayed on a workstation for interpretation.

The photostimulable phosphor most commonly used in computed radiography is barium fluorohalide, doped with europium. Photostimulable phosphors have somewhat different responses to incident x-ray spectra than screen-film combinations, because of differences in absorption coefficients that are related to their chemical compositions. The absorption efficiency of photostimulable phosphors is highest just above the K-edge of barium (37.4 keV). These phosphors are therefore more efficient at detecting lower energies than either calcium tungstate or rare-earth intensifying screens, which have K-edges of 69.5 keV and 50.2 keV, respectively. Therefore, the imaging parameters used for screen-film radiography may not be the best choices for CR.

Because of its digital nature, CR separates the image capture function from the image storage and image display functions. The appearance of a CR image is not solely determined by the radiation exposure and the detector response; rather, the appearance is modified through image processing and display (6). The interaction of the x-ray beam spectra with the CR phosphor determines the intrinsic image quality in terms of signal-to-noise ratio (SNR) and modulation transfer function (MTF) achievable in CR.

CR has the potential to overcome the problem encountered in screen-film chest radiography of displaying the widely varying tissue attenuations in the chest. Image processing capabilities such as dynamic range compression can change the mapping of

output pixel values, and therefore the contrast, in only one region of an image with a particular density level. In this way the contrast in the low-density mediastinum region of a chest CR image can be enhanced without overenhancing the lung fields (7). The dynamic range of the photostimulable phosphors used in CR is linear over an exposure range of 10^4:1 (3). Inconsistent film densities are often observed in mobile chest radiography with screen-film because of the lack of AEC. The wide latitude and automatic gain control capabilities of CR can compensate for many suboptimal choices of exposure parameters in mobile chest radiography.

Despite all the advantages of CR, radiologists at Shands at the University of Florida (UF) have noticed frequent suboptimal chest images, most notably with mobile chest radiographs of large patients. An investigation of the effect of imaging parameters including x-ray tube potential, added aluminum filtration and use of anti-scatter grids on measurements of image quality was performed in order to identify the parameters which could improve image quality in mobile chest radiography. The effects of these parameters on effective dose to patients were evaluated to assist in decisions regarding possible changes in techniques.

This study involved SNR and MTF measurements of two acrylic and aluminum block chest phantoms that were developed with x-ray attenuation and scatter properties similar to the chests of an average and a large patient. SNR and MTF measurements were performed with these phantoms while imaging parameters, such as x-ray tube potential, amount of added aluminum filtration and anti-scatter grid use, were adjusted.

Because of the separation of the image capture function in CR from image storage and display, it is not obvious that improvements in measured SNR would result in similar

improvements in the images interpreted by radiologists. The applicability of the SNR results to clinical mobile chest radiography was therefore evaluated. The parameters that improved the measured SNR of CR images were utilized in the performance of mobile chest radiographs of clinical patients. The resultant images were subjectively evaluated by radiologists and compared with images acquired with standard techniques.

1.2 X-Ray Production

In 1895 Wilhelm Roentgen discovered some mysterious rays, which became known as x rays. X rays are electromagnetic radiations that result from electronic transitions which release energy. In x-ray tubes, they may be produced by continuous radiation (bremsstrahlung) or by discrete (characteristic) radiation (8).

1.2.1 Bremsstrahlung

When a negatively-charged electron with kinetic energy T approaches a heavy nucleus, it is attracted to the positive charge of the nucleus. The attractive force of the nucleus causes the electron to slow down and change direction or stop altogether, depending on the charge of the nucleus, the energy of the electron and the distance between them. The energy that is lost by the electron ($T-T'$) is emitted in the form of an x-ray photon of energy $h\nu$. The bremsstrahlung process is shown in Figure 1-1.

The energy $h\nu$ of the x-ray photon that is produced through bremsstrahlung radiation ranges from zero (no deflection) to the total kinetic energy of the incident electron (completely stopped). The intensity of produced radiation is the energy per photon multiplied by the number of photons and has been described by quantum theory for the instance of a thin-target. The intensity of bremsstrahlung radiation from a thin

target, which allows only one interaction, with a monoenergetic beam of incident electrons is constant for all photon energies and cuts off at $h\nu_{max}=T$, as depicted in Figure 1-2 (9).
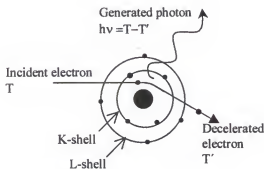
Figure 1-1 Generation of bremsstrahlung radiation by interaction between an electron and a nucleus [adapted from Ter-Pogossian, 1967 (8)]
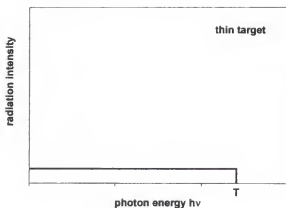
Figure 1-2 Bremsstrahlung radiation intensity as a function of photon energy for a thin target [adapted from Evans, 1985 (9)]

The spectral distribution of bremsstrahlung radiation from a thick target can then be thought of as the sum of the contributions from a number of thin-target cases at various electron energies as shown in Figure 1-3 (10). Electron energies that are incident on deeper layers of a thick target are lower in energy because of bremsstrahlung
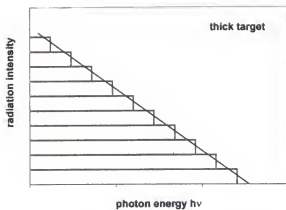
Figure 1-3 Bremsstrahlung radiation intensity as a function of photon energy for a thick target [adapted from Evans, 1985 (10)]

interactions taking place in the shallower layers of the target. Empirical data for electrons with energy T<2.5 MeV have supported this theory and shown that the total energy is proportional to the atomic number Z of the target material (10). The energy range of electrons used for x-ray production in chest radiography is well below this level, usually 120 keV or less.

1.2.2 Characteristic Radiation

Bremsstrahlung radiation is produced by interactions of impinging electrons with heavy nuclei of a target. Characteristic radiation is also produced by electrons striking a target atom, but the interaction takes place with tightly bound atomic electrons. When an impinging electron of sufficient energy collides with an atom, it can eject a tightly-bound electron from its shell, for example, the K-shell. The energy of the incident electron is used to overcome the binding energy of the ejected electron, and the remainder of the kinetic energy is shared with the ejected electron.

The shell from which the bound electron was ejected then has a vacancy, as shown in Figure 1-4. An electron from another shell, usually the next shell, rapidly fills the vacancy. For example, if a K-shell electron is ejected, an L-shell electron usually fills the vacancy. The transition produces a single x-ray photon with energy equal to the difference between the binding energies of electrons in the two shells, in this case the K-shell binding energy minus the L-shell binding energy. The vacancy that is produced in the L-shell is likewise filled by an electron from a higher shell, perhaps the M-shell, and so on. Each transition produces an x-ray photon with energy equal to the transition energy.
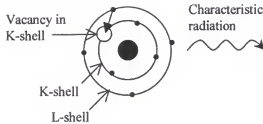
Figure 1-4 Generation of characteristic radiation as an L-shell electron fills an electron vacancy in the K-shell

The x-ray photons that are produced have energies that are specific for the shells of the target atom in which the interaction takes place and are therefore named characteristic x rays. Tungsten is the target material used for x-ray production in general diagnostic radiology x-ray tubes. Characteristic x rays produced from interactions in the K-shell of tungsten are called the tungsten K-series and include photon energies produced

by transitions from L and M subshells. The predominant characteristic radiation energies

for tungsten are shown in Table 1-1.

Table 1-1 Primary characteristic radiation energies for tungsten

Series	Line	Transition	Energy (keV)
K Series	$K_{\beta2}$	K-N	69.09
	$K_{\beta1}$	K-M	67.23
	$K_{\alpha1}$	K-L$_{II}$	59.31
	$K_{\alpha2}$	K-L$_{III}$	57.97
L Series	$L_{\gamma1}$	L$_{II}$-N$_V$	11.28
	$L_{\beta2}$	L$_{III}$-M$_V$	9.96
	$L_{\beta1}$	L$_{II}$-M$_V$	9.67
	$L_{\alpha1}$	L$_{III}$-M$_V$	8.40
	$L_{\alpha2}$	L$_{III}$-MI$_V$	8.33

The energy spectrum that is produced by electrons impinging on a target includes

contributions from both bremsstrahlung and characteristic radiation as long as the

electron energy is sufficiently high. Characteristic radiation appears as sharp lines

superimposed on the distribution of bremsstrahlung radiation. An example of an

unfiltered spectrum for a tungsten target at 100 kVp is shown in Figure 1-5.

1.3 Interaction of X Rays with Matter

In chest radiography, x rays are produced through interaction of electrons with

energies ranging from 50 to 120 kVp with a tungsten target. For adults, the range is more

limited. The x-ray energy spectrum that is produced is then attenuated as it interacts with

different types of matter including the x-ray tube exit port, aluminum filtration, the

collimation exit port, patient anatomy, the grid (if present) and finally the image receptor.

As the spectrum interacts with the matter in its pathway, it is attenuated by removal of x-

ray photons through scattering or absorption. In both cases, energy from the incident

photon beam is absorbed in the matter. The probability that an individual x-ray photon interacts with a material, and what form the interaction takes, depends on the photon energy and the material.
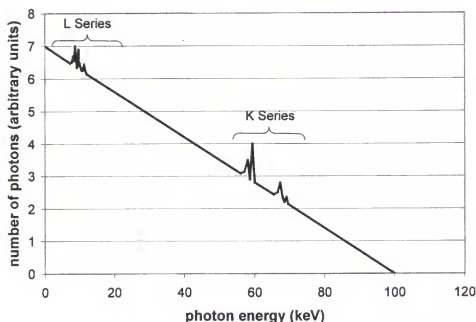
Figure 1-5 X-ray spectrum in tungsten, showing the superimposition of characteristic x-ray lines over the continuous distribution of bremsstrahlung production [adapted from Ter-Pogossian, 1967(8)]

1.3.1 Photoelectric Effect

The photoelectric effect consists of an atomic interaction of an incident photon with energy hv with a tightly bound electron, as shown in Figure 1-6. The photon is absorbed and its energy, less the energy required to overcome the binding energy of an ejected electron, is transferred to the electron in the form of kinetic energy (8,11). The photoelectric process is usually accompanied by the emission of a characteristic x ray as an outer shell electron fills the electron vacancy, as described in Section 1.2.

Eighty percent of photoelectric absorption processes take place in the K-shell, provided that the incident photon energy exceeds the K-shell binding energy (11). The probability of photoelectric interaction is highest just above the K-edge of the absorber. The probability decreases as photon energy is increased at the rate of approximately $(h\nu)^{-3}$ for materials with low atomic numbers Z (8). Characteristic x rays created by this process in low-Z material like soft tissue are low energy and are absorbed in short distances from the atom.
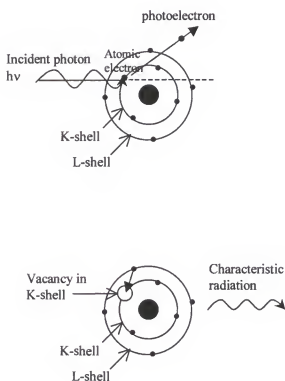
Figure 1-6 Diagram of the photoelectric effect [adapted from Ter-Pogossian,1967 (8)]

1.3.2 Coherent Scattering

Coherent scattering involves the interaction of a photon with an atom, in which the atom absorbs the photon and then reemits a photon equal in energy to the incident photon but with a new direction. Coherent scattering can take place only when the

wavelength of the incident photon is similar to atomic dimensions ~10^{-8} cm. Therefore coherent scattering takes place only for x-ray photons of the order of a few keV. These energies are not significant in chest radiography.

1.3.3 Compton Scattering

Compton scattering involves the interaction of a photon with a free electron, in which the photon gives up some of its energy to the electron and changes direction, while the electron recoils in a different direction. Compton scattering, diagrammed in Figure 1-7, obeys fundamental laws of conservation of momentum as they apply to collisions (12).
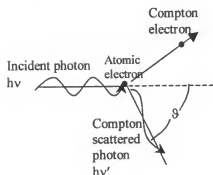
Figure 1-7 Diagram of the trajectories of the incident photon, the scattered photon and the scattering electron in Compton interactions [adapted from Evans, 1985 (11)].

The wavelength λ of the photon is related to the photon energy by the relationship $E = hc/\lambda$, where h is Planck's constant (6.625×10^{-34} J·s) and c is the speed of light (2.998×10^{8} m/s). The change in wavelength of the incident photon, when the trajectory of the scattered photon is at an angle ϑ to the incident photon direction, is given by the following equation: $\Delta\lambda = 2.43 \times 10^{-10} (1 - \cos\vartheta)$ cm (8). The maximum change in wavelength experienced by the photon is 4.86×10^{-10} cm, when the photon scatters at an angle of 180 degrees. If the wavelength of the incident photon is long with respect to this

change, as in the energy range used in diagnostic radiology, the maximum change in wavelength is only a small percentage of the energy carried by the photon. For example a 30-keV x-ray photon has a wavelength of 4.13×10^{-9} cm. The wavelength of the photon scattered at 180 degrees is 4.62×10^{-9} cm, which corresponds to a photon energy of 26.8 keV. The scattered photon differs only slightly (-3.2 keV) in energy from the incident photon (8).

The interaction that is likely to take place when an x-ray photon interacts with a diagnostic radiology patient depends on the energy of the photon. Figures 1-8a and 1-8b show the mass attenuation coefficients from photoelectric and Compton interactions when photons interact with soft tissue and with bone, respectively. For soft tissue the attenuation coefficient curves, shown in Figure 1-8a, cross at ~20 keV, which indicates that lower energy x rays, lower than 20 keV, are more likely to interact with soft tissue through photoelectric interactions, and higher energy x rays, greater than 20 keV, are more likely to interact with tissue through Compton scattering. Attenuation in bone is more likely through photoelectric interactions for photon energies up to 40 keV and through Compton scattering at higher energies higher than 40 keV (Figure 1-8b) (8).

Diagnostic radiology uses the differences in attenuation and density of tissues in patient anatomy, for example soft tissue and bone, to produce an image of the anatomy. The photoelectric effect has an advantage for diagnostic radiology image quality because photoelectric reactions are highly dependent on the atomic number of the interacting matter. Therefore, differences between adjacent tissues composed of different materials are enhanced. Although the photoelectric effect has the advantage of enhanced tissue differences, it also has the disadvantage of increased patient dose. The tissue in a
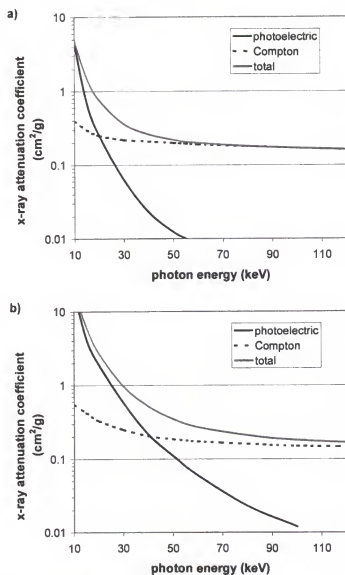
Figure 1-8 Contribution of photoelectric and Compton interactions to attenuation of x-ray photons in matter [adapted from Ter-Pogossian, 1967 (13) and Hubbell, 1981 (14)] a) soft tissue, b)bone

photoelectric interaction absorbs all of the energy from the incident photon, while in

Compton scattering only a small part of the incident photon energy is absorbed.

Compton scattering depends on the electron density of the interacting matter,

which is very similar for tissue and bone. In chest radiography, the air in the lungs has a

greatly different density than other soft tissues or bone ($\sim10^{-3}$:1). Therefore lungs

attenuate the x-ray beam much differently from other anatomical structures.

These differences among bone and soft tissue are present throughout most of the body. Chest radiography offers a particularly large range of differences in attenuations because of the presence of the lungs. It is this wide range of attenuations present in chest radiography that causes the challenge in imaging, because the required dynamic range is particularly large. Additionally, pathologic conditions can cause lungs to be filled with fluids or tissues with greatly different densities unknown to the technologist prior to the radiographic examination. The value of AEC is therefore great in chest radiography, and mobile radiography without AEC can present a difficult challenge to the technologist.

1.4 Patient Dose

The energy that is absorbed by the patient from exposure to x-ray photons contributes to patient dose. The changes that take place on the atomic level when x-ray photons interact with tissue may damage cells. Cells damaged from radiation can be repaired, modified or even killed. Cell death is considered a "deterministic" effect of radiation exposure and occurs when radiation dose is above a threshold dose level. Doses in chest radiography are typically well below the threshold for deterministic effects (15).

A cell that is modified can sometimes reproduce and result in a cancer after a prolonged latency period. The probability that a cancer will result from radiation increases with dose and is roughly proportional to the dose for levels well below the thresholds for deterministic effects. This kind of effect is called "stochastic." Stochastic effects of radiation are the reason that doses from diagnostic x-ray exams should be kept as low as possible without compromising the goal of the exam, which is diagnosis (15).

1.4.1 Dose Quantities and Units

The energy that is transferred to matter is quantified by kerma, which is an acronym for kinetic energy released in matter. The unit of kerma is the gray (Gy), defined to be 1 joule per kilogram of energy transferred. The energy transferred to charged air particles from ionizing radiation is called air kerma. Air kerma can be measured with an air ionization chamber, which collects the charge created when air molecules are ionized in the chamber. The meter is calibrated to display the collected charge in units of air kerma (Gy) or exposure (roentgen, R). One gray of air kerma is equivalent to 115 R of exposure (16). Air kerma or exposure for an examination is sometimes reported as an entrance skin exposure, measured without backscatter from the patient surface.

Absorbed dose D is the energy absorbed locally per unit mass and is also given in units of Gy. For the energies used in chest radiography, most energy is deposited locally; therefore, absorbed dose can be considered equivalent to kerma.

1.4.2 Associated Risk

The probability of stochastic effects associated with ionizing radiation depends on the type and energy of the radiation, the organ or tissue irradiated and the absorbed dose averaged over the tissue. The International Commission on Radiological Protection (ICRP) has quantified the effects of different types of radiation on the probability of stochastic effects with radiation weighting factors (w_R). The equivalent dose in a tissue, H_T, is defined as the product of the absorbed dose and the radiation weighting factor for the type of radiation involved. Radiation weighting factors are dimensionless scaling factors and when absorbed dose is presented in gray, equivalent dose is given in units of

sievert (Sv). The value of w_R for photons is equal to 1; therefore, 1 Gy absorbed dose for photons results in 1 Sv of equivalent dose (15).

Effective dose (E) is a different quantity, which takes into account the radiosensitivity of the irradiated tissues and organs. The ICRP introduced tissue weighting factors (w_T) that represent the relative contribution of each tissue or organ to the total detriment resulting from uniform irradiation of the whole body. The sum of all the weighted equivalent doses in all the irradiated tissues or organs is called the effective dose: $E = \sum_{R,T} D_{R,T} \times W_R \times W_T$. Like equivalent doses, effective doses are given in sievert. Both equivalent dose and effective dose are used in the assessment of risk from radiological exposures with the goal of keeping patient doses as low as possible without sacrificing the quality of the image (15). For many types of x-ray projection examinations, imaging techniques that improve the quality of the image also increase the dose to the patient. Therefore, a study to improve image quality in chest radiography also needs to consider the effects of these improvements on patient dose.

1.5 Projection Radiography

Projection radiography accounts for the largest percentage of all radiological studies performed in the US (1). Some technological advances have been made since the first projection radiograph was taken over a hundred years ago, but the basic concept remains the same. A fairly uniform x-ray beam interacts with the tissues in the patient's body through absorption and scatter, and then a detector placed behind the patient detects the transmitted photons as a two-dimensional view of the three-dimensional patient. The pattern formed by the transmitted photons on the detector is dependent on the interactions

that took place in the tissue. Many critical factors affect the quality of the projection image, including the incident x-ray beam energy, scatter reduction techniques used, type of detector, and other parameters such as patient size.

1.5.1 Diagnostic X-Ray Production

A primary critical parameter in projection radiography is the x-ray beam energy. The beam energy is defined by a spectrum that is determined by six major factors: the anode material, the peak x-ray tube potential (kVp), the tube current, the exposure time, the tube voltage waveform, and the type and amount of added filtration in the x-ray beam.

X-ray tubes and generators. Tungsten is the anode target material in most diagnostic x-ray tubes used for chest radiography. Tungsten is ideal as an anode material because it has both a high melting point and a high atomic number, which makes it efficient for the production of x rays. X rays are produced through bremsstrahlung and characteristic radiation, as described in Section 1.2. The beam of impinging electrons used for x-ray production is accelerated towards the target with energy equal to the instantaneous potential difference between the cathode, or filament which emits the electrons, and the anode. In conventional radiography the peak voltage applied is of the order of 50-120 kVp (8).

The x-ray source in projection radiography should be as small as possible, and the exposure time should be as short as possible, to reduce blur in the image. These conditions require a high electron flux hitting a small area (focal spot) of the anode and producing a significant amount of heat that can damage the target. The anode in modern x-ray tubes is angled, most commonly 12° to 15°, and rotated to increase the area of the target that is hit by the electron beam while still projecting a small effective focal spot

towards the patient. The length of the effective focal spot projected towards the patient

from an angled anode is equal to the actual focal length multiplied by the sine of the

anode angle.

The efficiency of x-ray production in the target, as well as the maximum energy of

the x-ray spectrum produced, is determined by the peak tube potential or kVp used to

accelerate the electrons. The effect of kVp on the x-ray spectrum produced with a

constant tube current is shown in Figure 1-9 (17). Decreasing the kVp greatly decreases

the efficiency of x-ray production and consequently the tube current and exposure time

must be increased to produce the same number of photons at a lower kVp.
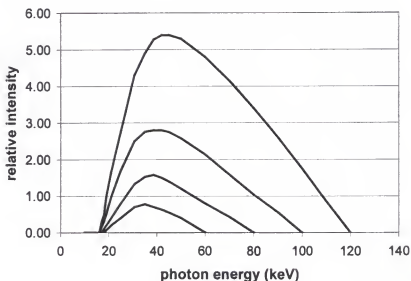
Figure 1-9 X-ray intensity as a function of kVp at the same tube current
(characteristic x rays not shown) [adapted from Bushberg *et al.*, 1994 (17)]

The flow rate of the electrons, or the number of electrons per second, impinging

on an x-ray tube target depends on the temperature of the tungsten filament that emits

them. The filament temperature is controlled by the x-ray tube current or mA. The x-ray

tube current and the x-ray tube potential are both controlled by the x-ray generator.

In this study, the effects of changing kVp and required changes in exposure time

(in order to maintain proper exposure) on image quality and patient dose were evaluated.

Most contemporary general diagnostic radiography systems use either 3-phase or constant

potential generators, which result in small amounts of ripple on the kVp waveform. The

kVp waveforms generated by the older single-phase units had much greater variation.

Figure 1-10 shows example kVp waveforms for four types of x-ray generators. The

instantaneous beam energy produced by a single-phase generator is lower and more

variable than the instantaneous beam energy produced by a three-phase or constant

potential generator at the same peak tube potential. Modern constant potential generators

produce more consistent x-ray images. In this study a three-phase, multi-pulse x-ray beam

waveform was used for images obtained with fixed x-ray units, and a high frequency

waveform with ~20% ripple was used for images obtained with the mobile x-ray unit.
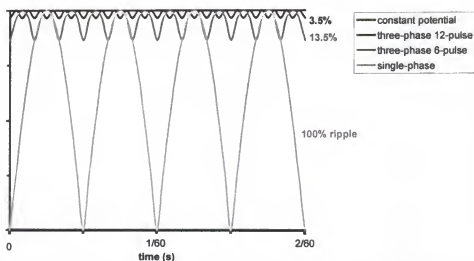
Figure 1-10 High voltage waveforms from 4 different types of x-ray generators
[adapted from Bushberg *et al.*, 1994 (17)]

Beam filtration. The x-ray spectrum that interacts with the patient undergoing an x-ray procedure is different from the spectrum that is initially produced in tungsten. This difference is because the x-ray beam is attenuated as it exits the x-ray tube by the inherent and added filtration in its path. Inherent filtration results from the thickness and material of the x-ray tube exit port, usually 1-2 mm of glass or metal as well as the collimator port. The lowest energy photons are attenuated by the inherent filtration so that essentially no photons with energies below 15 keV exit the x-ray tube and collimator (17).

Additional filtration is placed in the x-ray beam to filter low-energy x rays that contribute little to the image but contribute primarily to patient dose. Such filtration is referred to as added filtration. An example of the effect of inherent and added filtration on the tungsten x-ray spectrum is shown in Figure 1-11. Aluminum is the material commonly used for added filtration in diagnostic radiography. General-use x-ray systems
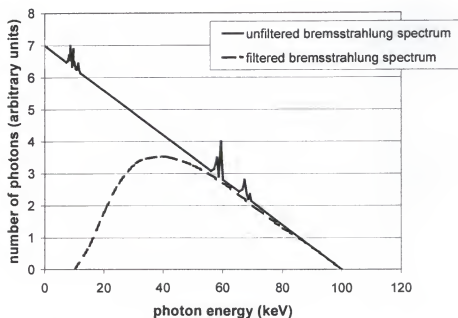
Figure 1-11 Example of the x-ray spectrum produced in a diagnostic x-ray tube at 100 kVp with tungsten target and the effect of inherent and added filtration on the x-ray spectrum [adapted from Ter-Pogossian, 1967 (8) and Bushberg *et al.*, 1994 (17)]

usually contain between 2 and 3 mm aluminum filtration added to the inherent filtration

in the x-ray tube housing (13). Figure 1-12 shows the effect of different thicknesses of

added aluminum filtration on a typical radiographic x-ray beam at 90 kVp (18).
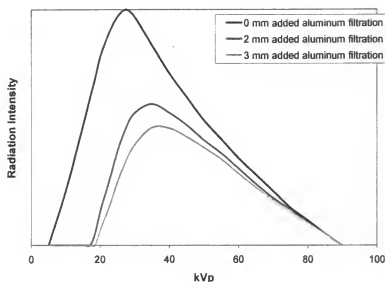
Figure 1-12 Energy spectra of 90 kVp x-ray beam with 0 mm, 2 mm and 3 mm added aluminum filtration (characteristic x rays not shown) [adapted from Curry *et al*., 1990 (18)]

The x-ray spectrum produced during projection radiography can be described in

terms of beam quality. Beam quality refers to the penetrability of an x-ray beam. A beam

containing a greater proportion of high-energy photons has higher "quality". Increasing

either the x-ray tube potential or the amount of added filtration results in an x-ray

spectrum with a higher beam quality (Figures 1-9 and 1-12). The generator waveform

affects the tube potential and consequently affects the quality of the x-ray beam similar to

changes in the kVp. A constant-potential waveform results in a higher effective energy

for the spectrum than a three-phase waveform (17).

Beam quality can be quantified by determining the half-value layer (HVL) in mm

of aluminum of an x-ray beam. The HVL of a beam is the thickness of aluminum required

to reduce the intensity of the original beam by one half. The HVL of a typical general-use

x-ray tube at 80 kVp is approximately 2.5-4.0 mm of aluminum. The HVL increases as

the beam quality increases with higher x-ray tube potential, more added aluminum

filtration or less waveform ripple. Table 1-2 lists the measured HVL in aluminum for a

three-phase, 12-pulse x-ray unit at Shands at UF. HVL values increase with kVp and

added aluminum filtration. In this study, the effects of aluminum filtration on image

quality and patient dose were studied.

Table 1-2 Measured HVL in aluminum for various kVps and amounts of aluminum
filtration in addition to the inherent and added aluminum filtration present in the x-ray
tube and collimator

kVp	Additional aluminum filtration (mm)	HVL in aluminum (mm)
60	0	2.67
80	0	3.61
100	0	4.45
120	0	5.29
60	1	3.02
80	1	4.14
100	1	5.11
120	1	5.94

1.5.2 Interactions of X Rays in the Patient

The x-ray beam produced in a diagnostic x-ray exposure is attenuated in the tissue

of the patient similar to the way it is attenuated with filtration. The remnant radiation

spectrum is lower in quantity (number of photons) and higher in quality than the incident

spectrum. Interactions of x-ray photons in the patient include absorption and scatter.

Visualization of adjacent structures in a projection radiography exam depends in part on

differences in attenuation of x-ray photons incident on each structure. The probability of

interaction depends on the attenuation coefficient and the density of the tissue, as described in Section 1.3.

Figure 1-8 in Section 1.3 showed the mass attenuation coefficients for tissue and bone as a function of x-ray photon energy. The attenuation coefficients are shown together in Figure 1-13. The difference between these coefficients is greatest at low photon energies where the photoelectric effect is dominant, because the probability of a photoelectric interaction is highly dependent on the atomic number Z of the absorber. The probability of the occurrence of a Compton interaction depends on the electron density of the material, which is very similar for most tissues. Fat, muscle and bone have electron densities of 3.34×10^{23}, 3.32×10^{23} and 3.19×10^{23} electrons per gram, respectively (13). Therefore, there is little or no difference in mass attenuation coefficients at the higher energies, where Compton scattering is most likely.
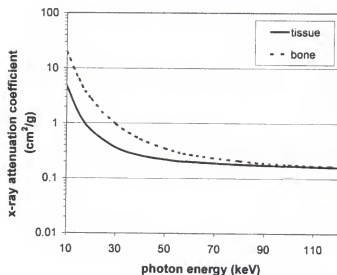
Figure 1-13 Mass x-ray attenuation coefficients for tissue and bone as a function of photon energy [values from Hubbell, 1981 (14)]

Structures can be visualized in projection radiography even though they have identical mass x-ray attenuation coefficients when there are differences in density, because of the differences in linear attenuation coefficients. Table 1-3 lists the densities of some human tissues. A lung nodule, for example, attenuates more photons than the surrounding inflated lung tissue because of its higher density, and therefore is likely to be visualized (13).

Table 1-3 Densities of human tissues [adapted from Ter-Pogossian, 1967 (13)]

Tissue	Density (g/cm^2)
Lung	0.32
Fat	0.92
Muscle and fluids	1.00
Lung tumor	0.86 to 1.05
Bone	1.65 to 1.85

The x-ray spectrum that exits the patient has been attenuated through absorption and scattering of x-ray photons. The exit spectrum includes primary radiation, which did not interact in the patient, and scattered radiation, which interacted with the patient and was scattered in a mostly forward direction. Figure 1-14 shows the primary and scattered radiation spectra exiting water phantoms of increasing thickness with a field size of 30 cm x 30 cm for incident x-ray beams of increasing kVps. The mean energies of the scattered spectra are lower than the mean energies of the primary spectra by approximately 5-10 keV. Only a small amount of the energy of an incident x-ray photon undergoing Compton scattering is lost to the electron, as described in Section 1.3. In comparison with 180° deflection, the energy transfer is even less when the photon is scattered at the angles necessary for detection by the image receptor. The decrease in the
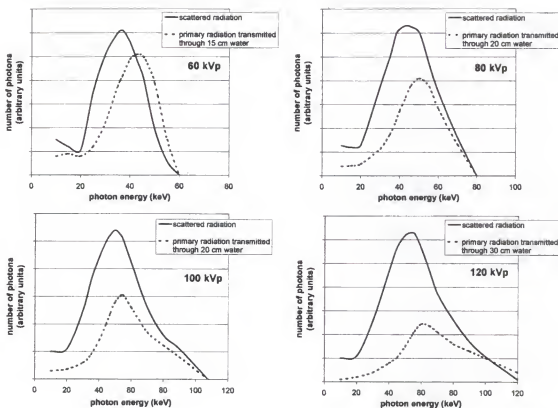
Figure 1-14 Primary and scattered x-ray spectra exiting a water phantom of increasing thickness with field size of 30 x30 cm and incident x-ray beam of 60, 80, 100 and 120 kVp [adapted from Ter-Pogossian, 1967 (19)]

mean energy of the scattered spectra is due to further attenuation in the tissue as the scattered photon exits the patient.

The amount of scattered radiation energy relative to the amount of primary radiation energy deposited at the same point in the image is called the scatter-to-primary ratio, S/P. The S/P indicates the reduction in contrast of structures at that position in the image. The S/P increases significantly with field size and patient thickness, as shown in Figure 1-15.

The S/P increases only slightly with kVp. Although the amount of scatter produced increases with kVp, the amount of primary radiation exiting the patient
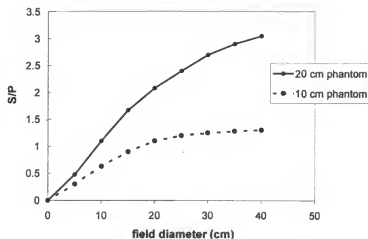
Figure 1-15 S/P values produced in two water equivalent phantoms as a function of field diameter for a 100 kVp x-ray beam [adapted from Bushberg *et al*., 1994 (3)]

increases as well, so that the ratio is not greatly affected. For example, S/P only increases

by a few percent as the kVp is increased from 80 to 120 (3).

Primary radiation contains the useful anatomic information about the patient.

Scattered radiation is not distinguishable by the detector and consequently provides

incorrect information about the structures along the primary path. A detected x-ray

photon in an image appears to have originated at the source, or x-ray tube focal spot, as

shown in Figure 1-16.
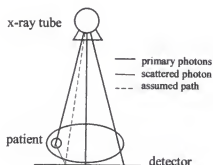
Figure 1-16 Primary and scattered radiation in projection radiography

Contrast is reduced with scattered radiation, as indicated in the diagram in Figure 1-17. A is the primary radiation that has been transmitted through the block and an overlying object, such as a disk. B is the primary radiation that has been transmitted through the block alone. The contrast without scatter is given by the equation: $\dfrac{A-B}{A}$.

Assuming that the contribution of scattered radiation S is constant in both locations, the contrast in the presence of scatter is reduced to: $\dfrac{A-B}{A+S}$. Therefore the contrast between A and B decreases as the scatter increases. The decrease in contrast due to scattered radiation can obscure structures in the image.
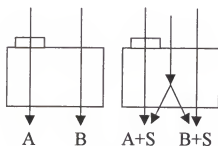
Figure 1-17 Diagram showing the effect of scattered radiation on contrast

1.5.3 Anti-Scatter Grids

Anti-scatter grids are sometimes used in projection radiography to reduce the amount of scattered radiation that reaches the imaging plate by absorbing off-angle radiation, as shown in Figure 1-18.
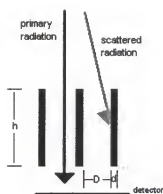
Figure 1-18 Cross-sectional diagram of a parallel anti-scatter grid.

The grid ratio is defined as the ratio between the height of the lead strips and the distance between them (h/D in Figure 1-18). Figure 1-19 shows the amount of scatter that is transmitted as a function of grid ratio for an ideal grid that does not attenuate primary radiation because of interspace material. A higher grid ratio removes more scattered radiation but requires more patient dose than a lower grid ratio. The grid line density is
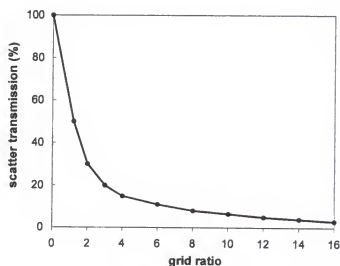
Figure 1-19 Scatter transmission as a function of anti-scatter grid ratio for an ideal grid [adapted from Bushberg *et al.*, 1994 (3)]

the number of lines per cm and can be calculated by adding the thickness of the lead strips and interspaces and taking the reciprocal ($(D+d)^{-1}$ in Figure 1-18).

The grid diagrammed in Figure 1-18 is called a parallel grid because the lead strips are parallel when viewed in cross section. Most grids that are used in radiography are focused grids in which the lead strips are angled so that they converge in space. The lead strips are thus aligned with the diverging x-ray beam so that a smaller fraction of the primary radiation is attenuated. The focal distance is the perpendicular distance between the grid and the convergent line. The focal distance should agree with the source-to-image detector distance (SID) to reduce loss of primary radiation and avoid image non-uniformity by grid cutoff.

Although grids are typically used in chest radiography with fixed units, in mobile chest radiography grids may not be used for several reasons. These reasons include the increase in exposure time that is necessary with grid use, as well as the constraints of positioning the grid parallel to the x-ray beam central ray and having the distance within the defined focal range. Lower ratio parallel grids are used at some institutions for mobile chest radiography in order to reduce the exposure and the positioning constraints. In this study, an 8:1 focused grid was used with a fixed unit for image quality measurements based on phantom imaging at Shands at UF, a 4:1 parallel grid was used for SNR measurements at the Mayo Clinic Jacksonville and a 3:1 parallel grid was used with a mobile unit for the clinical evaluation at Shands at UF.

1.5.4 <u>Image Detection</u>

The pattern of x rays transmitted from a patient undergoing projection radiography must be converted to a signal that can be detected by the radiologist's eyes. In diagnostic

radiology, photographic film has been historically used as the detector and display device, as well as a storage medium. CR is now a viable option for replacing x-ray film, and CR images are typically displayed on monitors instead. This study evaluates mobile chest radiographic imaging with CR. However, the x-ray techniques and other imaging parameters currently in use at Shands at UF were initially developed for screen-film radiography. The following discussion of screen-film imaging is therefore included for reference. The detailed discussion of CR is presented in Section 1.8.

1.5.5 <u>Screen-Film Imaging</u>

X-ray film produces an image of varying film optical densities, which are proportional to the energy deposited in the film. This process is possible by direct exposure of the film by the x-ray beam; however, direct exposure is a dose-inefficient process. It is estimated that only 5 to 6% of the energy dissipated by an x-ray beam in a photographic emulsion is used in liberating silver atoms (20).

A much more efficient way of converting transmitted x-ray energy into an image for viewing is to use a combination of a luminescent phosphor screen and a photographic film. Luminescent phosphor screens, called intensifying screens, first convert the absorbed x-ray energy into light in the visible range, and the emitted light exposes the photographic film. The density of the developed x-ray film is proportional to the amount of energy deposited in the luminescent screen. The improvement in detection efficiency of a screen-film combination over a film-only detector is called the intensification factor. This factor can vary, depending on the thickness and material of the phosphor, but it is in the range of 40 to 150 for the intensifying screens and energy range in diagnostic

radiology (3,20). The overall efficiency of the screen-film combination is the product of the detection efficiency and the conversion (x ray to light photon) efficiency.

The overall efficiency of a screen-film system is usually expressed by the speed. Manufacturers assign an arbitrary speed of 100 to their par-speed system. Then faster systems, which are more efficient at converting x-ray exposure to optical density, have higher numbers. Faster systems of the same luminescent material are thicker, require less radiation and produce noisier images.

Until the early 1970's the phosphor that was commonly used in x-ray intensifying screens was calcium tungstate, $CaWO_4$. Rare earth intensifying screens were introduced at that time and were much more efficient at both detecting diagnostic x-ray photons and converting x-ray photons to light. Therefore they could have an increased speed without introducing greater noise. Rare earth screens made with phosphors like doped gadolinium oxysulfide, $Gd_2O_2S:X$ (X is a dopant atom such as terbium), have better detection efficiency because of the K-edge energy relative to typical x-ray spectra used in radiography. This is apparent in Figure 1-20, which compares the detection efficiency of $CaWO_4$ (K-edge = 69.5 keV) and Gd_2O_2S (K-edge = 50.2 keV) intensifying screens.

The response of a screen-film system to the absorption of x-ray photons in its intensifying screen is to increase the density of the film (after developing). Screen-film response also introduces image blur not present in direct exposure imaging. The intensifying screen luminescence introduces an associated blur for each absorbed x-ray photon in the production of light. Blur is discussed later in Section 1.6.
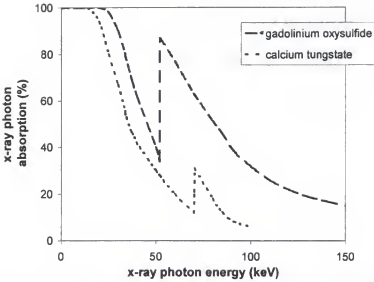
Figure 1-20 Absorption efficiency of two common intensifying screens as a function of x-ray photon energy [adapted from Ter-Pogossian, 1967 (20) and Bogucki *et al.*, 1995 (21)]

The characteristic curve of a screen-film system shows how rapidly the film density changes as a function of x-ray exposure. The characteristic curve of a screen-film system provides information about the speed, latitude and contrast characteristics of the system. Systems A and C in Figure 1-21 have similar contrast and latitude characteristics,
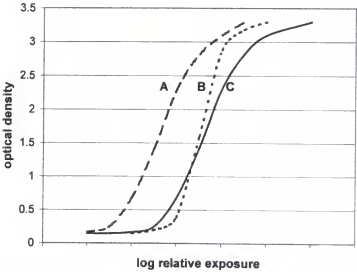
Figure 1-21 Characteristic curves for three different screen-film systems.

though System A is a higher speed system and therefore produces a similar optical density with a lower exposure. The slope of the characteristic curve indicates the contrast and latitude (dynamic range) of the system. A steeper slope indicates a higher contrast system with less latitude, such as System B in Figure 1-21. Wide latitude systems are needed in projection radiography exams where there is a large variation in x-ray exposure incident on the detector, such as chest radiography.

1.5.6 Image Interpretation

A transparent film base is used in screen-film imaging, which allows the images to be viewed by transmitting light from a viewbox through the developed film. Transmission viewing has much greater fidelity than viewing light that is reflected from film, such as for viewing photographs (3). Film densities range from 0.13 for unexposed areas to 3.5 or more for maximally exposed areas. The corresponding light transmitted through film with these densities varies from 75% to less than 0.1%, which is a wide dynamic range. A large dynamic range allows subtle differences in contrast to be visible. For example, on a chest radiograph the density is low in the mediastinum and high in the lung fields. A wide dynamic range allows subtle differences in contrast to be detectable in both areas (3).

The image that is presented to a radiologist for diagnosis contains information concerning differences in x-ray transmission through the patient. During training, radiologists acquire a mental database for pattern recognition used for interpretation of image characteristics. Experienced radiologists then use a free search approach in examining radiographs, which means that they repeatedly return to areas where suspicious findings are present or where abnormalities are found most frequently (6).

Consistency in image quality and film density is an important factor in providing the information necessary for pattern recognition and diagnosis.

1.6 Image Analysis

The quality of an image can be evaluated by examination of key image characteristics that can be quantified. The SNR and the MTF are two parameters that can be used to quantify the quality of an image and compare different imaging systems.

1.6.1 Signal

The signal produced by an object in an image is the difference in system response for that object compared with the system response in the adjacent areas of the image surrounding the object (22). For projection radiography, the system response is film optical density (OD), and the signal is the difference in the OD of the object and the OD of adjacent areas of the image. The signal is determined by two factors: the subject contrast and the detector contrast. The subject contrast is the difference in x-ray exposure between the object and the surrounding areas. Therefore, the subject contrast for a certain object size and material is affected by the x-ray beam energy. The detector contrast is the response of the system to different exposure levels and is described by the characteristic curve of the system.

1.6.2 Noise

Image noise refers to fluctuations in system response to a uniform exposure. In projection radiography, noise appears as fluctuations in film OD, which creates a textured appearance known as mottle (19). Several components contribute to the noise in an x-ray image, including quantum mottle, structure mottle and film graininess. Structure mottle

comes from irregularities in the intensifying screen. Film graininess is a result of the granularity of the film emulsion. Structure mottle and film graininess are fixed system characteristics. Quantum mottle, which results from the statistical fluctuations in the distribution of x-ray photons used to form the image, is the major contributor to radiographic noise (19).

Quantum mottle, or quantum noise, is determined by the number of x-ray photons (quanta) used to form the image. Quantum noise usually obeys the Poisson distribution. It follows that, as the number of photons used to form an image increases, the amount of quantum noise decreases. The speed of the screen-film system affects the quantum mottle in projection radiography. A faster speed system, which requires fewer x-ray photons to achieve the desirable film OD, yields a more mottled image than a slower speed system (19,22).

The overall noise in a projection radiography image includes photon noise due to radiation scattered in the patient. Factors that affect the amount of scattered radiation in a radiographic examination were discussed in Section 1.5. The noise contribution of scattered radiation is biased noise because it is dependent on the location and attenuation properties of structures in the patient. The noise contribution and contrast degradation due to scattered radiation vary for different parts of the same image.

1.6.3 Signal-to-Noise Ratio (SNR)

SNR is the ratio of the signal to the noise in an image. If the signal of an object is large compared to the noise in the image, the object is easily detected. However, if the signal is similar in magnitude to the noise in the image, the object is obscured. Figure 1-22 illustrates how an object that is initially undetectable (Figure 1-22a) can be visualized

by either increasing the signal of the object or by decreasing the level of noise in the image, thereby increasing the SNR. The SNR indicates the ability of a system to image large objects with very little contrast, i.e., the contrast resolution of the system. As the SNR of a system increases, contrast resolution improves. Therefore, SNR is a good indication of the performance of an imaging system (22).
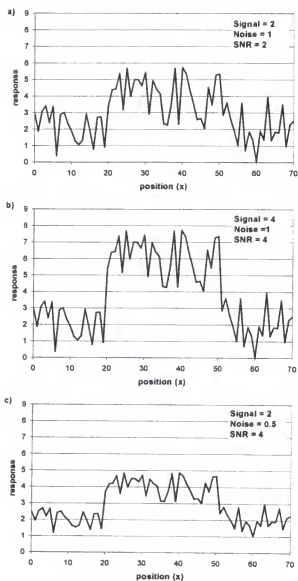
Figure 1-22 Example SNRs for a uniform disk image a) low SNR, b) increased signal, c)decreased noise

1.6.4 Spatial Resolution

Spatial resolution indicates the ability of a system to image very small objects. Physical characteristics of the imaging system, including focal spot size and screen thickness, reduce spatial resolution by introducing blur. The limiting spatial resolution indicates the smallest object that can be visualized with the system.

Focal spot blur is caused by the finite size of the focal spot, as opposed to a point source of radiation. The sharp edge of an object appears blurred in the image of the object because photons produced at one point on the focal spot intersect the image at a different point than photons produced at another point on the focal spot. The blur is called geometric unsharpness. The size of the blur is dependent on the focal spot size as well as the magnification of the object. Focal spot blur can be reduced by using a smaller focal spot size or by reducing the object magnification (19).

Screen unsharpness is due to the diffusion of the light photons that are produced by the absorption of x-ray photons in the luminescent layer of the intensifying screen. Absorption of x-ray photons in an intensifying screen can occur throughout its thickness. The light produced must travel through the screen to expose the film. Thicker intensifying screens allow the light to spread over a further distance before exposing the film, which increases the blurring of the light pattern (19). Thick phosphors are attractive because of the high efficiency of x-ray photon detection; however, there is a loss of spatial resolution associated with the thickness. Screen thickness in projection radiography is dependent on the imaging task. Thinner screens are used when detection of fine detail is important and system speed is not critical, as with extremity imaging. Blur also occurs in CR, which is discussed in Section 1-8.

In addition to the inherent system characteristics, spatial resolution in a clinical image is related to the object imaged. The sharp perpendicular edge of a thick object can be blurred by the divergence of the x-ray beam, because the incident surface of the object is imaged further laterally than the exit plane of the object. Blur in an image can also be caused by motion of the object during x-ray exposure. The amount of blur is directly related to the distance moved by the object and the magnification of the object. In projection radiography, patient motion blur is reduced by immobilizing the patient during the exam and by using high x-ray tube potential and current settings to shorten exposure times.

1.6.5 Modulation Transfer Function (MTF)

The MTF describes the resolution capabilities of an imaging system at different spatial frequencies. The MTF of a system is determined by taking the Fourier transform of the line spread function (LSF). The LSF is the response of the system to a δ-function line input. Figures 1-23-(a) and (b) show the line spread function and MTF of an ideal detector. Figures 1-23-(c) and (d) show the line spread function of a real detector, i.e., with blur added, from a finite slit input and the resultant MTF, respectively.

The overall MTF for a system includes blur introduced from each stage in the image capture process, such as the focal spot blur and the screen unsharpness. The system blur function is a convolution of the blur introduced at each stage. In the frequency domain, the system MTF is equal to the product of the component MTFs at that frequency.

$$\mathrm{MTF}_{sys}(f) = \mathrm{MTF}_1(f) \cdot \mathrm{MTF}_2(f) \cdot \mathrm{MTF}_3(f)$$
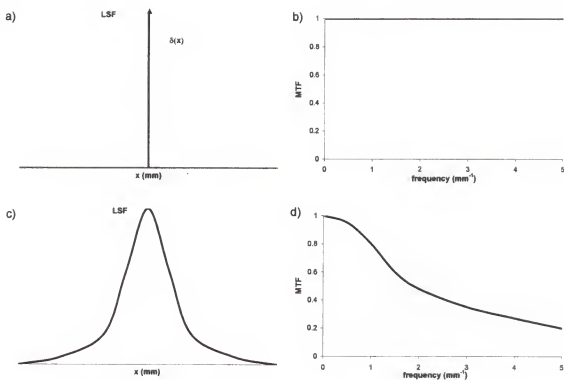
Figure 1-23. Examples of LSF and MTF.
    a) LSF of an ideal detector; b) MTF of an ideal detector; c)LSF of a real detector; d)
    MTF of a real detector. [adapted from Barnes, 1993 (23)]

Because each component MTF is less than 1 (unless edge enhancement is present in the

system), the system MTF is less than the lowest value of the component MTFs.

Consequently, the component with the lowest MTF limits the system MTF.

1.6.6 Image Quality and Patient Dose

      Many factors affect the SNR and MTF of projection radiography images. Changes

in factors that improve the SNR may be detrimental to the MTF of the image, and vice

versa. For example, a thicker phosphor layer in an intensifying screen absorbs more x-ray

photons and can improve the SNR of the resultant image at the cost of a decrease in MTF.

These factors have been balanced in the design of imaging systems to meet the needs of

various imaging tasks. Manufacturers have optimized many of these factors, such as focal

spot size, phosphor screen thickness, and screen-film system speed, for use in specific radiographic exams. The radiologic technologist controls other factors at the time of the exam, including kVp, mAs and use of an anti-scatter grid. Basic radiographic procedures are exam-dependent and may vary somewhat among institutions.

An important factor that should be taken into account when designing radiographic imaging procedures is the dose to the patient. In most cases the imaging parameters that improve the quality of an image also increase the dose to the patient. In some cases image quality might be sacrificed in order to reduce patient dose as long as successful diagnosis can be achieved. For example, the use of faster screen-film systems reduces the dose to the patient at the cost of increasing quantum noise. If the noise level is acceptable for the imaging task, faster screen-film systems should be considered. The situation is somewhat different for CR, as discussed in Section 1.8.

1.7 Chest Radiography

Chest radiography is the most common radiographic procedure, accounting for approximately 40 percent of all radiographic exams (1). There are many challenges associated with radiography of the chest, primarily due to the wide range of tissue attenuation being imaged.

Chest radiography is projection radiography of the chest region. X-ray production is performed with standard x-ray tubes used in general radiology. Areas of the body that are imaged in a chest radiograph include the lungs, heart and subdiaphragm. Large beam areas are required for chest radiography of adult patients in order to include these regions.

A significant amount of scatter can be produced in chest radiography because of the use of large x-ray field sizes, especially in the denser regions of the chest.

The mass attenuation coefficients of tissues in the chest region, other than bone, are not very different. The densities of tissues in the chest, however, vary greatly. The density of lung tissue is 0.32 g/cm^2, while the density in the heart muscle and subdiaphragm area is much greater, at 1.0 g/cm^2 (See Table 1-3). A screen-film system that has a wide latitude is needed in order to present both the lung and the heart areas of the film at acceptable film OD levels.

This wide-latitude system is necessarily low-contrast and produces a grayer-looking image, which can present a problem for contrast resolution of subtle differences in tissue attenuation. Lung nodules are a common clinical diagnosis found in one or two of every 1,000 chest radiographs (24). The visualization of fluid and nodules in the lung region and visualization of the vertebral bodies and bony structures behind the heart are common clinical tasks in chest radiography.

Because radiographic images delineate anatomical structures, the maximum exposure time is limited by patient motion that depends on the body region. Figure 1-24 shows the approximate cycle times for body functions that may cause motion artifacts when particular body regions are imaged (25). Of most concern in chest radiography is respiratory motion, which normally occurs every 2 to 6 seconds. Patients who are able are asked to stop breathing during x-ray exposures. However, patients who require mobile radiography may be unable to do so.
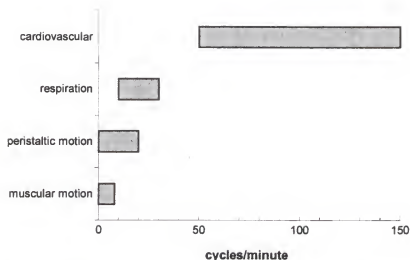
Figure 1-24 Approximate frequencies of periodic and aperiodic physiological motions. [adapted from Alfidi *et al.*, 1976 (25)]

Patient doses from chest radiography are relatively low compared with doses from other projection radiography exams. Table 1-4 shows the average entrance exposures, projection frequency and number of films per examination for chest radiography examinations of adults in the US reported by the National Council on Radiation Protection and Measurements (NCRP) (1). Entrance air kerma measured without backscatter for chest radiography projections ranged from 0.24 to 1.05 mGy. By comparison, the entrance air kerma value reported for an anterior-posterior (AP) abdomen examination was 5.76 mGy.

Table 1-4 Average entrance air kerma and number of films for chest radiography of adults in the US [adapted from NCRP Report No.100 (1)]

Projection	Entrance Air Kerma (mGy)	Average number of films per examination	
		Projection	Total
AP	0.438	0.10	
PA	0.236	0.92	1.5
LAT	0.708	0.50	
OBL	1.045	0.02	

AP refers to anterior (front) to posterior (back) beam projection
PA refers to posterior to anterior beam projection
LAT refers to lateral beam projection
OBL refers to oblique beam projection

The posterior-anterior (PA) projection is the most common projection performed, accounting for 61% of chest radiographic exposures. The AP projection, which is commonly used for mobile chest radiography, results in patient doses that are approximately double those of the PA projection. The higher doses associated with chest radiograph as compared to fixed chest radiography are primarily due to the differences in procedures.

1.7.1 Fixed Chest Radiography

Fixed chest radiography refers to chest radiography exams performed in the radiology department on mostly ambulatory patients. The most common chest radiographic projection is the PA projection, which involves the x-ray beam entering the patient's back and exiting the front. A relatively long SID is used in fixed chest radiography to reduce the magnification of structures furthest from the image detector. The distance used is commonly 183 cm (72 in), compared to an SID of 100 cm (40 in) used for most projection radiography exams. Anti-scatter grids (usually focused, high ratio grids) are used in fixed chest radiography to reduce the amount of scattered radiation that reaches the image receptor. The use of anti-scatter grids and long SIDs in fixed chest radiography require more than 10 times as much radiation output from the x-ray tube than would be required for a non-grid, 100-cm SID chest radiography examination of the same patient. High x-ray tube potentials of 120 kVp are used for fixed chest radiography in order to reduce patient motion. High kVp also decreases subject contrast. The typical x-ray tube current used for fixed chest radiography at Shands at UF is in the range of 400-600 mA. AEC is used to terminate the exposure at the proper level. The fixed chest radiography procedure is diagrammed in Figure 1-25.
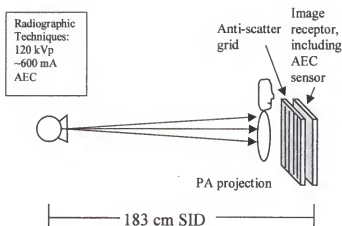
Figure 1-25 Simplified diagram of the fixed chest radiography procedure

1.7.2 Mobile Chest Radiography Procedure

Hospital inpatients often receive bedside or mobile chest x-ray examinations rather than being transported to the radiology department. Some hospitals report that the percentage of chest radiography exams performed as mobile exams is growing because of an increase in acuteness of illness and a rise in surgical procedures. At one institution this percentage increased by 17% between 1982 and 1988 (26). Because mobile chest examinations require that the imaging equipment be brought to the patient, there are many differences in techniques from fixed chest radiography. In addition to differences in the imaging equipment used for mobile chest radiography, the patient population is also different. Mobile chest radiographs are often performed on patients in hospital intensive care units who have more severe illnesses than the normal population. Positioning of the x-ray unit and the image receptor is often difficult because of the presence of air mattresses and other patient care equipment. In addition, the respiration of many patients in intensive care unit may be assisted by mechanical ventilation support so that breath suspension is not possible.

Patients undergoing mobile chest radiography are imaged while lying in their hospital beds. The x-ray tube is positioned above the patient and the image receptor placed beneath them to produce an AP projection chest radiograph. Mobile chest radiographs are commonly performed at an SID of 100 cm, in part because of practical limitations involved with positioning the equipment and also due to the limitations of the x-ray unit, which typically has a fixed x-ray tube current.

Unlike fixed units, mobile units do not have separate controls for tube current (mA) and time: for the mobile units at Shands at UF (GE AMX-4), the tube current is fixed at 100 mA, as compared with a tube current of ~600 mA used for fixed chest radiography. A typical mAs setting for mobile chest radiography is 2 mAs. For a mobile x-ray unit with a fixed x-ray tube current of 100 mA, an exposure time of 20 ms is required. An increase in mAs directly increases the exposure time by the same factor.

Mobile chest radiographs are performed at lower kVp (typically 80 kVp for an average-sized adult) than fixed chest radiographs. Historically, lower kVp was used because of system limitations of mobile x-ray units. Mobile chest radiographs are still performed at low kVp settings because of the enhancement of tissue contrast with low energy x-ray photons (see Section 1.3), superimposed on more scatter because of not using a grid. Enhancing subject contrast is especially important in the diagnosis of intensive care patients who more often have abnormal pathology.

Mobile x-ray units typically do not have AEC. Radiologic technologists must manually set the mAs, which can often result in over- or underexposed images, particularly because the patient thickness does not account for fluids in lung tissues, which may or may not be present. Consistent film density is difficult to achieve using

manual technique settings. Many intensive care patients undergo mobile chest radiography daily. Consistent film density is important for comparison of these images and diagnosis of changes in patient condition.

Patient motion artifacts are seen in mobile chest radiography more often than in fixed chest radiography, in part because of a more severely ill patient population and in part because of the low x-ray beam intensities and longer exposure times. Many of the patients undergoing mobile chest radiography use ventilation-supported respiration. Although these patients cannot voluntarily stop breathing for an x-ray exposure, the exposure can be timed to reduce patient motion due to respiration. Figure 1-26 shows the volume of air in the lungs during ventilator-supported respiration. Cycle times vary from 4 to 5 s for commonly used modes of mechanical ventilation (27). During the last fifth of the cycle, which corresponds to 0.8 to 1.0 s, the lung volume is approximately constant at full inspiration. An image exposed during this period will have minimal patient motion due to respiration. Exposure times in mobile chest radiography are generally short enough to avoid patient motion artifacts, but exposures must be accurately timed.
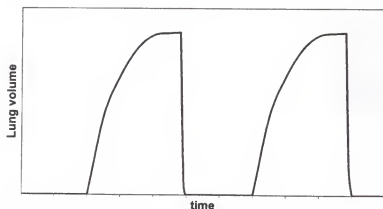
Figure 1-26 Lung volume as a function of time during mechanical ventilation [adapted from Fauci *et al.*, 1998 (27)]

Mobile chest radiographs are performed at many institutions, including Shands at UF, without the use of an anti-scatter grid. Focused, high ratio anti-scatter grids can be very sensitive to positioning errors, which can result in the loss of primary radiation and create a non-uniform image or grid cutoff. Therefore, parallel anti-scatter grids of low grid ratio are sometimes used instead. Another consideration for grid use in mobile chest radiography is the increase in exposure necessary to maintain film density, which would necessitate an increase in radiographic techniques (kVp and mAs) and patient dose. Low ratio grids do not require as much an increase in exposure as high ratio grids. A diagram of the procedure that is used for mobile chest radiography is shown in Figure 1-27.
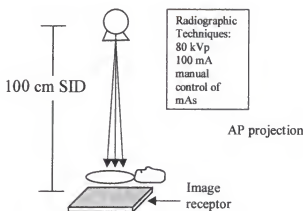
Figure 1-27 Simplified diagram of the mobile chest radiography procedure

Patient doses in mobile chest radiography are higher than doses in fixed chest radiography for two reasons. First, the differences in procedure, including use of a lower energy x-ray beam and therefore higher mAs and use of a short SID, increase the entrance air kerma incident on the patient. Second, calculations of effective dose include higher contributions from radiosensitive organs like the breast, which absorb much more x-ray energy when the AP projection is used rather than the PA projection.

1.8 Computed Radiography

Computed radiography is a projection imaging modality similar to traditional screen-film radiography. Identical x-ray equipment is used; however, with CR, the screen and film are replaced with a photostimulable phosphor plate. The energy from the incident x-ray pattern is stored in the CR plate that can be scanned at a later time to generate a digital x-ray image.

In 1980, Fuji Photo Film (Tokyo, Japan) patented the process of using photostimulable phosphors to record x-ray images. Some of the incident energy of the x rays is trapped in the photostimulable phosphor in a quasi-stable state. The trapped energy is emitted as visible light when stimulated with a scanning helium-neon laser beam. The light emitted is collected by a photomultiplier tube (PMT) which generates an electronic signal that is digitized to form the digital image. The first CR system was commercialized by Fuji in 1983.

Other manufacturers, including Philips, Toshiba, Dupont and Siemens, have marketed CR systems that make use of the patented Fuji technology including image processing software. More recently, Kodak and Agfa have marketed their own CR systems with some unique design features and software. These systems are still based on the basic photostimulable phosphor technology developed by Fuji. CR systems have only been in wide-spread use for the last 5 years.

In 1995, Shands Hospital at UF acquired two Kodak Ektascan 400 CR systems (Kodak Health Imaging Sciences, Rochester, NY) for bedside radiography. In 1999 the first of several Agfa ADC Compact CR units (Agfa-Gevaert, N.V.) were installed at Shands at UF in the main radiology department and at remote sites. All images are

interpreted by radiologists in soft copy form at CEDARA workstations using VR Report software (Cedara Software, Inc., Toronto, Canada).

In contrast to screen-film radiography, which uses film as a medium for image capture, image processing, image storage and image display, CR performs these functions separately. Though the image capture process has many similarities to screen-film radiography, CR produces a digital image providing for the processing, storage and display of images to be performed by computer software and hardware.

1.8.1 Image Capture

The capture of the image in CR is similar to that of screen-film radiography, except that a digital image file is created. Though identical x-ray equipment is used, in CR, the screen and film are replaced with a photostimulable phosphor plate. The energy from the incident x-ray pattern is stored in the CR plate that is scanned at a later time with a laser beam to stimulate the phosphor to emit the stored energy as light. The light is collected by a PMT that produces an electric signal proportional to the light collected. This signal is digitized to generate a digital x-ray image. Laser scanning does not release all of the energy stored in the plate. Therefore, the plate must be erased with a bright white light before reuse. Figure 1-28 shows a simplified diagram of the path of a CR plate in CR.

Photostimulable phosphors. The photostimulable phosphors used in CR plates are made of europium-activated barium fluorohalide ($BaFX:Eu^{++}$), where the halide element X is usually either bromine or iodine. Barium fluorohalides have the ionic crystal structure shown in Figure 1-29 (28). Europium doping creates luminescence centers (F-centers) in the phosphors by replacing some of the barium in the crystal. An F-center
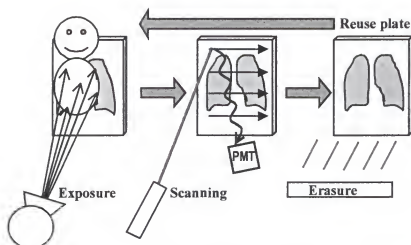
Figure 1-28 Simplified diagram of the path of a CR plate in CR [adapted from Kato, 1991 (28)]

consists of an electron trapped in a halogen ion vacancy in an ionic crystal. F-centers absorb light of specific wavelengths.
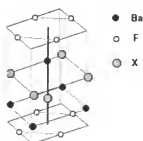
Figure 1-29 Ionic crystal structure of barium fluorohalides [adapted from Kato, 1991 (28)]

When x-ray energy is absorbed, electrons are excited to the conduction band as illustrated in Figure 1-30, generating electron-hole pairs in the crystal. Some of the halogen ion vacancies in the crystal trap these electrons to create metastable F-centers. Some of the Eu^{++} ions are ionized to Eu^{+++} ions by capturing holes (i.e., losing electrons).

The trapped electron-hole pairs store the absorbed x-ray energy as a latent image. During the readout, the phosphor is scanned with visible light having a wavelength absorbed by the F-center. The absorption of the light excites the trapped electrons to the conduction band. Once in the conduction band the electrons are again either trapped, or they migrate to the Eu^{+++} ions. The Eu^{+++} ions that combine with migrating electrons are converted to the Eu^{++} state, releasing the stored energy as luminescence (28).
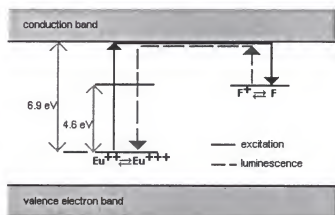
Figure 1-30 Energy level diagram of excitation and luminescence process [adapted from Kato, 1991 (28)]

The barium in the CR plate has a lower K-edge energy than the gadolinium in the standard rare-earth intensifying screens (37.4 keV, compared to 50.2 keV). Figure 1-31 shows the absorption efficiency for both a CR phosphor and a standard intensifying screen (21). An incident photon with energy slightly greater than the K-edge of an element is much more likely to interact with that element through photoelectric absorption, as described in Section 1.3. CR phosphors are more efficient than intensifying

screen phosphors at absorbing lower energy x rays in the region between 37.4 and 50.2 keV.
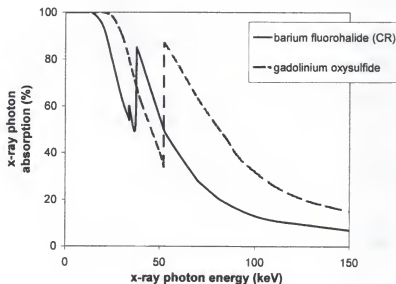
Figure 1-31 X-ray photon absorption efficiency for two phosphors as a function of photon energy [adapted from Bogucki *et al.*, 1995 (21)]

Scattered radiation that reaches the imaging plate has a slightly lower average energy than the primary radiation that did not interact in the patient. Figure 1-32 shows the absorption efficiency of each type of phosphor with the scatter and primary radiation spectra exiting a 20 cm water phantom from an 80 kVp x-ray beam. Gd_2O_2S intensifying screens take advantage of the difference in effective energies of primary and scattered radiation in order to absorb primary radiation preferentially. Note that the scattered x-ray spectrum in Figure 1-32a is centered below the K-edge of Gd_2O_2S. Because CR phosphors are more efficient at absorbing low-energy x rays, it is likely that they are more susceptible to scattered radiation from an 80 kVp incident x-ray beam. Both scattered and primary spectra from an 80 kVp x-ray beam are absorbed efficiently in the BaFBr phosphor used in CR, see Figure 1-32b.
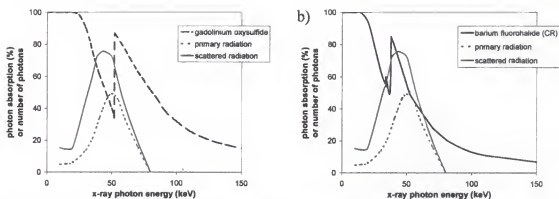
Figure 1-32 Primary and scattered x-ray spectra transmitted from a 20 cm-thick water phantom at 80 kVp and x-ray photon absorption efficiency curves of phosphors a) gadolinium oxysulfide, and b) barium fluorohalide
[adapted from Ter-Pogossian, 1967 (19) and Bogucki *et al.*, 1995 (21)]

The dynamic range of photostimulable phosphors is $10^4:1$, compared with $10^2:1$ for conventional screen-film radiography. Figure 1-33 shows the characteristic curves for CR and a typical screen-film system. CR has a wider latitude than screen-film radiography. At low values of air kerma to the CR plate, below ~0.04 mGy, the noise or mottle in the image is directly related to the amount of energy deposited in the plate (28).
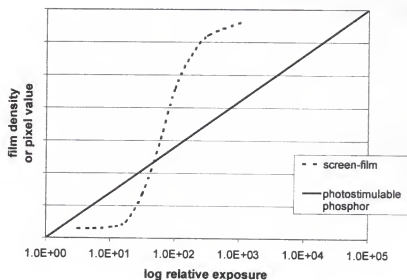
Figure 1-33 Characteristic curves for a photostimulable phosphor used in CR and a screen-film system [adapted from Bushberg *et al.*, 1994 (3)]

High exposures can be used to improve the image quality of CR images by reducing the amount of quantum mottle present in the image, with no risk of producing a dark image.

The minimum exposure required to create a quality image is not determined by a characteristic curve but by the amount of image noise that can be tolerated by the radiologist. In other words, an underexposed CR plate might yield an image with an adequate density and contrast but it would also have a greater amount of quantum mottle, which would degrade the detectability of low-contrast objects in the image.

Current commercially-available CR systems have a system speed of approximately 300 relative to Kodak Lanex (rare-earth) screen-film systems (29). Therefore, radiographic techniques used with 400 or 600 speed screen-film systems need to be increased for use with CR in order to keep the noise-level constant. For example, a facility that uses a 600-speed screen-film system for general radiography needs to double existing exposures to achieve approximately the same image quality with a CR system.

Scanning laser. During the CR scanning process, photostimulable phosphors are scanned with a laser beam to stimulate the phosphor to release the stored energy from the x-ray exposure in the form of light. The light emitted during scanning has a different wavelength from the light used for stimulation. Figure 1-34 shows the emission and stimulation spectra of the $BaFX:Eu^{++}$ phosphors. The phosphors are stimulated most efficiently by light around 600 nm, and the light released is around 400 nm. The helium-neon laser, with wavelength of 633 nm used for stimulation of the phosphor, is therefore close to ideal.

Phosphor plates are scanned raster fashion with a laser spot of ~100 μm at the plate (21). The luminescence is emitted in all directions, so a collector is used to focus the
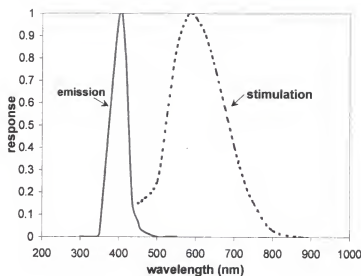
Figure 1-34 Emission and stimulation spectra of BaFX:Eu^{++} phosphors [adapted from Bogucki *et al.*, 1995 (21)]

light onto a PMT. An optical filter, used in front of the collector to prevent reflected laser light from reaching the PMT, allows only the 400 nm fluorescence to be detected.

Photomultiplier tubes. PMTs produce a pulse of electrical current when stimulated by very weak light signals (30). The inside front surface of the glass entrance of the PMT is coated with a photoemissive substance that ejects electrons, typically one to three electrons per ten light photons, when struck by photons of visible light. A series of metal plates called dynodes, coated with a material having relatively high secondary emission characteristics, is located throughout the PMT. The first dynode has a positive voltage relative to the photocathode. Each additional dynode has an incremental increase in voltage relative to the previous dynode. Electrons emitted at each stage are attracted to the next stage and the electron multiplication process is repeated until many electrons are collected at the anode. The total electron multiplication factor is very large. For a ten-stage tube with average multiplication factor 6 at each dynode, the multiplication factor is

6^{10} or 6.05×10^7. The amount of current produced is proportional to the intensity of the light signal incident on the photocathode and thus also proportional to the amount of energy deposited by the radiation event in the phosphor.

PMTs require a very stable high-voltage supply because the electron multiplication factor is very sensitive to dynode voltage changes. Typically a 1 percent increase in the high voltage applied to the tube increases the amount of current collected at the anode by about 10 percent. PMTs are sealed in glass, and air is evacuated (30).

Digitization. The electronic signal produced by the PMT is proportional to the light released from the CR plate. This signal is digitized to create an image file. For current CR systems, 35 cm x 43 cm imaging plates produce a digital image with a matrix size of 2048 x 2500, corresponding to a pixel size of 0.17 mm on a side. A 12-bit pixel depth is used, which provides pixel values ranging from 0 to 4096.

1.8.2 Image Storage

CR images are 16-bit DICOM image data files. Image data files, produced by 35 cm x 43 cm imaging plates, are approximately 10 Mbytes in size. Data files can be sent via Ethernet to several destinations. Although images can be printed by a laser printer when necessary, image interpretation is typically from a monitor. Soft copy images are normally sent both to radiologist workstations for image interpretation and to an image archive for long-term storage. Images can be retrieved from the long-term archive at a later time for image comparisons.

1.8.3 Image Processing

A CR digital image file is processed in order to maximize the information given to the viewer. Image processing functions that are common to all systems include

applying a lookup table (LUT) for optimal display and applying an edge-enhancement algorithm. Some image processing operations, including collimation detection, definition of the anatomic region and tone scaling, are controlled by internal parameters that are derived from the actual image data. Some image processing operations, such as LUT application and edge enhancement, are controlled by parameters that vary according to the examination information entered when the CR imaging plate is scanned (7). Figure 1-35 shows a simplified flow diagram of the image processing operations in current CR systems.
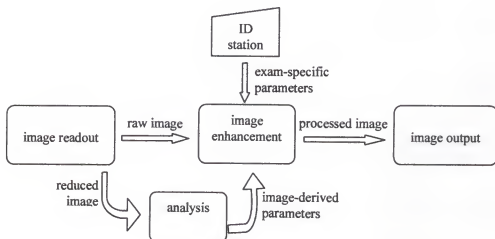
Figure 1-35 Generalized CR image processing flow diagram [adapted from Vuylsteke *et al.*, 1997 (7)]

Most CR systems use a reduced version of the original images (larger pixels with averaged values) as input to determine internal parameters. Some earlier generation CR systems use a preliminary scan of the CR plate with a low intensity laser beam as input to derive parameters. These parameters are used for the critical tasks of defining the anatomic region and collimation borders so that the relevant data are used to determine density levels and dynamic range.

The type of radiographic exam that was performed is entered at the CR ID station before the imaging plate is scanned. Some parameters of image processes are exam dependent. Two important processes which depend on the designated exam are the application of an LUT and unsharp mask enhancement.

LUT application determines how the image is displayed. An LUT maps the pixel values of the image to display pixel values. LUTs can map linear image data to output values that approximate the appearance of a screen-film image of the same region.

Some projection radiography images, for example chest images, contain a range of exposures that may be too large to display all regions with sufficient contrast resolution. Some CR systems use processing methods for contrast equalization (e.g., Fuji's Dynamic Range Compression (DRC)). A blurred version of the image is first created using a very large kernel size (up to 255 pixels). The blurred image is added to the original image using weighting factors that vary, depending on the density (average pixel value) of the image region. The dynamic range is compressed according to the equation: $Y = X + f(\overline{X})$, where Y is the pixel value after DRC, X is the original pixel value and $\overline{X}$ is the pixel value of the blurred image. This method can adjust the density and contrast in high or low signal areas of an image without changing other areas (7). This contrast equalization procedure is used on Fuji CR images of the chest to improve the visibility of structures in the low-density areas of the image, e.g., the mediastinal region.

Unsharp mask enhancement is an image-processing tool that is used by CR systems to enhance edges in a CR image. The process first involves creation of an unsharp mask image by a moving average (convolution) operation with a two-dimensional kernel. This kernel is a collection of an odd number of pixels, which is

symmetric about the center pixel and is approximately circular or diamond in shape. The pixel at the center of the kernel takes on the average gray-scale value of the entire kernel in that position. Then the kernel is moved to the next pixel and the averaging procedure is repeated to form the unsharp mask image.

The unsharp mask image is then subtracted from the original image to obtain a difference image which contains the high spatial frequency content of the image. Then the difference image is multiplied by an enhancement or "boost" factor and added back to the original image. The bandwidth of the spatial frequency band to be enhanced is determined by the size of the filter kernel that is used for creating the unsharp mask image. The unsharp masking MTF is shown in Figure 1-36. Note that the MTF values are greater than 1, so that the measured MTF for an unsharp mask enhanced image can be greater than 1 at some frequencies. Unsharp masking generally enhances features that are smaller than the kernel size (7). Unsharp masking kernels typically used in CR vary in size from 3 to 151. Kodak uses a kernel size of 75 for chest images (21).
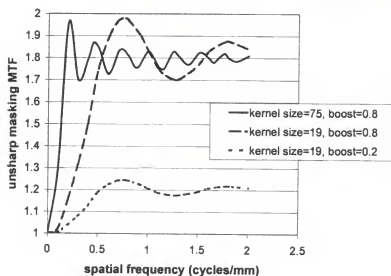
Figure 1-36 MTF for unsharp mask enhancement used in CR systems [adapted from Bogucki *et al.*, 1996 (21)]

1.8.4 Image Display

CR images are displayed at workstations for radiologist interpretation. The use of softcopy display for interpretation allows manipulation of the appearance of images, most commonly through adjustments of the display window and level. Many other tools are available, including magnification, sharpening or smoothing algorithms and LUT inversion (black and white reversal). These tools can be useful for such tasks as optimizing visualization in the mediastinum by increasing the contrast of the image display. Display adjustments may be able to compensate to a certain degree for sub-optimal image quality.

The effect of softcopy display for interpretation of digital images is not well understood. During training, radiologists acquire a mental database of patterns in images used for image interpretation. The ability to change the appearance of CR images greatly expands the range and amount of information that is included in the acquired database of normal images (6). Consequently, pattern recognition becomes difficult and the time required for interpretation longer. The display of CR images is an area that requires further research.

1.8.5 CR Image Quality

As described in Section 1.6, the SNR and MTF are two parameters that can be used to quantify image quality.

SNR. The SNR of a system, discussed in section 1.6, is an indicator of contrast resolution or the detectability of large, low contrast objects. The SNR of a digital image can be manipulated through image processing. For example, unsharp mask enhancement, which is used to enhance edges in digital images, reduces SNR values by 40% when

kernel sizes of ~80 pixels (half-value width of 10) are used to produce the unsharp mask image rather than kernel sizes of ~8000 pixels (half-value width of 100) (31). The matrix size of the kernel used to generate the blurred image determines the spatial frequencies that are enhanced. Using a small matrix size causes the overall SNR to decrease because the noise is enhanced more than the image signal. Noise has high-frequency components that are preferentially enhanced by a small mask (21).

As with screen-film imaging systems, the noise of a CR image has several contributing factors, including x-ray quantum mottle, structure noise from the imaging plate and the readout process and quantum noise from the photostimulable luminescence. Figure 1-37 shows the relationship of noise in a CR image to x-ray exposure for standard CR plates (28). At lower exposure levels, the noise standard deviation curve is a straight line, which indicates that the noise at these levels is due primarily to x-ray quantum fluctuations. At higher exposures, the curve levels off, indicating that the structure mottle
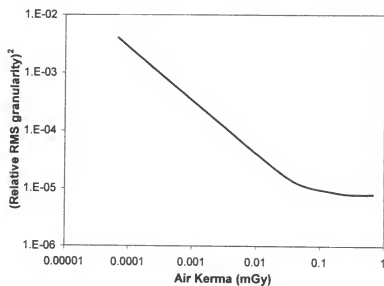
Figure 1-37 Noise standard deviation as a function of x-ray exposure for CR
[adapted from Kato H, 1991 (28)]

from the imaging plate is more predominant. At air kerma levels to the CR plate below ~0.03 mGy, the noise, or quantum mottle in the detected image is related to the number of x-ray photons incident on the detector (28). Air kerma levels to imaging plates in CR are generally of the order of 10 μGy, which is well below this level.

MTF. System MTF using CR includes most of the same components as screen-film radiography, as described in Section 1.6, with the exception of the image receptor and the display. Components which contribute to the system MTF of CR include: the profile of the scanning laser beam, the diffusion of light in the phosphor screen, the decay of the stimulated luminescence and the digital sampling rate or pixel size. The laser beam profile is Gaussian in shape and has a width of approximately 100 μm (23). The diffusion of light in the CR plate phosphor is similar to diffusion in conventional intensifying screens. High-resolution CR plates reduce this diffusion by using phosphors with half the thickness of standard CR plates, similar to high-resolution intensifying screens. At higher spatial frequencies, i.e., above 5 lp/mm, the MTF response is dominated by the readout laser spot size. As with screen-film radiography, blur due to the finite size of the focal spot and patient motion are part of the overall MTF for a CR image. Image processing techniques that are used in CR, including unsharp mask enhancement, can also affect the MTF by enhancing the contrast of certain frequencies in the image as described earlier in this section. The display monitor also has its own MTF, different from a viewbox used in screen-film radiography. Parameters affecting display MTF include the resolution of the monitor or display pixel size.

Figure 1-38 shows the MTF for both a typical screen-film system and for a CR system. The spatial frequency at which the MTF falls to 0.04 or 4 % is called the limiting

spatial resolution (23). Although the screen-film system and the CR system shown in Figure 1-38 respond similarly at low frequencies, the screen-film system has higher limiting spatial resolution.
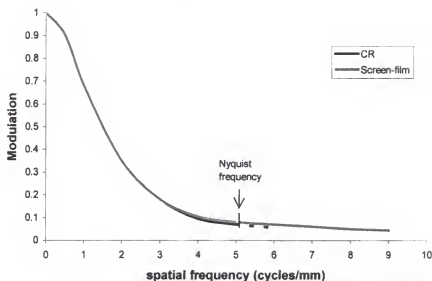
Figure 1-38 Modulation transfer function for a CR system and for a screen-film system [adapted from Cowen *et al*., 1993 (32)]

The limiting spatial resolution for CR is inferior to that of screen-film radiography. The limiting resolution is restricted by the matrix size of the digital image file or by the number of pixels/mm that are in the image. The limiting spatial resolution is one-half of the sampling rate or Nyquist frequency of the image. The limiting resolution of a digital system may be difficult to measure due to the presence of aliased bars at frequencies above the Nyquist frequency (32). The dashed line in Figure 1-38, above 5 cycles/mm, indicates the presence of aliasing.

CR limiting spatial resolution improves when smaller plate sizes are used because of an approximately fixed matrix size. Table 1-5 shows the Nyquist sampling rate for several CR plate sizes for three CR systems.

Table 1-5: Resolution capabilities of CR imaging plates

Plate Size	CR Manufacturer	Matrix Size	Approximate Pixel Size (mm)	Nyquist sampling rate (cycles/mm)
	Kodak	1792 x 2392	0.10	5
18 cm x 24 cm	Agfa	1792 x 2392	0.10	5
	Fuji	1770 x 2370	0.10	5
	Kodak	2048 x 2500	0.12	4.2
24 cm x 30 cm	Agfa	2048 x 2500	0.12	4.2
	Fuji	1576 x 1976	0.15	3.3
	Kodak	2048 x 2500	0.17	2.9
35 cm x 43 cm	Agfa	2048 x 2500	0.17	2.9
	Fuji	1760 x 2140	0.20	2.5

1.9 Use of CR for Mobile Chest Radiography

As discussed in Section 1.7, mobile chest radiography with screen-film is often challenging and can produce suboptimal chest images. A major problem with screen-film chest imaging in general is the lack of adequate latitude and contrast resolution to display subtle differences in density over the wide range of density levels found in chest radiography (22). Another problem found in mobile chest radiography is the production of chest images with inconsistent film density levels because of the lack of AEC for most mobile x-ray units.

CR has the potential to overcome the problem in screen-film chest radiography of optimally displaying the widely varying tissue attenuations in the chest. Image processing capabilities such as dynamic range compression can change the mapping of output pixel values, and therefore the contrast, in only one region of an image with a particular density

level. In this way the contrast in the low-density mediastinum region of a chest CR image can be enhanced without overenhancing the lung fields (7). CR is very well suited for mobile chest radiography because of its wide latitude and automatic gain control, which compensate for inappropriate exposures. Despite all the advantages of CR, radiologists at Shands at UF have noticed frequent suboptimal chest images, most notably with mobile chest radiographs of large patients.

1.10 Goal of This Dissertation

The interaction of the x-ray beam spectra with the CR phosphor determines the intrinsic image quality in terms of the SNR and MTF achievable in CR. The wide exposure latitude of photostimulable phosphors and the image processing capabilities inherent to digital systems make CR an imaging modality with superb image quality features. Because of these features, the appearance of CR images is not solely determined by the radiation exposure and characteristic curve of the detector but may be modified by manipulation of the digital CR data.

The goal of this dissertation was to identify the imaging parameters that improve image quality in mobile chest radiographs performed with CR and to assess their impact on patient dose. An investigation of the effect of imaging parameters including x-ray tube potential, added aluminum filtration and use of anti-scatter grids on measurements of image quality in terms of SNR and MTF was performed in order to determine the intrinsic image quality achievable in CR. The effects of these parameters on effective dose to patients was evaluated to assist in decisions regarding techniques chosen.

This study involved SNR and MTF measurements of two acrylic and aluminum block chest phantoms that were developed with x-ray attenuation and scatter properties similar to the chests of an average and a large patient. Image quality measurements indicated the performance of the CR system in mobile chest radiography.

Because of the separation of image capture in CR from storage and display, the effects of improvements in measured SNR on the interpretation of images by radiologists were not obvious. The applicability of the SNR results to clinical mobile chest radiography was therefore evaluated. The parameters that affected the measured SNR of CR images were utilized in mobile chest radiography for clinical patients. The quality of the resultant images was then subjectively evaluated by radiologists in comparison with images acquired at standard techniques.

CHAPTER 2
HYPOTHESES

The goal of this dissertation was to identify the imaging parameters that improve image quality in mobile chest radiographs performed with CR. An investigation of the effects of imaging parameters including x-ray tube potential, added aluminum filtration and use of anti-scatter grids on measurements of image quality in terms of signal-to-noise ratio (SNR) and modulation transfer function (MTF) was performed in order to determine the intrinsic image quality achievable. The effects of these parameters on effective dose to patients were evaluated to assist in decisions regarding technique changes. The resultant image quality measurements were evaluated with the goal of providing clinically useful guidelines for mobile chest radiography image acquisition with CR. The applicability of the results to clinical mobile chest radiography was also evaluated.

Hypothesis 1.A: The peak x-ray tube potential (kVp) used with CR for performing a mobile chest examination of a typical patient should be lowered from current clinical settings to improve SNRs, although there is an increase in patient dose.

Hypothesis 1.B: The amount of aluminum filtration added to the x-ray beam used with CR for performing a mobile chest examination of a typical patient should be decreased from current clinical settings to improve SNRs, although there is an increase in patient dose.

Hypothesis 1.C: The use of an anti-scatter grid for performing a mobile chest examination of a typical patient with CR does not significantly improve SNRs but does increase patient dose.

Hypothesis 1.D: The measured MTF of a mobile chest examination for a typical patient is not affected by changes in the kVp, added filtration or use of an anti-scatter grid.

Hypothesis 2.A: The peak x-ray tube potential (kVp) used with CR for performing a mobile chest examination of a large patient should be lowered from current clinical settings to improve SNRs, although there is an increase in patient dose.

Hypothesis 2.B: The amount of aluminum filtration added to the x-ray beam used with CR for performing a mobile chest examination of a large patient should be lowered from current clinical settings to improve SNRs, although there is an increase in patient dose.

Hypothesis 2.C: An anti-scatter grid should be used for performing a mobile chest examination of a large patient with CR in order to improve SNRs, although there is an increase in patient dose.

Hypothesis 2.D: The measured MTF of mobile chest examination for a large patient is not affected by changes in the kVp, added filtration or use of an anti-scatter grid.

These hypotheses are based on the following principles.

The storage phosphor used as the image detector in CR is composed of $BaFX:Eu^{++}$. The barium in the CR plate has a lower K-edge energy than the gadolinium in standard intensifying screens (37.4 keV, compared to 50.2 keV). Because of the lower

K-edge energy, CR plates have a higher detection efficiency for low-energy x rays than gadolinium intensifying screens. The use of lower energy x rays also provides better tissue contrast in radiographic images. Lowering the kVp in mobile chest radiography with CR might improve image quality with CR at the cost of increased patient dose.

In a radiographic exam, scattered radiation that reaches the imaging plate has a lower average energy than the primary radiation that did not interact in the patient. Because CR phosphors are more efficient at absorbing low-energy x rays, they are likely to be more susceptible to scattered radiation. The use of anti-scatter grids should be evaluated for improving examinations that are typically performed without grids, such as mobile chest radiography, particularly with large patients.

Aluminum filtration is added to the x-ray beam to remove some of the low energy x rays that will likely be absorbed by the patient and therefore contribute to patient dose but not to the image. Most general-use x-ray units utilize 2-3 mm of added aluminum filtration in the x-ray beam. Reducing the amount of added filtration in the x-ray beam with CR imaging may provide an output energy spectrum from the patient which would better match the absorption curve for the CR imaging plate, taking advantage of the 37.4 keV K-edge of barium.

CHAPTER 3
LITERATURE REVIEW

3.1 <u>Phantom Design</u>

3.1.1 <u>Chest Phantom Development Goals</u>

Chest radiography includes three anatomic regions of concern: the lungs, the heart and the upper abdomen (subdiaphragm). Evaluation of the image quality of a CR system for mobile chest radiography requires an appropriate phantom in order to obtain results that are meaningful for assessing possible improvements. The phantom therefore needs to contain these three regions. Anthropomorphic chest phantoms developed for diagnostic radiology use are designed to simulate an average patient in the diagnostic x-ray energy range. An anthropomorphic chest phantom usually contains a human skeleton embedded in tissue-equivalent plastic.

The non-uniformity of anthropomorphic phantoms can make it difficult to position them reproducibly with respect to AEC detectors or to make quantitative measurements. Conway *et al.* developed a more uniform phantom, the CDRH (Center for Devices and Radiological Health, Rockville, Maryland) LucAl attenuation phantom, based on an anthropomorphic chest phantom produced by Humanoid Systems (Carson, California). The LucAl chest phantom was developed for estimating patient exposures for typical chest radiographic examinations (33).

3.1.2 Chest Phantom Evaluation

Conway *et al.* defined a detector area in the lung field of the Humanoid phantom and a point near the center of the area with a screen-film OD equal to the mean OD of the area (33). This position was used as the lung field standard. The spectra exiting the phantom at this position were measured with narrow-beam transmission measurements with input beams from 80 to 120 kVp. A uniform phantom of 0.41 cm of aluminum and 7.3 cm of acrylic was created which provided the same exit spectra as the Humanoid phantom. The relative positions of the acrylic, aluminum and air were manipulated to match scatter properties under a variety of scatter conditions. The resultant LucAl chest phantom was tested on several clinical chest x-ray systems and produced entrance skin exposure values that were approximately equal to the mean patient entrance skin exposures on those systems. This phantom represents the lung-field areas of the chest only. The phantom consists of 25 cm x 25 cm attenuation blocks of acrylic and aluminum, as well as an air gap. A cross-sectional diagram is shown in Figure 3-1.
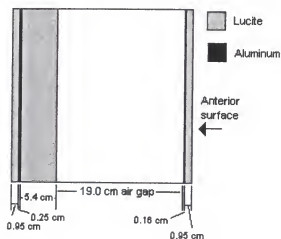
Figure 3-1 Arrangement of aluminum, Lucite and air in CDRH chest phantom [adapted from Conway *et al.*, 1984 (33)]

3.1.3 <u>Abdomen Phantom Development and Evaluation</u>

The CDRH abdomen phantom was developed similarly to the chest phantom by

matching exit spectra to a Humanoid anthropomorphic phantom (34). The resultant

LucAl Abdomen phantom consists of a 25 cm x 25 cm acrylic phantom, with additional

acrylic and aluminum in the center to represent the spine of the patient. A cross-sectional

diagram of the CDRH abdomen phantom is shown in Figure 3-2.
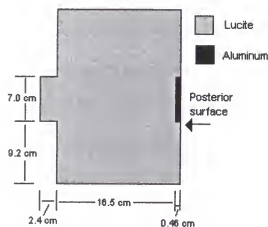
Figure 3-2 Arrangement of aluminum and Lucite in CDRH abdomen phantom [adapted
from Conway *et al.*, 1990 (34)]

3.2 <u>Scatter Measurements</u>

3.2.1 <u>Measurement of Scatter with a Lead Beam Stop</u>

Conway *et al.* measured the exit scatter plus primary intensities exiting the LuCal

phantom under various scatter conditions with an ionization chamber to match the scatter

produced to the Humanoid anthropomorphic phantom. A more quantitative way to

compare scatter conditions alone between two phantoms or two imaging systems is to use

the lead beam stop method.

The lead beam stop method involves a small diameter lead disk placed on top of a scattering phantom to block the primary radiation as shown in Figure 3-3 (35). The radiation that reaches the image receptor beneath the beam stop is scattered radiation only, while the radiation that reaches the image receptor next to the beam stop includes scattered and primary radiation. The system response, film density or pixel value, is measured at each of these two locations, and the response curve is used to calculate the scatter-to-primary ratio (S/P). The equation used to calculate S/P for a digital system is shown below, where ΔP is the difference in average pixel values measured behind the beam stop and in the adjacent areas of the image, and $\overline{G}$ is the slope of the system response between the pixel values of interest (35).

$$\frac{S}{P} = \frac{1}{\left(10^{\Delta P/\overline{G}} - 1\right)}$$
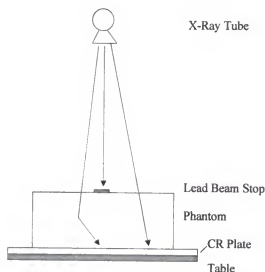
Figure 3-3 Experimental setup for the lead beam stop method used to measure S/P

3.2.2 <u>Lead Beam Stop Scatter Measurements and Results</u>

Tucker *et al.* used the primary beam stop method to measure S/P values for three

thicknesses of Lucite phantoms and three beam energies (70, 100 and 120 kVp) (35).

They compared S/P values for CR and screen-film systems and found that CR S/P values

were greater. The S/P values for both systems increased with kVp and patient thickness,

as expected.

The lead beam stop method was also used by Yip *et al.,* who modeled and

measured the scatter degradation factor (SDF) for three types of radiographic screens

($CaWO_4$, Gd_2O_2S and BaFBr) (36). For many years, $CaWO_4$ screens were the standard

intensifying screens used in screen-film cassettes. Currently Gd_2O_2S screens are typically

used as rare-earth intensifying screens in screen-film cassettes. BaFBr screens are used in

CR plates. Yip used primary and scattered spectra from Monte Carlo simulations to

model the scatter degradation factors for these three imaging systems from a homogenous

water phantom. The scatter degradation factor indicates the fraction of subject contrast

that is transferred to the image in the presence of scatter. The following equation defining

the scatter degradation factor is derived from the loss of contrast in the presence of

scatter, as discussed in Section 1.5.

$$ SDF \quad = \frac{P}{P + S} = \left(1 + \frac{S}{P} \right)^{-1} $$

A value of 1 indicates no scatter, and a value close to 0 indicates substantial

scatter. Figure 3-4 shows the results of Yip's measurements as the x-ray beam potential

was varied. The curves for GdO_2S and BaFBr crossed at approximately 70 kVp. Below
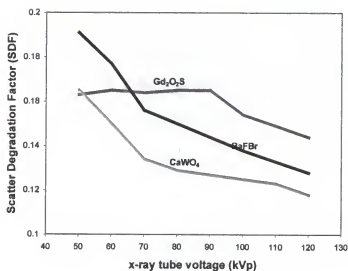
Figure 3-4 Graph of SDF as a function of kVp for three types of phosphor screens (single screen in back-screen configuration with a 20 cm water phantom) [adapted from Yip *et al.*, 1996 (37)]

70 kVp, the BaFBr phosphor used in CR systems had a higher SDF than the Gd_2O_2S used in

screen-film systems. The SDF for the CR phosphor decreased much more rapidly than the

Gd_2O_2S. These results indicate that CR systems are more sensitive than screen-film

systems to scattered radiation, and this sensitivity increases as the tube potential is

increased. The results of both of these studies suggest consideration of the use of a grid

for CR chest imaging, especially for high tube potentials and large patients.

3.3 CR Image Quality Evaluation

3.3.1 Contrast-Detail Studies and Results

The size and contrast of detected objects is another important consideration in

designing image quality studies. Observer studies using contrast-detail phantoms

containing disks of varying contrast (thickness) and detail (diameter) are often used to study the relationship between image size and resultant contrast necessary for detection.

Dobbins *et al.* used a contrast-detail phantom containing object diameters ranging from 0.05 to 2.0 cm, with 6.8 cm added acrylic thickness (38). They studied the effects of many parameters on threshold detection, including input exposure, imaging plate type and size, kVp and image processing. An improvement in detection was found at 80 kVp, compared to 110 and 140 kVp for small and intermediate-sized objects (0.05-0.2 cm).

Cowen *et al.* used another contrast-detail phantom, Leeds test object TO.16 (FAXIL, University of Leeds, Leeds, UK), which has object diameters ranging from 11.1 mm to 0.25 mm and 12 different contrast levels designed to match the reference image quality for CR imaged at 75 kVp and 1.5 mm Cu filtration (32). Threshold contrast detail detectability was evaluated by reader performance studies as a function of imaging plate type and dose.

Giger and Doi studied the effect of pixel size on SNR and threshold contrast (39). A phantom was used which contained squares of various sizes and contrast levels. No substantial difference in threshold contrast was found between pixel sizes of 0.1 and 0.2 mm in the detection of square objects ranging in size from 0.1 to 20 mm. Current CR systems use pixel sizes ranging from 0.1 to 0.2 mm, depending on plate size (see Table 1-5 in Section 1.8), which indicates that CR plate size does not affect the visualization of most radiographic image detail.

Giger and Doi also showed that the alignment of objects in relationship to pixels (centered in pixel or shifted and centered between pixels) affects the threshold contrast, except when the objects are substantially larger than the pixel size (39). Experiments with

a pixel size of 0.5 mm demonstrated that results for centered and shifted alignments converge at object sizes greater than ~3.0 mm, about 6 times greater than pixel size. Therefore, in order to eliminate alignment-related variations in contrast measurements, such as SNR measurements, it is important that the object size be considerably larger than the pixel. SNR measurements performed by Chotas *et al.* used acrylic disks that were 1.2 cm in diameter, which is about 70 times the pixel size of 0.17 mm (40).

3.3.2 SNR Measurements

SNR measurements for CR images have been performed by many groups using region-of-interest (ROI) analysis (31,40,41). Most imaging software programs provide this tool that allows mean and standard deviation measurements of pixel values in an ROI. SNR measurements for objects in CR images, such as low contrast disks, are done with ROI analysis of disk images. Mean and standard deviation measurements are made with ROIs positioned over the disk and in regions adjacent to the disk. The signal is defined as the difference between the mean pixel value inside and the average of the mean pixel values outside of the disk. Image noise is defined as the mean of the standard deviations of the ROIs. The SNR of the CR disk image is simply the ratio of these values.

Chotas *et al.* utilized both a Humanoid anthropomorphic chest phantom and an acrylic block phantom to make SNR measurements using the PCR ACe CR system (Philips Medical Systems North America, Shelton, CT) (40). The PCR ACe uses Fuji technology, including both hardware and software. The acrylic block phantom used in the study contained three areas representing the lung, mediastinum and subdiaphragm regions that were 10.0 cm, 19.8 cm and 21.5 cm thick, respectively. The thickness of acrylic used in each region had gross x-ray transmittance and scatter properties similar to those

regions of the anthropomorphic chest phantom. Two images of each phantom were taken at several kVp settings (60-120 kVp), one with and one without acrylic disks (1.2 cm thick and 1.2 cm diameter) in each of the three anatomical regions. The product of the tube current and exposure time (mAs) was adjusted to keep the calculated effective dose equivalent equal at different tube voltages, using the method of Huda and Bissessur (42).

Chotas *et al.* determined SNRs from subtracted images using ROI analysis for each disk in 9 ROIs. One ROI was positioned inside the disk and eight ROIs were positioned around the disk. The signal was defined as the difference between the mean pixel value inside and the mean of the means outside of the disk. Image noise was calculated as the mean of the standard deviations of the eight ROIs outside of the disk, divided by the square root of 2 to correct for the increase in image noise that resulted from image subtraction. The SNR was computed as the ratio of the signal to the corrected noise.

Results obtained from both the anthropomorphic and the acrylic block phantoms were similar. The SNR did not vary appreciably with changes in kVp when the effective dose equivalent was held constant. The greatest change was in the lung region, where the SNR decreased by 15% as the kVp was increased from 60 kVp to 120 kVp. The thickness of the acrylic disks used by Chotas *et al.* was not varied; therefore, the signal in the lung region of the phantoms was much higher (approximately 5×) than the signal in the other anatomical regions. Any differences that existed in the low signal regions (heart and subdiaphragm) were not visible when plotted together with the high signal region (lung).

Jing and Huda made SNR measurements using a 2.54 cm-thick acrylic phantom with small disks of bone, acrylic and aluminum as low contrast objects (43). The Fuji

sensitivity parameter S was held constant as the kVp was varied. CR film images were digitized. The pixel values of the disk region and the adjacent regions were measured and subtracted to obtain a measurement of signal. Noise was determined by measurement of the standard deviation of the pixel values in a selected uniform region of the image. Jing and Huda found that, for low Z materials (acrylic), the image contrast and SNR were independent of kVp, and for high Z materials (bone and aluminum), the image contrast and SNR were reduced with increasing kVp. Therefore, in order to make SNR measurements that are clinically relevant and comprehensive, the attenuation properties of low contrast objects should be matched to important radiographic anatomy (soft-tissue and bone).

3.3.3 MTF Measurements

Slit method. The slit method for MTF measurements involves imaging a narrow slit in a radiopaque material, called a "slit camera". A normal slit width is 10 μm. The profile of the line formed on the image is measured perpendicular to the line as shown in Figure1-23. This profile is the line spread function (LSF)of the system. The Fourier transform of the LSF is the MTF, as discussed in Section 1.6 (22).

Studies and results using slit method. Several groups have made MTF measurements of CR systems in comparison to both screen-film systems and earlier generation CR systems. In 1989 Sanada *et al.* used a dual-image recording technique to expose a CR phosphor plate and a screen-film combination with a single exposure using a Toshiba 3030A CR system, which used Fuji technology (44). Using the slit method, the MTFs of the two systems were compared. They found that the MTF of CR was superior to film at low spatial frequencies (<3 cycles/mm) and inferior to film at high frequencies

(>3 cycles/mm). In 1995, Dobbins *et al.* also used the slit method to measure MTFs of four generations of Fuji CR plates and readers (45). Some improvement in the MTF of the newer CR plates was noted.

Cowen *et al.* evaluated the physical image quality of CR systems (32). The MTF of the CR system was measured using the slit method and compared with the MTF of several screen-film combinations. The low frequency MTF curves were similar, although the limiting resolution for the screen-film images was much higher. The sampling matrix of each CR image restricted the limiting resolution.

Square wave response function. Another method of determining the MTF of a system was proposed by Coltman in 1954 (46) and used by Droege and Morin for evaluating the MTF of CT scanners (47). This method uses the square wave response function (SWRF) generated by periodic bar patterns. The following relationship is the Coltman series approximation that is used to determine the MTF, where *f* is the spatial frequency.

$$\text{MTF}(f) = \frac{\pi}{4}\left(\text{SWRF}(f) + \frac{1}{3}\text{SWRF}(3f) - \frac{1}{5}\text{SWRF}(5f) + \ldots\ldots\right)$$

Studies and results using square wave response function. Hillen *et al.* used the square wave response method when evaluating the imaging performance of first generation Fuji CR imaging plates (48). Bar patterns with spatial frequencies from 0.05 to 6.0 lp/mm were imaged. An image trace was performed in the direction perpendicular to the bars and averaged over 20 pixels. The amplitudes of each were normalized by the contrast at very low frequencies. The resultant MTF curve was found to be comparable to screen-film systems at lower frequencies (<3 lp/mm).

3.3.4 Effect of Exposure to the CR Plate

The noise in a CR image is directly related to the number of photons used to make that image, as shown in Figure 1-37 of Section 1.8. Therefore, changes in the number of photons used to make an image affects the SNR of the image. In studying the impact of certain parameters on CR image quality, such as x-ray tube potential, it is important to control the contribution of the number of photons.

In two of the studies previously mentioned, Chotas *et al.* (40) kept the effective dose equivalent to the patient constant as kVp was varied, and Dobbins *et al.* (38) kept the entrance air kerma constant. These two methods required very different x-ray beam intensities. Chotas measured the entrance air kerma values when H_E values were matched and found that the entrance air kerma values were higher at 60 kVp (133%) and lower at 120 kVp (93%), compared with the 100 kVp value.

The response of CR phosphors to different energy x-ray beams can be examined by maintaining the same total energy deposited in the imaging plate. Tucker and Rezentes showed that the imaging plate was an energy-integrating detector and that the energy deposited was dependent on the x-ray energy absorption characteristics of the phosphor and the spectrum of the incident x-ray beam. They demonstrated that the pixel value generated indicated the energy deposited (49). Current CR systems provide a dose indicator for each CR image.

3.3.5 Effect of Scatter

Scattered radiation contributes to the noise in a radiographic image, which reduces SNR of the image as described in Section 1.6. Scatter measurements of CR phosphors described above (Section 3.2) showed that CR phosphors exhibited more degradation due

to scatter than typical screen-film intensifying screens for x-ray beam energies greater than 70 kVp (37). The effect that scattered radiation detected by the image detector has on the SNR of a CR system was evaluated by Miettunen and Korhola (41). They used eleven exposure conditions with varying beam energy and entrance air kerma conditions to image a 20 cm water phantom with and without the use of different scatter reduction methods. The signal was provided by a 4-mm thick sheet of aluminum with a 10-mm hole drilled in it, which was immersed in the water phantom. The SNR values measured with the use of a 12:1 anti-scatter grid were approximately 17% higher than values measured without the grid (41).

3.3.6 Effect of Image Processing

Manipulation of image data with image processing techniques such as unsharp mask enhancement can affect measurements of image quality, including SNR and MTF measurements. Unsharp mask enhancement is an edge enhancement method used in CR imaging which is described in detail in Section 1.8. The kernel size that is used to create the unsharp mask, as well as the enhancement factor that is used, are both exam-specific parameters that are determined by the CR system.

Miettunen and Korhola examined the effect of unsharp mask enhancement on SNR measurements in CR (31). Exposure conditions used to image a 20 cm water phantom were varied, including beam energy and entrance air kerma. The signal was provided by a 4-mm thick sheet of aluminum with a 10-mm hole drilled in it, which was immersed in the water phantom. The resultant data were processed using unsharp mask enhancement with 7 kernel sizes ranging from 7 pixels to ~ 30,000 pixels, corresponding to image areas of 0.2 mm^2 to 900 mm^2 and an enhancement factor of 0.9. SNR

measurements were made using ROI analysis. The results showed that the SNR was affected by the kernel size. SNR decreased with kernel size, with larger differences noticed between kernel sizes of ~8000 and kernel sizes of ~80 (drop of approximately 40%). Above and below these values, the SNR measurements did not have much variation (31). The kernel size used by Kodak for chest images is 75 pixels which corresponds to an image area of ~2 mm^2 (21).

Giger and Doi modeled MTF measurements using different enhancement factors and kernel sizes (50). Their results were confirmed with experimental measurements using the slit method of MTF measurement. The modeled MTF curves for unsharp mask enhanced images were the product of the appropriate unsharp mask enhancement MTF (examples are plotted in Figure 1-36) and the unprocessed MTF of the CR plate. Figure 3-5 shows the resultant MTF when unsharp mask enhancement is performed with a boost factor of 0.5 and a kernel size of 3.1 mm. Experimental MTF measurements confirmed the modeled results (50).
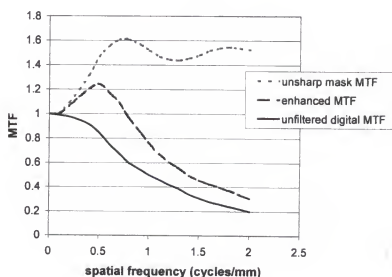
Figure 3-5 MTF for an unsharp mask enhanced digital image [adapted from Giger *et al.*, 1984 (50)]

CHAPTER 4
MATERIALS AND METHODS

4.1 Materials: CR Systems

Three commercially-available CR systems were used in this study: the Kodak Ektascan CR 400, the Agfa ADC Compact CR and the Fuji FCR5000. All make use of photostimulable phosphor technology described in Section 1.8. Differences are identified for each system in separate sections below.

4.1.1 Kodak Ektascan CR 400 System.

The Kodak CR system includes: CR imaging plate cassettes, a Model 400 storage phosphor reader, a touch-screen identification station with a bar code scanner for entering patient and exam information, and a workstation for reviewing images (21).

There are two types of Kodak CR plates: general purpose (GP-25) and high resolution (HR). The photostimulable phosphor coating composition is identical in the two types of CR plates; however, the coating used for the HR plates is thinner. Therefore, image sharpness for HR plates is superior to the general purpose plates. However, HR plates require roughly twice the intensity of x rays as GP-25 plates to generate the same amount of light, which results in a lower relative speed. The CR plates are available in three sizes: 35 x 43 cm, 24 x30 cm and 18 x 24 cm, as listed in Table 1-5 of Section 1.8. In this study, only 35 x 43 cm GP-25 CR plates were used.

The phosphor screens in the Kodak CR plates are mounted on a lead sheet for backscatter control, and both are attached to an aluminum panel. The panel is used for all

85

plate handling in the storage phosphor reader in order to minimize physical damage to the phosphor screen. A label on the back of each aluminum panel indicates the size and type of phosphor. The label also includes a barcode that identifies the cassette to the storage phosphor reader and allows the reader to match entered patient and exam information with the scanned image.

When a cassette is placed in the storage phosphor reader, the CR plate is extracted and placed on a motorized translation stage. The plate is moved in the slow scan direction as the laser scans across the short axis of the plate in the fast scan direction for 35 cm x 43 cm and 18 cm x 24 cm plates. The 24 cm x 30 cm CR plates are read in the opposite direction, so that the long axis is the fast scan direction.

Photostimulated luminescence is emitted from the phosphor screen during scanning and is focused by a collector onto a PMT. The Model 400 reader has five PMTs sitting above the plate. A collector profile is established when the system is calibrated using a flat field exposure with air kerma of 174 µGy (20 mR) with 1.5 mm aluminum and 0.5 mm copper added filtration. The collector profile is used to set the relative gains of all the PMTs in order to balance the signal across the image.

The signal from each PMT passes through a preamplifier and a summing circuit before being filtered by a Bessel (antialiasing) filter. Then the analog signal is converted to 16-bit linear data by an analog-to-digital converter. The 16-bit linear data are mapped to 12-bit logarithmic data, which make up the raw data for the image. Pixel values (P) range from 0 to 4095 and relate to the screen exposure by the following equation for GP-25 screens (21).

$$P = 1000 \left[\log\left(\frac{\text{air kerma in } \mu Gy}{8.7} \right) \right] + 2000$$

For HR screens, which generate less light, there is an offset of 300, as shown by the following equation.

$$P = 1000 \left[\log\left(\frac{\text{air kerma in } \mu Gy}{8.7} \right) \right] + 1700$$

The raw data image is then automatically processed before display on the workstation. The user can perform additional image processing functions at the workstation, including: window and level adjustments, further edge enhancement or reprocessing as a different body part. The Kodak CR 400 system offers selection of a "pattern" algorithm that provides an unprocessed (raw data) image.

4.1.2 Agfa ADC Compact CR system

The Agfa (Agfa-Gevaert, N.V.) CR system includes: CR imaging plates and cassettes, an ADC Compact storage phosphor reader, a PC identification station with a bar code scanner for entering patient information, and a workstation for reviewing images.

Agfa has only one type of CR plate available, and image sharpness for the large cassette size (35 cm x 43 cm) can be set at high or standard resolution. The same plate and scanning laser beam are used, but the high-resolution image has a much larger matrix size. The high-resolution mode is always used for the smaller cassette sizes. The Agfa CR plates come in six sizes: 35 cm x 43 cm, 35 cm x 35 cm, 24 cm x 30 cm, 18 cm x 24 cm, 10 in x 12 in and 8 in x 10 in. In this study, 35 x 43 cm CR plates with standard resolution were used.

Unlike the Kodak plates, the phosphor screens in the Agfa CR are not mounted on an aluminum backing. Therefore, they remain flexible during scanning, and they contain no lead backing for backscatter control. There is a microchip in each cassette which stores patient and exam information at the identification station. The cassette can be taken to any Agfa storage phosphor reader, where patient and exam information are matched with the scanned image.

CR plates are scanned and luminescence detected in a similar method to that described for the Kodak system. In the Agfa system all small cassettes are read so that the long axis is the fast scan direction. There is no prescan performed in the Agfa storage phosphor reader. The gain of the photomultiplier tubes is determined by the speed setting that is matched to the exam performed. It is therefore possible to "overexpose" an image by saturating the PM tubes.

Agfa CR images are processed using MUltiScale Image Contrast Amplification (MUSICA). MUSICA decomposes the image into frequency components and improves the contrast by processing the frequency components rather than the original image.

4.1.3 Fuji 5000 CR system

The Fuji CR system includes: CR imaging plates and cassettes, a model 5000 storage phosphor reader, an identification station with a bar code scanner for entering patient information, and a workstation for reviewing images.

Fuji has both standard and high resolution CR plates available. Additionally, image sharpness can be set at high or standard pixel-density. The same plate and scanning laser beam are used, but the high pixel-density image has a much larger matrix size. The Fuji CR plates come in six sizes: 35 cm x 43 cm, 35 cm x 35 cm, 24 cm x 30 cm, 18 cm x

24 cm, 10 in x 12 in and 8 in x 10 in. The matrix size associated with the large 35 cm x 43 cm CR plate used in this study, when scanned with the standard pixel density, is 1760 x 2140. The resultant pixel size is 0.20 mm, which is slightly larger than both Agfa and Kodak under similar conditions (0.17 mm) (51).

Like the Agfa plates, the phosphor screens in the Fuji CR are not mounted on an aluminum backing. Therefore, they remain flexible during scanning, and they contain no lead backing for backscatter control. Imaging plates are not returned to the same cassette after scanning. A different, previously-scanned plate is placed in the cassette so that it is ready for immediate use. A microchip in each cassette stores patient and exam information entered at the identification station. The cassette can be taken to any Fuji storage phosphor reader, where patient and exam information are matched with the scanned image.

Three readout modes are available on the Fuji CR system: Automatic, Semi-Automatic and Fixed (32). The majority of clinical images are scanned using the Automatic mode, which makes use of a pre-scan with a low-intensity laser beam. The pre-scan data are used to determine collimation borders and to optimize the sensitivity and latitude of the system for the actual image data collection. The Semi-Automatic mode allows automatic sensitivity adjustment with a fixed latitude setting, and the Fixed mode operates with fixed sensitivity and fixed latitude parameters. The mode which is used clinically (Automatic) was used for this study.

The gray scale bit depth of the Fuji system readout is 10 bits/pixel, less than both Agfa and Kodak, which use 12 bits/pixel. The resultant pixel values for Fuji CR images range from 0 to 1023, compared with 0 to 4096 for the others (51).

4.1.4 Image Processing

For all three types of CR systems used in this study, the image that is captured and digitized is also processed in order to enhance the information given to the viewer. Image processing that is common to all 3 CR systems include application of both an LUT for optimal display and an edge-enhancement algorithm. Some image processing operations, such as collimation detection, definition of the anatomic region and tone scaling, are controlled by internal parameters that are derived from the actual image data. Other image processing operations, including LUT application and unsharp-mask enhancement (described in Section 1.8), are controlled by parameters that vary according to the examination type entered at the ID station (7).

Most CR systems, including the Agfa ADC and Kodak Ektascan 400, use a reduced version of the original images as input to derive internal parameters. Some earlier generation CR systems, including the Fuji CR used in this study, use a preliminary scan of the CR plate with a low intensity laser beam as input to derive internal parameters.

4.1.5 CR Exposure Indicators

Each of the CR systems offers an imaging plate dose indicator. It has been shown that the pixel value in a CR image is related to the energy deposited in the CR phosphor(49). The Kodak CR system provides an Exposure Index that is directly related to the average pixel value of the image. Table 4-1 summarizes the dose indicators of the CR systems and the kVp and filtration settings used to calibrate this indicator. The dose indicator can easily be monitored to maintain a desired level of energy input to the phosphor.

Table 4-1 Dose indicators generated by CR systems

Manufacturer	Dose Indicator	Relationship to entrance air kerma to the plate, K (μGy)	Calibration kVp and Filtration
Kodak	Exposure Index	EI = 2000 + 1000log(K/8.7)	80 kVp, 1.5 mm Al + 0.5mm Cu filtration
Agfa	Exposure Level	LgM = 2.22 + log(K/8.7) + log(S/200)*	75 kVp, 1.5 mm Cu filtration
Fuji	Sensitivity	S= 1740/K	80 kVp, no added filtration

*S is the speed setting of the system.

4.2 Materials: Workstations

4.2.1 CEDARA Workstations

CEDARA workstations (Cedara Software, Inc., Toronto, Canada) were used during phantom development to evaluate the initial CR images made in this study. CEDARA workstations are also used by radiologists for image interpretation and were used in the clinical evaluation of mobile chest CR images of SICU patients. These workstations consist of a desktop PC with the Windows NT operating system and two high-resolution monitors (1K x 1K pixels, with 2K x 2K zooming capabilities).

The software that was used to read images was VR Report 3.1 This software contains a rectangular measurement tool, which calculates the mean, minimum and maximum pixel values for a rectangular ROI, as well as the standard deviation and area of that region. The rectangular ROI was easily positioned in different regions of an image; however, the ROI had to be redrawn in each location. Additionally the area of the ROI was measured after it was drawn, rather than simultaneously, which often necessitated repeated attempts to produce the desired ROI size.

4.2.2 Analyze Workstations

A personal computer with Analyze 3.0 imaging software (AnalyzeDirect, Inc., Lenexa, Kansas) was used for image quality evaluations, including SNR and MTF measurements. Analyze 3.0 allows image analysis of 10 Mbyte CR images without compression; this feature was not available in many other imaging programs. It also allows viewing of the image information, which ensures accuracy in identifying images that are similar in appearance. Analyze 3.0 provides many tools, such as image subtraction and flexible ROI analysis. An ROI of any size or shape can be created with size and location feedback. The same region can then be fixed and moved around the image for additional measurements of mean and standard deviation.

4.3 Materials: X-Ray Units

Several x-ray units were used for measurements in this study. Systems were selected based on their availability, their proximity to the CR system tested and their beam quality. Table 4-2 summarizes the x-ray units used for this study and their beam quality characteristics.

4.3.1 Shands at the University of Florida X-Ray Units

Rooms 1 and 9 in the Department of Radiology of Shands at UF were used for most measurements in this study. Room 1 was a Picker Clinix VPE radiographic room (Picker International, Cleveland, Ohio) with an 80 kW, three-phase multipulse generator. Room 1 was used for SNR measurements on the Agfa ADC Compact and Kodak 400 CR systems with 0 mm and 1 mm added aluminum filtration and for MTF measurements. Because it was not possible to remove 1 mm of aluminum filtration from the collimator

of Room 1, it was necessary to find another x-ray system that had the desired beam

quality and output for these measurements.

Table 4-2 Summary of location and x-ray beam characteristics for radiographic x-ray
units used for this study

X-Ray Unit	Location	Experiments performed with this unit	kVp	HVL (mm of Al)	Output at 70 cm (μGy/ mAs)
Room 1	Shands at UF	SNR (Kodak & Agfa CR, 0 & +1mm added Al filtration) MTF measurements (other than –1 mm filtration)	60	2.67	46
			80	3.61	92
			100	4.45	150
			120	5.29	213
Room 9	Shands at UF	SNR (Kodak & Agfa CR, -1mm Al filtration) Phantom evaluation MTF measurements (-1 mm Al filtration)	60	2.40	60
			81	3.18	114
			99	3.88	169
			121	4.73	246
Mayo	Mayo Clinic Jax	SNR (Fuji CR, -1mm added Al filtration)	60	2.42	57
			81	3.22	106
			99	3.90	157
			121	4.81	227
Mobile	Shands at UF	SNR (Kodak CR, mobile) Clinical Evaluation	60		
			80	2.71	124
			100	3.20	188
			120		

Room 9 was a Siemens Polydoros 80S radiographic and fluoroscopic x-ray system

(Siemens Medical Systems, Iselin, NJ). Like Room 1, Room 9 also had an 80 kW, three-

phase multipulse generator; however, Room 9 had a lower beam quality than Room 1

(3.18 mm aluminum HVL as compared with 3.61 mm at 80 kVp). Additionally, the HVL

for Room 9 was measured with 1 mm aluminum filtration added to the x-ray beam. The

resultant HVL was 3.67 mm Al at 81 kVp, which is comparable to the HVL of Room 1

with no added filtration (3.61 mm Al at 80 kVp). These measurements confirmed that

Room 9 could be utilized for SNR measurements with the low beam quality condition

("-1"). Room 9 was therefore used for the reduced filtration SNR measurements on the Kodak and Agfa CR systems. In addition Room 9 was used for S/P measurements and pixel value comparisons in the phantom evaluation.

4.3.2 Mayo Clinic Jacksonville X-Ray Unit

The x-ray unit that was used for all measurements using the Fuji 5000 CR system at the Mayo Clinic Jacksonville was a Siemens Polydoros unit. This unit was similar to Room 9 at Shands at UF. Output and HVL characteristics were measured and used to match the entrance air kerma at surface of the phantom to the entrance air kerma values used to test the Agfa and Kodak CR systems.

4.3.3 Mobile X-Ray Unit

GE AMX-4 mobile x-ray units (General Electric Medical Systems, Waukesha, WI) are used for all mobile projection radiography at Shands at UF. The GE AMX-4 is a battery discharge x-ray unit that produces a high-frequency (2 kHz) voltage waveform with substantial ripple (20%). The significant amount of waveform ripple produces an x-ray beam with an average energy that is lower than the average energy of a three-phase fixed unit x-ray beam at the same x-ray tube potential. The lower average energy of the mobile x-ray beam results in a lower beam quality. Therefore the HVL of the mobile x-ray unit at a particular kVp was similar to the HVL for the fixed units at a kVp that was 20 kVp lower (See Table 4-2). The mobile x-ray unit had a fixed tube current of 100 mA.

A GE AMX-4 mobile x-ray unit was used for SNR measurements made with the Kodak CR for mobile chest radiography conditions. This unit was also used on SICU patients in the evaluation of clinical CR images.

4.4 Materials: The Phantom for CR Chest

4.4.1 Development Goals

There are several considerations in designing a phantom that can be used for CR image quality testing. First, the phantom must include different regions in order to provide enough variation in the histogram so that it is recognized and processed correctly as a clinical chest image by the CR system. Second, the energy spectra exiting each region of the phantom should be similar to the energy spectra exiting an average patient during a chest exam. A phantom that generates a patient-similar spectrum provides an accurate indication of the CR phosphor's energy response. Lastly, the regions representing the lung, heart and subdiaphragm should be uniform to allow the addition of low contrast disks for evaluation and ROI measurements.

Because of the unique processing algorithms of CR systems, a uniform phantom cannot be used. To provide enough variation in the histogram so that the CR processes the image as clinical chest image, it is necessary to simulate the lung, heart and subdiaphragm regions of the chest. For example, when an image is recognized by the Kodak CR to be too uniform (i.e., the histogram has very little dynamic range), it is assumed to be a non-clinical test pattern and is processed as a pattern.

4.4.2 ABC Phantom

The CDRH chest and abdomen phantoms were shown by Conway *et al.* to meet the exit spectra criteria (33,34). Combining a CDRH chest phantom, a CDRH abdomen phantom and a small acrylic phantom to simulate the heart created a phantom that largely met all of the criteria. The average block chest (ABC) phantom, simulating an average patient for chest radiography, was assembled by positioning the CDRH chest phantom so

that it covered approximately two-thirds of a 35 cm x 43 cm CR plate. The CDRH abdomen phantom was positioned adjacent to the chest phantom and covered the lower third of the CR plate. The side panels were removed from the CDRH chest phantom in order to allow contiguous placement of the abdomen phantom. Therefore the chest air gap was recreated with 19-cm spacers and a laboratory jack was used for stabilization of top portion of the chest phantom. A 10 cm x 12 cm acrylic phantom (8 cm thick) was positioned in the air gap region of the CDRH LucAl Chest phantom to represent the heart. A diagram of the ABC phantom setup is shown in Figure 4-1, and a photograph of the setup is shown in Figure 4-2.
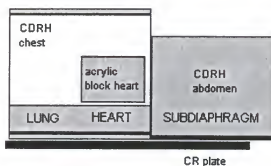
Figure 4-1 ABC phantom set-up

4.4.3 LBC Phantom

Unlike average-sized patients undergoing mobile chest radiography, large patients require crosswise orientation of the screen-film cassette or CR plate in order to image their entire lung fields. Large patients completely cover the 35 cm x 43 cm area of the cassette so that the x-ray beam is collimated to the cassette. The larger field size and the greater tissue thickness of large patients cause an increase in the amount of scatter produced, when compared with mobile chest imaging of average-sized patients.

Figure 4-2 Photograph of ABC phantom setup

Radiologists at Shands at UF have noted that chest exams performed with CR on large patients frequently produce sub-optimal, noisy images due, in part, to the increase in scattered radiation produced in these patients. A large block chest (LBC) phantom was developed in order to evaluate the response of the various parameters (kVp, filtration and grid-use) in this higher-scatter condition.

The LBC phantom was created by assembling different combinations of the ABC phantom with 2.5 cm-thick blocks of acrylic, with the goal of producing regional mean pixel values similar to clinical large patient chest images. Each combination was imaged using a Kodak CR system and the same radiographic techniques as large patient clinical images, 85 kVp and 5 mAs. The images were evaluated with ROI analysis. The final LBC phantom was created with 7.6 cm additional acrylic underneath the ABC phantom and 7.6 cm additional acrylic on each side of the ABC phantom. A diagram and photograph of the resultant LBC phantom are shown in Figures 4-3 and 4-4, respectively.

LBC phantom assembly

The ABC phantom is placed on top of 7.6 cm of acrylic. Then additional 7.6-cm thick blocks are placed on either side of the ABC phantom.
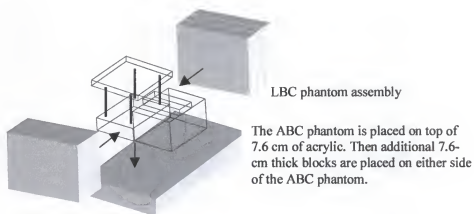
Figure 4-3 Diagram of LBC phantom

Figure 4-4 Photograph of LBC phantom setup

4.4.4 Phantom Evaluation

Pixel value comparison of the ABC phantom. The ABC phantom was first evaluated by pixel value comparison with an anthropomorphic chest phantom (Radiological Support Devices, Inc., Long Beach, CA), imaged under identical exposure

conditions. Both phantoms were exposed on top of the x-ray examination table in a simulated mobile chest exam (AP projection, 100-cm SID, 81 kVp, 1.6 mAs, without anti-scatter grid). The CR plates were processed, and the resultant images were sent to a CEDARA workstation. A rectangular ROI measurement tool was used to find the mean pixel value in an ROI with an area of 3000 pixels. Similar regions of the anthropomorphic chest and ABC phantoms were compared, as shown in Figure 4-5. The thicknesses of acrylic in the heart and subdiaphragm regions of the ABC phantom were then adjusted to match those regions in the anthropomorphic chest phantom.
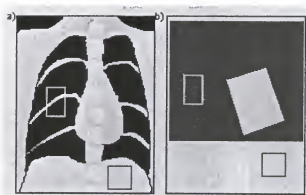
Figure 4-5 Approximate positioning of regions of interest for ROI comparison of CR images
a) anthropomorphic chest phantom; b) ABC phantom.

S/P comparison of the ABC phantom. The beam-stop method was used to compare the scatter characteristics of the ABC phantom with the anthropomorphic chest phantom. The lead beam stop method involves placement of a small diameter lead disk on top of a scattering phantom to block the primary radiation, as described in Section 3.2. The mean pixel value response of the CR was measured beneath the beam stop and next

to the beam stop with ROI analysis, and the response curve was used to calculate the S/P ratio.

This method was used to compare the scatter characteristics of the ABC phantom with the anthropomorphic chest phantom. All three regions (the lung region, the heart region and the subdiaphragm region) of each phantom were compared, respectively. A Kodak CR cassette was positioned on a radiographic table with a 100-cm SID. The x-ray field size was 35 x 43 cm at the cassette. Lead beam stops that were 2 mm thick with diameters of 0.48, 0.79, 0.95 and 1.9 cm were positioned one at a time on top of the phantom area tested, as shown in Figure 4-6.
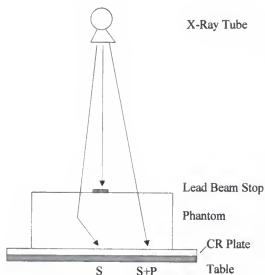
Figure 4-6 Experimental setup for phantom scatter measurements

Sixteen CR images were generated for each phantom region using the four lead beam stop diameters with x-ray tube voltages of 60, 80, 100 and 120 kVp. Images were processed with the Kodak 400 CR system and the Kodak "pattern" body part algorithm. Resultant images were sent via Ethernet through the Shands at UF Department of Radiology PACS network to a CEDARA workstation, where they were evaluated. Five

elliptical ROIs were used to measure the pixel values in the image. One ROI was positioned in the shadow of the lead beam stop, and four were positioned in the surrounding areas. The mean pixel values of the ROIs were recorded and used to calculate the pixel value difference $\Delta P = P_2 - P_1$, where P_1 was the mean of the ROI behind the beam stop, and P_2 was the average of the means of the four surrounding ROIs.

The system response curve was determined by imaging an aluminum step wedge using the Kodak 400 CR system. Again the "pattern" body part algorithm was used, which provided linear, unprocessed image data. Three exposures of the step wedge were made on a single CR plate using 70 kVp and 100 ms exposure time. The x-ray tube current was adjusted to 5, 10 and 20 mA for the three exposures. The mean pixel values of steps from the three step-wedge images were evaluated at a CEDARA workstation and used to generate a pixel value response curve as a function of relative exposure. The slope of the response curve $\overline{G}$ between the pixel values of P_1 and P_2 was used to calculate S/P ratios.

S/P ratios were calculated for each kVp and beam-stop diameter using the following equation:

$$\frac{S}{P} = \frac{1}{\left(10^{\Delta P/\overline{G}} - 1\right)}$$

The entire experiment was repeated three times with each phantom. Average S/P values were plotted with beam stop diameter and fit with a linear regression to extrapolate to a zero-area beam stop S/P value. The values obtained for each of the three regions of the two phantoms were then compared for similarity.

Pixel value comparison of the LBC phantom. A sample of 20 mobile Kodak CR chest images from large patients was selected on the basis of imaging plate positioning (crosswise), plate coverage (complete), and radiographic techniques chosen by the technologist (greater than 80 kVp). These images were evaluated using ROI measurements in the same 3 chest regions (lung, heart and subdiaphragm) used previously. The LBC phantom was modified by changing the amount of added acrylic, and the phantom was imaged with the Kodak CR employing the same x-ray techniques used for the clinical patient images. This procedure was repeated until the pixel value generated in each region of the phantom was approximately equal to the average mean ROI pixel values of the same 3 chest regions for the 20 patient images.

4.4.5 Low Contrast Disks

Disk diameter. Low contrast disks were imaged for SNR measurements in the disk locations shown in Figure 4-7. The disk located in the subdiaphragm region was furthest from the center of the x-ray beam, 8 cm in both the direction parallel and perpendicular to the anode-cathode axis. A geometric analysis of a 2-cm thick disk placed in this position was performed in order to evaluate the uniformity of the disk image. The primary source of variability across the image of the disk was due to the disk thickness because the upper and lower surfaces of the disk are different distances from the image receptor.

Figure 4-8 demonstrates the effect of a disk thickness of 2 cm on the image of a disk in the subdiaphragm region. The position of each disk edge in the image is directly determined by the position of the edge in the object plane (7 cm and 8.9 cm) multiplied by the magnification factor for each disk surface ($\frac{100}{83}$ and $\frac{100}{81}$). The positions of the
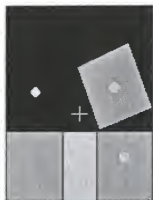
Figure 4-7 Disk location for SNR measurements

disk edges in the image are noted in the magnified portion of Figure 4-8. The resultant

image of the disk is 11.0 cm − 8.4 cm = 2.6 cm in diameter with a uniform region that is

10.7 cm − 8.6 cm = 2.1 cm in diameter.
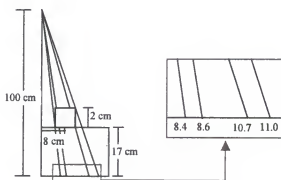
Figure 4-8 Geometric analysis of blur introduced due to disk thickness and distance from the center of the x-ray beam

Additional blur is introduced by the finite size of the focal spot as described in

Section 1.6. For the same example of a 2-cm thick disk in the subdiaphragm of the ABC

phantom, the amount of blur from a 1.2 mm focal spot is (1.2 mm)(17/83) = 0.25 mm for

the bottom surface of the disk and (1.2 mm)(19/83) = 0.29 mm for the top surface of the

disk. The image size of the disk that is 2 cm thick and 1.9 cm in diameter imaged in the

subdiaphragm region with a 1.2 mm focal spot, including both edge effects and focal spot

blur is $2.56 + (0.5)(0.025) + (0.5)(0.029) = 2.59$ cm. The uniform region of the image is

$2.08 - (0.5)(0.025) - (0.5)(0.029) = 2.05$ cm. The resultant disk image area is then

$\pi(1.29)^2 = 5.2$ cm^2, with a uniform area of $\pi(1.03)^2 = 3.3$ cm^2 or 63% of the total area. A

disk size of 1.9 cm was chosen, so that in the worst case situation, an ROI covering 63%

of the disk image would avoid penumbra from focal spot blur and edge effects due to disk

thickness and lateral displacement from the central beam.

Disk material. The thickness and material of the disk in each region was adjusted

to simulate clinically relevant pathology and maintain visibility of the disk. Acrylic and

aluminum were chosen for the disk materials because of the similarities in attenuation

properties to soft tissue and bone, respectively. Table 4-3 shows the absorption

coefficients for the materials for the energy range used in diagnostic radiology (14).

Table 4-3 Photon mass attenuation coefficients (14)

Photon energy (keV)	μ/ρ (cm^2/g)			
	Acrylic ρ=1.2 g/cm^3 Z_{eff}=6.5*	Soft tissue ρ=1.0 g/cm^3 Z_{eff}=7.4*	Aluminum ρ=2.7 g/cm^3 Z=13	Compact Bone ρ=1.9 g/cm^3 Z_{eff}=13.8*
20	0.56	0.75	3.29	2.80
30	0.30	0.36	1.12	0.97
40	0.23	0.26	0.56	0.52
50	0.21	0.22	0.37	0.35
60	0.19	0.20	0.28	0.27
80	0.18	0.18	0.20	0.21
100	0.16	0.17	0.17	0.18
150	0.15	0.15	0.14	0.15

*Z_{eff} values calculated according to the fractional contributions, a_n, of electron densities of elements in the compound according to $Z_{eff} = \sqrt[2.94]{a_1 Z_1^{2.94} + a_2 Z_2^{2.94} + a_3 Z_3^{2.94} ....}$ (8).

Disk thickness. The thickness of disk material used for each chest region and each

phantom was determined to provide a baseline SNR that was similar in all regions and in

both phantoms. To determine the disk thickness that would generate this threshold SNR level, SNR measurements were made with varying thicknesses of each disk material using the Agfa CR and typical portable chest techniques (no grid, no added aluminum filtration).

Subtracted images were also evaluated qualitatively. Disk visibility was rated on a 5-point scale, based on the criteria listed in Table 4-4. Resultant data were analyzed to determine the threshold SNR level that corresponded to a visibility rating greater than or equal to 4, with at least 75% of the edge visible. The thickness of acrylic or aluminum that generated this threshold SNR was determined, and this thickness was used for all further experimental comparisons.

Table 4-4 Disk visibility rating scale

Disk visibility rating	Criteria
0	Not visible
1	Circular pattern of noise, no edges
2	25% disk edge visible
3	50% disk edge visible
4	75% disk edge visible
5	Clearly visible

4.5 Materials: Anti-Scatter Grids

The effect of radiation scattered in the patient on the image quality of CR images was evaluated by performing measurements with and without the use of an anti-scatter grid. The grid that was used for measurements of the Agfa ADC Compact and the Kodak 400 CR systems is the type that is currently available at Shands at UF for mobile radiography. These grids are focused grids with a grid ratio of 8:1 and a line density of 33 lines/cm. Concerns about grid cut-off from misalignment, as well as the necessary increase in exposure when a grid is used, have discouraged grid use for mobile chest

imaging. The increase in exposure is not only a patient dose issue, but the time increase also raises the likelihood of blurring from patient motion.

The anti-scatter grid caps used for mobile chest radiography at the Mayo Clinic Jacksonville are parallel grids with a grid ratio of 4:1. The use of this type of grid reduces the impact of the disadvantages of grid use in mobile radiography. A parallel grid is not as sensitive to misalignment as a focused grid. A 4:1 grid requires less increase in exposure than an 8:1 grid, and therefore reduces both patient dose and patient motion artifacts. The effect of grid ratio on the transmission of scattered radiation is discussed in Section 1.5. The 4:1 grid has a line density of 40.5 lines/cm and was used for SNR measurements of the Fuji 5000 CR.

There are concerns about grid cut-off and increases in exposure when using a grid in mobile chest imaging. Therefore, a third type of grid was acquired for use in the clinical evaluation. A 3:1 parallel grid with low attenuation properties was acquired from Medical X-ray Enterprises, Inc. (Culver City, CA). The 3:1 grid had carbon fiber construction and a line density of 40.5 lines/cm. The required increase in radiographic techniques was much less with this grid (2.4× for Room 9) as compared with the 8:1 grids (3.7× for Room 9) currently in clinical use.

The contribution of scatter to the reduction in contrast of an overlying disk can be calculated using the equations described in Section 1.5, where $\dfrac{A-B}{A}$ is the contrast in the absence of scatter and $\dfrac{A-B}{A+S}$ is the contrast with scatter present (3). When T is the fractional scatter transmission through an ideal grid, the SNR values with grid use can be

estimated by the following equation: $\dfrac{A - B}{A + TS}$. Fractional scatter transmission values as a

function of grid ratio for an ideal grid (no primary attenuation) are shown in Figure 1-19

in Section 1.5. The transmission values associated with the grid ratios used in this study

are 0.20, 0.15 and 0.10 for 3:1, 4:1 and 8:1 grids, respectively (3).

4.6 Method: SNR Measurements

A low-contrast disk was placed in each of the three regions of the ABC and LBC

phantoms, described in Figures 4-1 through Figure 4-4. Figure 4-7 showed the locations

of the low-contrast disks in the phantom images.

It was necessary to remove biased sources of variability from the measurements of

SNR, even though a block chest phantom with uniform regions was used in making the

measurements. Some sources of bias include the heel effect, imaging plate non-

uniformity, scatter from other body regions and edge effects from the phantom.

SNR measurements were done using the Analyze workstation. A pair of images

was exposed for each setting, with and without the presence of the low-contrast disks.

Images were processed at a CR system and sent via Ethernet through the Department of

Radiology, Shands at UF PACS network to the clinical patient archive. The images were

retrieved from the archive as 16-bit DICOM images and imported into Analyze. The two

images were subtracted, leaving the image from the disk only with little structural

information. Image subtraction removed sources of biased noise described above that

might have affected SNR measurements.

Five ROI measurements were made for each disk, one with the ROI positioned

within the disk and 4 others with the ROI positioned in the adjacent background area. The

signal was determined by finding the difference between the mean pixel value of the ROI positioned on the disk and the average of the mean pixel values of the ROIs positioned in the background area. Noise was determined as an average of the standard deviation of the pixel values in all 5 ROI positions. Measurements of standard deviation for the background were divided by the square root of 2 to correct for the increase in image noise that resultedfrom image subtraction. This method for determination of contrast and noise characterized only the low spatial frequency performance of the CR system.

4.7 Method: MTF Measurements

The high spatial frequency performance of the CR system was evaluated by determining the MTF. A Hüttner lead and acrylic square wave bar pattern (0.5-5.0 lp/mm) was positioned in each of the three different regions of the ABC phantom. The bars of the pattern were positioned at an angle of 45° to the axes of the CR plate in order to eliminate the possibility of aliasing artifacts that might have occurred from interference with the laser scanning lines or monitor raster lines. The MTF of the CR system was then evaluated at the Analyze workstation by measuring the standard deviation of the pixel values in each cyclic group of bars and using the method developed by Droege and Morin for CT scanners described in Chapter 3 (47). The measured standard deviation of a particular cyclic group was $M'(f)$. The background noise was the standard deviation in pixel values measured in the background region of the pattern, i.e., the region without lead bars. The modulation $M(f)$ was found by correcting for the background noise (N).

$$M = \sqrt{M'^2 - N^2}$$

The MTF(f) for a square-wave input was given by the following equation.

$$\text{MTF}(f) = \frac{\pi\sqrt{2}}{4} * \frac{M(f)}{M_0}$$

For each frequency the MTF was normalized by the contrast at very low frequency (0.5 lp/mm) to reduce the contribution of image processing. The resultant MTF curves indicated the high contrast response of the CR systems, including image capture, digitization and processing for chest images.

Differences between different MTF curves were quantified by determination of the area under the curve. The area under the MTF curve was calculated as the sum of the product of each spatial frequency and the MTF measured at that frequency, as shown in the following equation:

$$\text{area under MTF curve} = \sum_{f=0.5}^{f_{max}} f \times \text{MTF}(f)$$

4.8 Method: Experimental Conditions

Image quality evaluations were made under different conditions of x-ray parameter settings. The peak tube potential was varied from 60 kVp to 120 kVp. The amount of aluminum filtration in the x-ray beam was varied by either use of an x-ray unit with a lower beam-quality (equivalent to the initial system with 1 mm aluminum filtration removed from the beam) or by adding 1mm of aluminum to the collimator of the initial system. Scatter conditions were also varied by using or not using an 8:1, 33 lines/cm, 86-112 cm focal range grid in front of the CR cassette. A 4:1, 41 lines/cm, parallel grid was used with the Fuji CR system. As the x-ray conditions were varied, the energy that was absorbed by the CR plate was kept constant by adjusting the tube current and the time of exposure (mAs). The energy that was absorbed by the plate is indicated by the exposure

value generated by the CR system. Table 4-1 in Section 4.1 lists the exposure indicators and the calibration method for each type of CR system. For the Kodak CR, an Exposure Index of 2000 indicated an air kerma of 8.7 µGy (exposure of 1 mR) at the CR plate with an 80 kVp x-ray beam that has been filtered by 1.5 mm Al and 0.5 mm Cu filtration. Similarly for the Agfa CR, an Exposure Level of 2.52 indicated an air kerma of 8.7 µGy to the CR plate with a 75 kVp x-ray beam filtered by 1.5 mm Cu.

Table 4-5 shows the exposure parameters that were chosen for the SNR experiments using the ABC phantom and the resultant exposure indicators. Although identical exposure conditions were used for both systems, the actual exposure indicator values produced by the CR systems were slightly higher for the Agfa system (2.69±0.02) and slightly lower for the Kodak system (1777±49) than expected for an air kerma delivered to CR plate of ~8.7 µGy. A decision was made to keep the mAs constant for the 2 systems in order to compare each system's response to the same exposure conditions. The exposure conditions were maintained in order to simulate the clinical environment in which a technologist may use one of several CR systems.

The Fuji CR system was tested at a different facility (Mayo Clinic Jacksonville). The HVL of the x-ray tube at the second facility was measured to be 3.2 mm of aluminum at 81 kVp, as compared with 3.2, 3.6 and 4.1 mm of aluminum for the three filtration conditions (-1, 0, +1 mm added aluminum filtration) at Shands at UF at ~80 kVp. Therefore the HVL at the second facility was equivalent to the low beam quality condition (-1 mm) at the primary facility. The output of the x-ray tube in µGy/mAs was also measured and used to match the exposure at the phantom surface to the exposure produced at the primary facility. The exposure indicator on the Fuji system, the

Sensitivity (S), is calibrated with an unfiltered 80 kVp x-ray beam. Although the

Sensitivity parameter did not remain constant with kVp variation, as shown in Table 4-5,

the exposure conditions for testing the Fuji CR system were matched to those used at the

primary facility with the other CR systems.

Table 4-5 Technique factors used to generate approximately constant exposure indicators
for the ABC phantom.

Image #	kVp	Added Al filtration (mm)	Grid used	mAs (Fuji mAs)	Kodak Exposure Index (EI)	Agfa Exposure Level (LgM)	Fuji Sensitivity (S)
1	60	-1	No	5.0 (5.0)	1810	2.68	193
2	80	-1	No	1.4 (1.6)	1770	2.65	177
3	100	-1	No	0.7 (1.0)	1760	2.65	135
4	120	-1	No	0.6 (0.6)	1890	2.72	113
5	60	-1	Yes	20 (16)	1700	2.70	232
6	80	-1	Yes	5.6 (5.0)	1690	2.70	166
7	100	-1	Yes	2.8 (2.8)	1740	2.69	158
8	120	-1	Yes	1.6 (1.6)	1760	2.69	128
9	60	0	No	6.4	1780	2.69	
10	80	0	No	2.0	1810	2.70	
11	100	0	No	1.0	1780	2.71	
12	120	0	No	0.6	1780	2.66	
13	60	0	Yes	20	1720	2.68	
14	80	0	Yes	6.0	1810	2.72	
15	100	0	Yes	3.0	1810	2.70	
16	120	0	Yes	1.8	1730	2.68	
17	60	+1	No	7.0	1810	2.68	
18	80	+1	No	2.3	1850	2.72	
19	100	+1	No	1.1	1840	2.72	
20	120	+1	No	0.6	1760	2.67	
21	60	+1	Yes	21.6	1680	2.68	
22	80	+1	Yes	6.4	1800	2.70	
23	100	+1	Yes	3.2	1780	2.70	
24	120	+1	Yes	2.0	1780	2.70	

Table 4-6 lists the technique factors used for SNR experiments with the LBC

phantom and the associated exposure indicators. For the same kVp, the mAs settings used

for the LBC phantom images were significantly higher than the settings used for the ABC

phantom. When the phantoms were imaged without an anti-scatter grid, the LBC

phantom required mAs settings that were 2 to 2.6 times higher than the ABC phantom

imaged without a grid. Compared with mAs settings for the ABC phantom with an 8:1

grid, using the grid for the LBC phantom required an increase in mAs of 3.2 to 5.6 times.

Table 4-6 Technique factors used to generate approximately constant exposure indicators
for the LBC phantom.

Image #	kVp	Added Al filtration (mm)	Grid used	mAs (Fuji mAs)	Kodak Exposure Index (EI)	Agfa Exposure Level (LgM)	Fuji Sensitivity (S)
1	60	-1	No	14 (16)	1940	2.63	161
2	80	-1	No	3.6 (4.0)	1870	2.70	146
3	100	-1	No	1.8 (2.2)	1910	2.69	134
4	120	-1	No	1.1 (1.4)	1990	2.70	122
5	60	-1	Yes	100 (110)	2090	2.70	128
6	80	-1	Yes	22 (25)	2090	2.70	111
7	100	-1	Yes	11 (12.5)	2020	2.75	81
8	120	-1	Yes	5.0 (7.1)	1950	2.69	54
9	60	0	No	16	1870	2.71	
10	80	0	No	4.0	1890	2.69	
11	100	0	No	2.0	1900	2.70	
12	120	0	No	1.2	1910	2.66	
13	60	0	Yes	120	2100	2.71	
14	80	0	Yes	25	2100	2.69	
15	100	0	Yes	11	2000	2.72	
16	120	0	Yes	6.0	2000	2.72	
17	60	+1	No	18.0	1880	2.69	
18	80	+1	No	4.5	1890	2.70	
19	100	+1	No	2.0	1880	2.68	
20	120	+1	No	1.2	1900	2.65	
21	60	+1	Yes	125	2080	2.67	
22	80	+1	Yes	28.0	2120	2.68	
23	100	+1	Yes	11.0	1990	2.69	
24	120	+1	Yes	6.0	2000	2.73	

System Monitoring. Selected SNR measurements of the acrylic disk in the lung

region and the aluminum disk in the heart region were repeated approximately 4 months

after the initial measurements were completed for the Agfa and Kodak CR systems.

Repeat measurements evaluated experimental reproducibility and monitored the performance of the system hardware over time. Results for one of the CR systems were repeated a third time, following system calibration to adjust the overall gain of the PMTs on that system.

4.9 Method: Phantom dose Measurements

Effective dose to the phantom was determined for each experimental condition. The entrance skin exposure without backscatter was measured with a Radcal MDH model 1015 Radiation Monitor with a 10X5-6 ionization chamber (Monrovia, CA) and was corrected to the patient entrance plane. The HVL of each x-ray beam was also measured. The energy imparted (ε) in joules to the phantom was calculated using the method of Gkanatsios and Huda (52). The effective dose to the phantom was then calculated using published ratios of E/ε, based on National Radiological Protection Board (NRPB) Monte Carlo calculations. For an AP chest exam of an average-sized adult (70 kg), this value is 22.4 ± 0.9 mSv/J and independent of kVp and beam filtration for the range used in this study (53).

4.10 Method:Data Analysis

The absolute SNR values produced by a CR system are affected by many system-dependent functions. System-dependent functions include hardware, such as the overall gain of PMTs which may drift without frequent calibration, and software, such as the kernel size used in unsharp mask enhancement (31). Therefore, only relative comparisons should be made between different CR systems, even between two systems from the same manufacturer.

4.10.1 Paired t Test

Paired t tests (α=0.05) were performed on selected SNR data to examine the effect of tube potential, added aluminum filtration and anti-scatter grid use on the SNR of each disk material in each chest region with both the Kodak and Agfa CR systems. Paired t tests were performed on data collected using the Fuji CR only for comparison of SNR values from images acquired with and without an anti-scatter grid. The sample size for other comparisons, e.g., 60 kVp compared with 80 kVp, was too small to provide meaningful results.

All paired t tests were performed with the data analysis tool available in Microsoft Excel (Microsoft Corporation, USA) in order to compare data acquired under various conditions. A paired t test was used to evaluate differences between samples of paired data, such as two samples of SNR values. A sample of SNR values from images acquired at 60 kVp was compared to a sample of values from images acquired at 80 kVp to evaluate the effect of kVp on SNR. A test statistic t was calculated, based on the differences between each pair of SNR values, as well as the sample size and variability of the data. The test statistic was then compared with a critical t value that depended on the sample size and the confidence interval. The resultant p values showed the probability that the mean value of sample 1 was greater than the mean value of sample 2 (54). In this case, using a 95% confidence interval, p values of less than 0.05 indicated a significant difference between the samples. A negative t value indicated a negative mean difference, or that SNR values for sample 2 were higher than sample 1.

4.10.2 <u>Relative SNR Comparisons</u>

Absolute SNR measurements can be affected by many system-dependent parameters, including image processing. To evaluate the effect of one imaging parameter on the SNRs measured, ratios of SNR values were used to make relative comparisons. Ratios were computed by dividing each experimental SNR value by the SNR value measured when mobile chest radiography techniques that are used at Shands at UF were used (i.e., 80 kVp, no grid). For example, the relative-grid SNR value was the SNR value measured with use of an anti-scatter grid divided by the SNR value measured without use of an anti-scatter grid with other conditions identical.

The relative-grid SNR values were predicted using the equations for contrast in the presence of scatter described in Section 4.5. For an ideal grid, the relative SNR values are described by the following equation:

$$\frac{\dfrac{A-B}{A+TS}}{\dfrac{A-B}{A+S}} = \frac{A+S}{A+TS}$$

where T is the fractional scatter transmission through an ideal grid. This equation may be reduced to: $\dfrac{1+\dfrac{S}{A}}{1+\left(\dfrac{S}{A}\right)T}$, where S/A = S/P. The transmission values associated with the grid ratios used in this study were 0.20, 0.15 and 0.10 for the 3:1, 4:1 and 8:1 grids, respectively (3).

4.11 <u>Method: Clinical Evaluation</u>

A major difference between the use of screen-film radiography and CR is that, in screen-film radiography, the functions of image capture, processing and display are all

performed by the same medium, the x-ray film. In CR these functions are performed by different systems, which allows more freedom in manipulation of parameters. SNR and MTF measurements of phantom images in CR provide valuable information about the image capture process in CR. In order to examine the clinical effect of parameters which improved SNR, a clinical evaluation was performed.

Imaging parameters that improved the SNR of low contrast disks in block phantom images were tested on actual patient images to ensure applicability. Mobile chest radiographs are performed daily on many patients in the SICU in Shands at UF. Sometimes clinical mobile chest CR images are suboptimal. This environment provided an opportunity for performing multiple images of the same patient on consecutive days using different imaging parameters, but without performing a clinically unnecessary exam. Two parameters, kVp and grid-use, were systematically adjusted both independently and together. The techniques chosen were within the range of techniques used commonly and therefore this evaluation did not require assessment by the institutional review board. A 3:1 parallel grid with carbon fiber construction was acquired from Medical X-ray Enterprises, Inc., for mobile chest images during the clinical evaluation at Shands at UF.

Mobile chest radiography techniques currently in use at Shands at UF utilized x-ray tube voltages in the 85 kVp to 95 kVp range, depending on individual patient size. On Day 1a of the clinical evaluation, mobile chest radiographs in the SICU at Shands at UF were performed with using current standard techniques. The mAs setting was also adjusted to produce an image with an Exposure Index of approximately 1800 (typical Exposure Index because the system was in need of calibration). The Exposure Index

generated by the CR system for each image was recorded. These images were acquired so that evaluation of image quality with adjusted parameters could be directly compared to an image acquired with standard techniques.

On Day 2 of the clinical evaluation data collection, a lower tube potential (-10 kVp) was used to acquire mobile chest radiographs of the same patients imaged on Day 1a. To reduce the effect of image noise, a relatively constant Exposure Index was maintained for each patient's image. As the kVp was reduced, the Exposure Index was maintained by increasing the corresponding mAs setting by 30-60%.

On Day 3 of the clinical evaluation data collection, an anti-scatter grid was used with the typical tube potential to acquire mobile chest radiographs of the same patients imaged on Day 1a. To reduce the effect of image noise, a relatively constant Exposure Index was maintained for each patient's image by increasing the mAs setting with grid use by 2 to 2.5 times.

The images collected on Days 1a, 2 and 3 were evaluated by radiologists, and the data were analyzed before further technique adjustments were made. A second set of standard technique images was collected for the second part of the clinical evaluation (Day 1b). The new set of images contained some patients who were different from the original set and allowed comparison of images from adjacent days, which reduced the contribution of changes in patient condition. On Day 4 of the clinical evaluation data collection, a higher tube potential (+15 kVp) was used to acquire mobile chest radiographs of the same patients imaged on Day 1b. To reduce the effect of image noise a relatively constant Exposure Index was maintained for each patient's image. The

Exposure Index was maintained by decreasing the mAs setting by 37% as the kVp was increased.

On Day 5 of the clinical evaluation data collection, an anti-scatter grid was used with a higher tube potential (+15 kVp) to acquire mobile chest radiographs of the same patients imaged on Day 1b. To reduce the effect of image noise, a relatively constant Exposure Index was maintained for each patient's image by increasing the mAs by 60% to compensate for the use of the grid. The experimental design is summarized in Table 4-7.

Table 4-7 Experimental design for clinical evaluation image acquisition

Test day	Parameter adjusted	mAs change
Day 1 (a or b)	Standard kVp	0
Day 2	Decreased kVp (-10 kVp)	+ 30-60%
Day 3	Standard kVp, grid	× 2-2.5
Day 4	Increased kVp (+15 kVp)	− 37%
Day 5	Increased kVp (+15 kVp), grid	+ 60%

Image quality evaluations were made for both the lung and heart regions of the clinical images by 5 radiolgists. Two additional radiologists evaluated images from Day 2 and Day 3 only.

Clinical image evaluation. The patient images that were collected were presented to five board-certified radiologists and two radiology residents for evaluation. Two images of the same patient, acquired with different imaging parameters, were presented simultaneously on one monitor of a CEDARA workstation. Radiologists were encouraged to adjust the window and level of each image as they would during clinical practice. They were also allowed to use other imaging tools, such as the magnifying tool. The initial image of each patient, acquired with normal techniques was used as a standard and

assigned an image quality rating of 3. Radiologists were asked to compare each of the other images, without knowledge of technique changes, to the standard and to rate the lung and heart regions of each. The 5-point scale shown in Table 4-8 was used for rating the images, based on visibility of structures, contrast, noise and overall impression. Radiologists were asked to disregard changes in patient pathology that may have occurred between consecutive images.

Table 4-8 Clinical evaluation ratings for image quality comparison

Score	Image quality in comparison with standard image
1	Much worse
2	Worse
3	Equivalent
4	Better
5	Much better

CHAPTER 5
RESULTS

5.1 Phantom Development

As described in Section 4.4, the validity of the block phantoms for use in this study was assessed in two ways. First, the ABC phantom was compared with the anthropomorphic chest phantom in the three anatomic regions, using mean pixel values as the criterion. Because the LBC phantom was designed to simulate large patients, the anthropomorphic phantom, designed to simulate average-sized patients, was not useful for comparison purposes; rather, the LBC phantom was compared with data derived from clinical chest radiographs of large patients.

5.1.1 Pixel Value Comparison for ABC Phantom

Both the anthropomorphic chest phantom and the ABC phantom were imaged using the Kodak CR system that was used for clinical mobile chest radiography. Pixel values in each chest region were measured at a CEDARA workstation and are presented in Table 5.1. The mean pixel values in the lung and heart regions were very similar for both chest phantoms. The mean pixel value in the subdiaphragm region was lower for the ABC phantom than it was for the anthropomorphic phantom. These data indicated that there was more exposure reaching the imaging plate, and therefore, less attenuation in the subdiaphragm region of the ABC phantom in comparison with the anthropomorphic phantom. However, this region is not considered critical by radiologists in the review of

chest exams. Rather, this region was included in order to simulate the scatter situation found in a patient and to provide histogram variability for correct CR processing.

Table 5-1 Mean pixel value comparison of ABC phantom with anthropomorphic chest phantom.

Chest region measured	Mean pixel value of ROI (CEDARA)	
	Anthropomorphic Phantom	ABC Phantom
Lung (CDRH chest)	1017	1016
Heart (CDRH chest + heart block)	1342	1276
Subdiaphragm (CDRH abdomen)	1524	1267

5.1.2 Pixel Value Comparison of LBC Phantom

In order to develop criteria for assessing the validity of the LBC phantom, twenty clinical images of large patients were collected from the two Kodak CR systems that were used clinically to produce mobile chest radiographs at Shands at UF. These images were evaluated with Analyze 3.0 imaging software using ROI analysis. Irregular-shaped ROIs were positioned to include the largest possible area of the region being measured; therefore, the size of the ROI varied with patient anatomy. Fourteen of the twenty images collected were imaged with the same radiographic technique factors, 85 kVp and 5 mAs. The average of the regional mean pixel values from these 14 images was chosen to be the target value used to create the LBC phantom. Table 5-2 lists the average of the mean pixel values of each region for both CR systems, as well as the average of the 14 images acquired with the same radiographic techniques.

Pixel values measured in each region of the LBC phantom, as well as the average patient values obtained with the same techniques, are presented in Table 5-3. The mean pixel values were very similar, with differences of less than 100 in all regions, and less than 50 for the lung and heart regions.

Table 5-2 Summary of regional mean pixel values from mobile chest images of large clinical patients

Subgroup averaged (number of images)	Mean pixel value		
	Lung	Heart	Subdiaphragm
Processed at CR2[1](10)	1325	2457	3279
Processed at CR5[2](10)	1476	2427	3087
Imaged at same technique settings (14)	1435	2447	3167

[1]Kodak CR 400 system located in the SICU at Shands at UF.
[2]Kodak CR 400 system located in the MICU at Shands at UF.

Table 5-3 Mean pixel value comparison of LBC phantom with clinical patient average.

Chest region measured	Mean pixel value	
	Large patient average	LBC Phantom
Lung	1435	1388
Heart	2447	2474
Subdiaphragm	3167	3073

5.1.3 S/P Measurements for ABC and Anthropomorphic Phantoms

Additional validation of the ABC phantom was made by comparison of S/P values with the anthropomorphic phantom. First, the CR pixel value response as a function of relative plate exposure was determined. Figure 5-1 shows the pixel value response of the
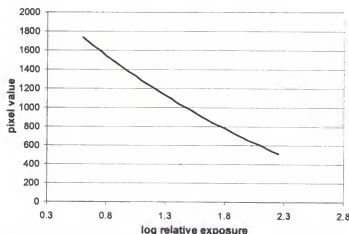
Figure 5-1 Pixel value response of the CR generated with ROI analysis of relative exposures of an aluminum step wedge.

Kodak 400 CR system to input exposure measured at the CEDARA workstation. This curve was generated by imaging an aluminum step wedge at 3 exposure levels (×1, ×2 and ×4) on the same CR plate and measuring the mean pixel value of the same step at each exposure level. The gradient or slope of this curve between two pixel values was used in calculating the S/P values.

Next, S/P values were determined for the two phantoms for three different lead disk diameters (0.48, 0.79 and 0.95 cm). The resulting data are shown in Figure 5-2. Figure 5-2(a) shows the data for the anthropomorphic chest phantom at each kVp, and Figure 5-2(b) shows the data for the ABC phantom. The lines are linear regression fits to the data.

The S/P values calculated for the two phantoms are similar. However, values of S/P for the anthropomorphic phantom had a larger negative slope as a function of lead beam-stop diameter. This trend was especially true for the heart and sudbdiaphragm regions, where there was more scattered radiation produced. In these regions, the slope of the regression line was 2.6 to 9 times as large for the anthropomorphic phantom as the ABC phantom. By contrast, the slopes of the regression lines in the lung region were more similar, ranging from –0.34 to –0.53 for the ABC phantom and –0.15 to –0.72 for the anthropomorphic chest phantom ($r^2 = 0.95$).

Figure 5-3 shows the 0.48-cm beam stop S/P values for each phantom as the kVp was varied. As expected, the S/P values increased with kVp in all cases. This figure showed the two phantoms to be relatively scatter-equivalent in all three regions, and they were particularly well-matched in the heart region. S/P values for the ABC phantom were

somewhat higher in the lung region (24%), and lower in the subdiaphragm (22%) region

than the values for the anthropomorphic phantom.
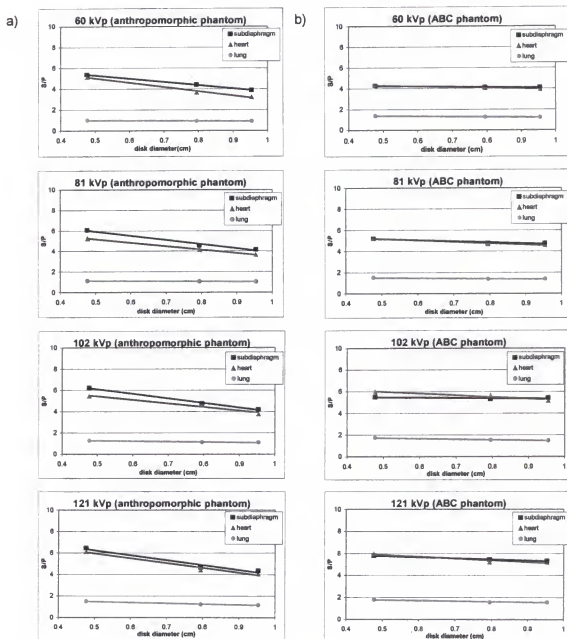
Figure 5-2 Scatter-to-primary ratios as a function of lead disk diameter (0.48, 0.79 and 0.95 cm) at each kVp measured for a) the anthropomorphic chest phantom and b) the ABC phantom
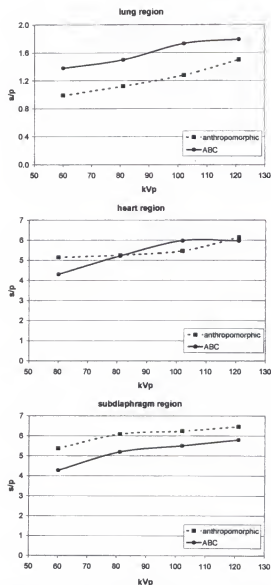
Figure 5-3 S/P ratios as a function of kVp for each chest phantom region for the 4.8 mm lead beam stop (Note that a different scale is used for the lung-region graph)

Although the S/P values in the lung region were higher for the ABC phantom than for the anthropomorphic chest phantom, the difference between the values remained approximately constant at 0.38±0.06 over the kVp range. Therefore, the differences between the phantoms were not likely to introduce variability in studying the effects of changing beam quality. S/P values in the heart region from the two phantoms were very similar, with an average difference in values of 0.14. The S/P values in the subdiaphragm

region showed the greatest variability, with an average difference of 0.85. However, as explained previously, this region is of little concern for clinical chest imaging.

5.2 Low Contrast Disk Determinations

Section 5.1 described the validation of the ABC and LBC phantoms for the purpose of providing reasonable images to use as comparison for varying chest radiographic techniques. The next experiments were designed to determine appropriate low contrast disk sizes for use in assessing CR image quality.

5.2.1 Low Contrast Disk Thickness for the ABC Phantom

Disk-thickness experiments were performed with the ABC phantom on the Agfa CR system using typical mobile chest radiography techniques as a reference standard (80 kVp and no anti-scatter grid). Disk diameters were 1.9 cm, chosen for geometric criteria described in Section 4.4. Figure 5-4 shows the relationship between SNR and disk visibility, including data from all regions of the ABC phantom and both acrylic and aluminum disk materials. Disk visibility was rated according to a scale presented in Table
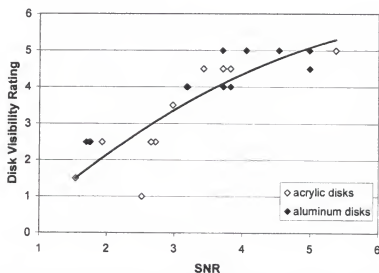
Figure 5-4 Disk visibility rating as a function of measured SNR, including data from all regions of the ABC phantom and both disk materials.

4-4. The curve represents a second order polynomial curve fit to the data. Table 5-4 lists

the results of the SNR measurements by region and material.

Table 5-4 Data comparing disk visibility rating and SNR by region and material for
different thicknesses of 1.9 cm-diameter disk with the ABC phantom

Region	Disk material	Disk thickness (mm)	SNR	Visibility rating
Lung	acrylic	2	2.52	1
		4	3.80	4.5
		6	5.37	5
		8	7.17	5
	aluminum	0.5	3.82	4
		1	4.98	5
		2	8.98	5
Heart	acrylic	8	1.74	2.5
		12	2.72	2.5
		15	2.97	3.5
		18	3.71	4.5
	aluminum	2	1.76	2.5
		3	3.17	4
		4	3.71	4
		6	4.98	4.5
		7.5	6.17	5
Subdiaphragm	acrylic	8	1.54	1.5
		12	1.93	2.5
		15	2.65	2.5
		20	3.17	4
		22	3.42	4.5
	aluminum	2	1.69	2.5
		4	3.19	4
		5	3.70	5
		6	4.05	5
		8	4.53	5

A visibility rating of 4, which corresponded to a disk with 75% or more of its edge

visible, was used as a threshold level. Inspection of the data in Figure 5-4 comparing disk

visibility rating with SNR shows that there is a cluster of data points with a disk visibility

rating between 4 and 5, which have SNR values between 3 and 4. All SNR values greater

than 4 corresponded to disks with more than 75% of their edge visible. The minimum

SNR that corresponded to a visibility rating of 4 or greater from all measurements was

3.17. The minimum SNR with a visibility rating of 4 or greater from each group

(region/disk material) averaged 3.48. This information was used to set the threshold SNR

level to 3.5. The disk thickness that produced the SNR value closest to 3.5 was selected

for use throughout the subsequent SNR experiments with the ABC phantom. These

values are summarized in Table 5-5.

Table 5-5 Summary of data comparing disk visibility rating and SNR for disk thicknesses
selected for SNR experiments with the ABC phantom

Region	Disk material	Disk thickness (mm)	SNR	Visibility rating
Lung	acrylic	4	3.80	4.5
	aluminum	0.5	3.82	4.0
Heart	acrylic	18	3.71	4.5
	aluminum	4	3.71	4.0
Subdiaphragm	acrylic	22	3.42	4.5
	aluminum	5	3.70	5.0

5.2.2 Low Contrast Disk Thickness for the LBC Phantom

Disk-thickness experiments were also performed for the LBC phantom with

typical reference mobile chest radiographic techniques (no anti-scatter grid and no added

aluminum filtration), using 80 kVp. Table 5-6 lists the results of the SNR measurements

by region and material. First, SNR measurements were made with the same disk

thicknesses and materials used for SNR measurements in the average phantom. SNR

measurements from these thickness values averaged only 1.3 with the LBC phantom, as

compared with 3.5 for the ABC phantom. Disk thicknesses were increased and SNR

remeasured. An SNR value of 3.5 was again used as a threshold level to determine what disk thickness should be used. The disk thickness that produced the SNR value closest to 3.5 was selected for use throughout the subsequent SNR experiments with the LBC phantom. These values are summarized in Table 5-7.

Table 5-6 Data comparing disk visibility rating and SNR by region and material for different thicknesses of 1.9 cm-diameter disk with the LBC phantom

Region	Disk material	Disk thickness (mm)	SNR	Visibility rating
Lung	acrylic	4	1.44	1
		8	3.16	3.5
		10	3.44	4
		12	4.53	4
	aluminum	0.5	0.98	0.5
		1	4.98	5
		2	3.35	4
		3	5.05	4.5
Heart	acrylic	18	1.69	0.5
		25	2.20	2
		54	3.01	3
	aluminum	4	1.55	0.5
		14	2.41	3
		16	2.91	3.5
		18	3.36	4
Subdiaphragm	acrylic	22	1.07	1
		25	1.53	1
		50	2.10	1
		54	1.87	1
	aluminum	5	0.95	1
		15	2.90	3
		20	3.30	4

In both the heart and subdiaphragm regions, the thickness of acrylic required to reach the threshold SNR level of 3.5 was greater than 5.4 cm. This thickness of disk dramatically increases the blur that is introduced from both geometric blur (off-axis) and

focal spot blur, and causes the image of the disk to be less than 25% uniform. Furthermore, SNR measurements of the acrylic disk in the lung region and the aluminum disk in the heart region are the most clinically applicable because they are indicative of the visibility of lung nodules and vertebral bodies in chest radiographs, respectively. For these reasons the SNR values in the heart and subdiaphragm regions of the LBC phantom were measured only with aluminum disks.

Table 5-7 Summary of data comparing disk visibility rating and SNR for disk thicknesses selected for SNR experiments with the LBC phantom

Region	Disk material	Disk thickness (mm)	SNR	Visibility rating
Lung	acrylic	10	3.44	4
	aluminum	2	3.35	4
Heart	aluminum	18	3.36	4
Subdiaphragm	aluminum	20	3.30	4

5.3 SNR Measurements

Signal-to-noise ratio (SNR) measurements were made for the acrylic and aluminum low contrast disks listed in Tables 5-5 and 5-7 for the ABC and LBC phantoms, respectively. All low contrast disks were 1.9 cm in diameter. Complete SNR results for the ABC phantom are tabulated in Appendix A. Complete SNR results for the LBC phantom are tabulated in Appendix B. Results in this section include only the SNR measurements made with acrylic disks in the lung region and aluminum disks in the heart region, because these materials and regions were the most clinically applicable.

5.3.1 Effect of kVp on SNR Measurements

Figure 5-5 shows the SNR values as a function of kVp for the 4-mm thick acrylic disk in the lung region of the ABC phantom. To verify experimental reproducibility, a

standard deviation of measurements was calculated from 3 replicate measurements done within a 2-week period with the Agfa CR at 80 kVp without use of an anti-scatter grid, producing an SNR of 3.77±0.04.
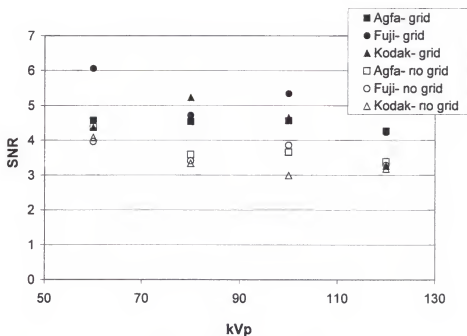
Figure 5-5 SNR measurements as a function of x-ray tube potential for a 4-mm thick acrylic disk in the lung region of the ABC phantom imaged with the low beam quality x-ray unit

The SNR values measured with the use of an anti-scatter grid were approximately 30% higher than non-grid SNR values for all CR systems. SNR values performed with a 60-kVp x-ray beam were somewhat higher than other values. However, there was not much variation among SNR values at higher kVps (80 to 120 kVp). SNR values decreased by approximately 15% as the kVp was increased from 60 kVp to 120 kVp.

There are many system-dependent parameters that can affect the SNR. Therefore, relative-kVp SNR values were calculated to evaluate the general effect of kVp on SNR values for CR in mobile chest radiography. The relative-kVp SNR values were calculated by dividing the SNR value at a particular kVp by the SNR value at 80 kVp for the same

CR system and grid conditions. Relative-kVp SNR values for the acrylic disk in the lung region of the ABC phantom are shown in Table 5-8, including repeated results acquired with the Kodak and Agfa CR systems. Relative-kVp SNR values produced with different CR systems were fairly consistent among manufacturers for the case without the use of a grid. There was more variation in the relative-kVp SNR values acquired with the anti-scatter grids, where very little kVp dependence was noticed. The grids used were not identical for the 3 systems tested, because the 4:1 grid was used with the Fuji system while the 8:1 grid was used with Agfa and Kodak. The first replicate data for the Kodak CR acquired at 60 kVp without a grid produced an obviously outlying data point with a relative-kVp SNR value of 1.62. Therefore, the average relative value for this case was calculated without this outlier.

Table 5-8 Relative-kVp SNR values for acrylic disk in the lung region of the ABC phantom

Grid Use	kVp	$SNR_{kVp}/SNR_{80\,kVp}$						
		Agfa Set 1	Agfa Set 2	Kodak Set 1	Kodak Set 2	Kodak Set 3	Fuji	Average values
Yes	60	1.01	1.28	0.84	0.98		1.28	1.08±0.17
	80	1.00	1.00	1.00	1.00		1.00	(reference)
	100	1.01	1.13	0.89	0.78		1.13	0.99±0.14
	120	0.94	1.15	0.62	0.85		0.90	0.89±0.17
No	60	1.22	1.16	1.22	1.62	1.17	1.16	1.19±0.03*
	80	1.00	1.00	1.00	1.00	1.00	1.00	(reference)
	100	1.02	1.01	0.90	0.99	0.99	1.13	1.01±0.07
	120	0.94	1.09	0.95	1.08	1.08	0.96	1.02±0.07

*60 kVp-no grid average value was computed without the highest relative-kVp SNR value.

Figure 5-6 shows SNR values as a function of kVp for the 4-mm thick aluminum disk in the heart region of the ABC phantom for the low-HVL (-1) filtration condition. As seen with the values for the acrylic disk in the lung region, there was improvement for SNR values of the aluminum disk in the heart with the use of an anti-scatter grid and with
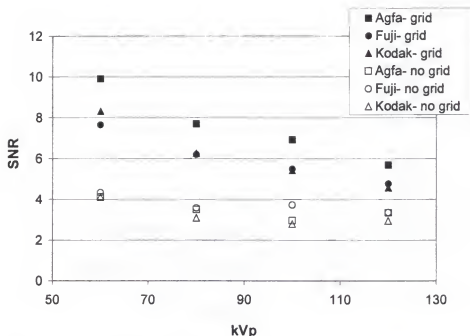
Figure 5-6 SNR measurements as a function of x-ray tube potential for a 4-mm thick aluminum disk in the heart region of the ABC phantom imaged with the low beam quality x-ray unit

decreasing kVp for all CR systems. The improvements were larger for the heart region and the aluminum disks. The improvement with the use of a grid was approximately 90% for the aluminum disk in the heart region. SNR values decreased by approximately 30% as the kVp was increased from 60 kVp to 120 kVp.

Relative-kVp SNR values were calculated by dividing the SNR value at a particular kVp by the SNR value at 80 kVp for the same CR system and grid conditions. Relative-kVp SNR values for the aluminum disk in the heart region of the ABC phantom are shown in Table 5-9. The absolute SNR values for aluminum disks in the heart region of the ABC phantom for images produced with the Agfa CR system and an anti-scatter grid were consistently higher than those produced with the Kodak and Fuji CR systems.

The relative-kVp SNR values showed that the change in SNR as a function of x-ray beam

kVp was consistent for all CR systems.

Table 5-9 Relative-kVp SNR values for aluminum disks in the heart region of the ABC phantom

Grid Use	kVp	SNR$_{kVp}$/SNR$_{80 kVp}$						
		Agfa Set 1	Agfa Set 2	Kodak Set 1	Kodak Set 2	Kodak Set 3	Fuji	Average values
Yes	60	1.29	1.45	1.33	1.30		1.23	1.32±0.07
	80	1.00	1.00	1.00	1.00		1.00	(reference)
	100	0.90	0.90	0.87	0.85		0.89	0.88±0.02
	120	0.74	0.86	0.73	0.74		0.77	0.77±0.05
No	60	1.18	1.26	1.34	1.34	1.40	1.21	1.29±0.08
	80	1.00	1.00	1.00	1.00	1.00	1.00	(reference)
	100	0.85	0.80	0.91	0.93	0.98	1.04	0.92±0.08
	120	0.96	0.90	0.96	1.00	1.10	0.94	0.98±0.06

Figure 5-7 shows the SNR values as a function of kVp for the 10-mm thick acrylic

disk in the lung region of the LBC phantom with the low beam quality x-ray unit. The

SNR values measured with the use of an anti-scatter grid were significantly higher than

non-grid SNR values for all CR systems, improving values by a factor of approximately

Figure 5-7 SNR measurements as a function of x-ray tube potential for a 10-mm thick acrylic disk in the lung region of the LBC phantom imaged with the low beam quality x-ray unit

2.6. SNR values also improved with use of a lower kVp. SNR values decreased by approximately 35% as the kVp is increased from 60 kVp to 120 kVp.

Relative-kVp SNR values were calculated by dividing the SNR value at a particular kVp by the SNR value at 80 kVp for the same CR system and grid conditions. Relative-kVp SNR values for the acrylic disk in the lung region of the LBC phantom are shown in Table 5-10, including repeated results acquired with the Kodak and Agfa CR systems. Relative-kVp SNR values at a given kVp were somewhat consistent among different CR systems.

Table 5-10 Relative-kVp SNR values for acrylic disk in the lung region of the LBC phantom

Grid Use	kVp	$SNR_{kVp}/SNR_{80\ kVp}$					
		Agfa Set 1	Agfa Set 2	Kodak Set 1	Kodak Set 2	Fuji	Average values
Yes	60	1.28	1.10	1.27	1.26	1.15	1.21±0.07
	80	1.00	1.00	1.00	1.00	1.00	(reference)
	100	0.60	0.76	0.85	0.83	0.83	0.77±0.09
	120	0.99	0.67	0.77	0.77	0.75	0.79±0.11
No	60	1.28		1.35	1.44	1.16	1.31±0.10
	80	1.00		1.00	1.00	1.00	(reference)
	100	0.86		0.93	0.80	0.77	0.84±0.06
	120	0.60		1.00	0.93	0.81	0.84±0.15

Figure 5-8 shows SNR values as a function of kVp for the 18-mm thick aluminum disk in heart region of the LBC phantom. Again there was improvement for SNR values of the aluminum disk in the heart with the use of an anti-scatter grid and with decreasing kVp for all CR systems. The SNR values measured with the use of an anti-scatter grid were significantly higher than non-grid SNR values for all CR systems, improving values by a factor of approximately 3.7. SNR values also improved with use of a lower kVp.

SNR values decreased by approximately 37% as the kVp was increased from 60 kVp to 120 kVp.
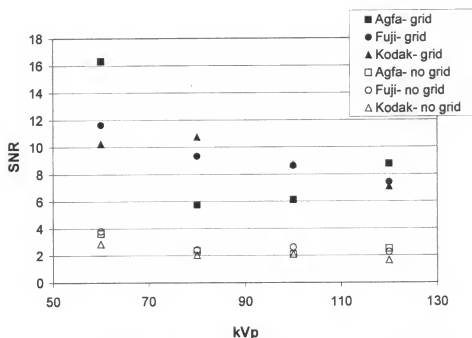
Figure 5-8 SNR measurements as a function of x-ray tube potential of a 18-mm thick aluminum disk in the heart region of the LBC phantom imaged with the low beam quality x-ray unit

Relative-kVp SNR values were calculated by dividing the SNR at a particular kVp by the SNR at 80 kVp for the same CR system and grid conditions. Relative-kVp SNR values for the aluminum disk in the heart region of the LBC phantom are shown in Table 5-11. The first set of relative-kVp SNR values for the Agfa CR acquired with a grid was much higher than other data. These results were due to an unusually low SNR value at 80 kVp which was used for normalization. Therefore, each of the average relative values calculated for the grid data excluded this highest value, obviously an outlier.

Table 5-11 Relative-kVp SNR values for aluminum disk in the heart region of the LBC phantom

Grid Use	kVp	$SNR_{kVp}/SNR_{80\,kVp}$					
		Agfa Set 1	Agfa Set 2	Kodak Set 1	Kodak Set 2	Fuji	Average values
Yes	60	2.84	0.91	0.95	1.30	1.25	1.10±0.17*
	80	1.00	1.00	1.00	1.00	1.00	(reference)
	100	1.06	0.74	0.81	0.85	0.92	0.83±0.07*
	120	1.52	0.70	0.66	0.70	0.79	0.71±0.05*
No	60	1.54	N/A	1.42	1.16	1.57	1.42±0.16
	80	1.00	N/A	1.00	1.00	1.00	(reference)
	100	0.89	N/A	1.03	0.83	1.08	0.96±0.10
	120	1.07	N/A	0.81	0.97	0.93	0.95±0.09

*Grid average values were computed without the highest relative-kVp SNR value.

Although both grid and non-grid SNR values decreased about 37% as the kVp was increased from 60 to 120 kVp, the relative-kVp SNR values showed that the decrease in the grid data was much more gradual. The non-grid data show a large decrease between 60 and 80 kVp, and very little change at higher kVps.

5.3.2 Effect of Anti-Scatter Grid on SNR Measurements

Three different anti-scatter grids were used in the collection of SNR data. The grid data shown in Figures 5-5 through 5-8 were collected using an 8:1, focused grid for Agfa and Kodak CR systems and a 4:1 parallel grid for the Fuji CR system. Figures 5-5 and 5-6 show absolute SNR values for acrylic disks in the lung region and aluminum disks in the heart region of the ABC phantom. Figures 5-7 and 5-8 show absolute SNR values for acrylic disks in the lung region and aluminum disks in the heart region of the LBC phantom. Improvements in varying degrees were seen in all data with the use of an anti-scatter grid. Clinical evaluations were later performed with a 3:1 grid ratio, parallel grid, and SNR measurements for selected data were repeated with this new grid.

For each kVp, relative-grid SNR values, which showed the amount of improvement in SNR with grid use, were computed as the ratio of the SNR measured with the grid to the SNR measured without the grid. Relative-grid SNR values for the acrylic disk in the lung region of the ABC phantom are shown in Table 5-12, including values measured with the 3:1 ratio grid. All relative-grid SNR values were greater than one, which indicates improvement of SNR with grid use; however, values did not improve with increased grid ratio as one might expect. The improvements in SNR with grid-use were approximately 26%, 40% and 62% for grid ratios of 8:1, 4:1 and 3:1, respectively. Relative-grid SNR values ranged from 1.05 to 2.51.

Table 5-12 Relative-grid SNR values for a 4-mm thick acrylic disk in the lung region of the ABC phantom

| kVp | $SNR_{grid}/SNR_{no\ grid}$ | | | | | |
| | 8:1 grid | | 4:1 grid | 3:1 grid | | |
	Agfa	Kodak	Fuji	Agfa	Kodak	Kodak (mobile x-ray unit)
60	1.05	1.07	1.53	1.21	1.44	1.21
80	1.26	1.57	1.38	1.09	2.38	1.17
100	1.25	1.56	1.39	1.22	1.89	2.25
120	1.26	1.03	1.29	1.15	1.87	2.51
$\bar{x} \pm \sigma_x$	1.2±0.1	1.3±0.3	1.4±0.1	1.2±0.1	1.9±0.3	1.8±0.6

Relative-grid SNR values for the aluminum disk in the heart region of the ABC phantom are shown in Table 5-13, including values measured with the 3:1 grid. All relative-grid SNR values showed improvement with grid use, and values increased with increasing grid ratio. SNR values improved by an average factor of 2.0 when the 8:1 grid was used, as compared with an improvement factor of 1.5 with the 3:1 grid.

Table 5-13 Relative-grid SNR values for a 4-mm thick aluminum disk in the heart region of the ABC phantom

kVp	$SNR_{grid}/SNR_{no\ grid}$					
	8:1 grid		4:1 grid	3:1 grid		
	Agfa	Kodak	Fuji	Agfa	Kodak	Kodak (mobile x-ray unit)
60	2.40	2.02	1.76	1.72	1.67	1.44
80	2.20	2.03	1.73	1.49	1.73	1.30
100	2.34	1.94	1.47	1.68	1.59	1.47
120	1.70	1.55	1.42	1.43	1.28	1.26
$\bar{x} \pm \sigma_x$	2.2±0.3	1.9±0.2	1.6±0.2	1.6±0.1	1.6±0.2	1.4±0.1

The improvement in SNR with grid ratio for the heart region indicated that the scattered radiation in the heart region was greater than the scattered radiation in the lung region, which is consistent with S/P ratios measured in these regions, and that reduced scatter transmission was helpful. Relative-grid SNR values ranged from 1.26 to 2.40. Although the dependence on beam energy was not consistent, relative values at 120 kVp were lower, indicating that grid use was not as beneficial at 120 kVp.

Relative-grid SNR values for the acrylic disk in the lung region of the LBC phantom are shown in Table 5-14, including values measured with the 3:1 grid. All relative-grid SNR values showed improvement with grid use, and values increased with increasing grid ratio. SNR values improved by an average factor of 2.6 when the 8:1 grid was used, as compared with an improvement factor of 1.9 with the 3:1 grid. This result indicated a significant level of scattered radiation in the LBC phantom and demonstrated that reduced scatter transmission was helpful. Relative-grid SNR values ranged from 1.42 to 3.38 and were independent of beam energy.

Table 5-14 Relative-grid SNR values for a 10-mm thick acrylic disk in the lung region of the LBC phantom

kVp	SNR$_{grid}$/SNR$_{no\ grid}$					
	8:1 grid		4:1 grid	3:1 grid		
	Agfa	Kodak	Fuji	Agfa	Kodak	Kodak (mobile x-ray unit)
60	2.05	2.98	2.78	1.60	1.83	2.16
80	2.05	3.18	2.80	1.85	2.09	2.15
100	1.42	2.90	3.01	1.63	2.16	1.84
120	3.38	2.43	2.61	2.07	1.73	1.70
$\bar{x} \pm \sigma_x$	2.2±0.7	2.9±0.3	2.8±0.1	1.8±0.2	2.0±0.2	2.0±0.2

Relative-grid SNR values for the aluminum disk in the heart region of the LBC phantom are shown in Table 5-15, including values measured with the 3:1 grid. All relative-grid SNR values showed improvement with grid use, and values increased with increasing grid ratio. SNR values improved by an average factor of 3.8 when the 8:1 grid was used, as compared with an improvement factor of 2.0 with the 3:1 grid.

Table 5-15 Relative-grid SNR values for an 18-mm thick aluminum disk in the heart region of the LBC phantom

kVp	SNR$_{grid}$/SNR$_{no\ grid}$					
	8:1 grid		4:1 grid	3:1 grid		
	Agfa	Kodak	Fuji	Agfa	Kodak	Kodak (mobile x-ray unit)
60	4.50	3.56	3.06	1.52	2.28	2.10
80	2.45	5.29	3.86	2.59	2.04	2.03
100	2.91	4.16	3.29	2.14	2.07	1.88
120	3.49	4.30	3.30	1.70	1.47	1.70
$\bar{x} \pm \sigma_x$	3.3±0.8	4.3±0.6	3.4±0.3	2.0±0.4	2.0±0.3	1.9±0.2

This result indicated a significant level of scattered radiation in the LBC phantom and implied that reduced scatter transmission improves SNR. Relative-grid SNR values ranged from 1.47 to 5.29 and were independent of beam energy, except for the 3:1 grid

relative-grid SNR values, which were approximately 20% lower at 120 kVp than at other kVps.

5.3.3 Effect of Added Aluminum Filtration on SNR Measurements

The effects on the SNR of changing the x-ray spectra by modifying beam filtration were studied for the Agfa and Kodak CR systems. Using Room 1 at Shands at UF, beam filtration was increased from the standard by adding 1 mm of aluminum filtration to the x-ray beam. Filtration could not be removed from the collimator in Room 1. Therefore, Room 9 at Shands at UF was used for the low-filtration (-1) condition. The HVLs for −1, standard (0), and +1 mm aluminum filtration at 80 kVp were measured and found to be 3.2, 3.6 and 4.1 mm of aluminum, respectively. The following results include data acquired on the Agfa and Kodak CR systems with the three filtrations. Figure 5-9 shows the effect of beam filtration on the SNR for a 4-mm thick acrylic disk in the lung region of the ABC phantom imaged without use of an anti-scatter grid. The low-beam filtration condition, comparable to removing 1 mm aluminum filtration from the x-ray beam, slightly improved the SNR overall for images created with and without the use of an anti-

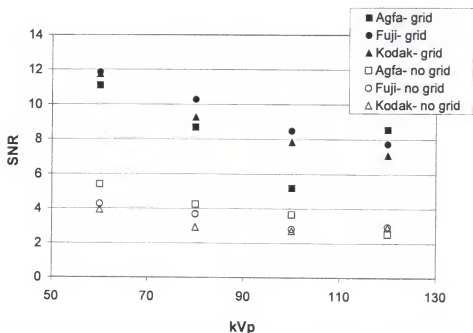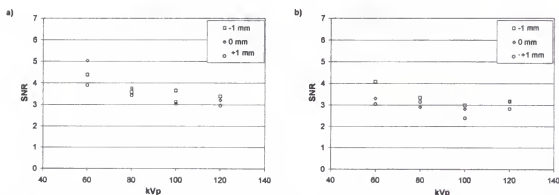Figure 5-9 SNR as a function of tube potential for a 4 mm-thick acrylic disk in the lung region of the ABC phantom with differing amounts of added aluminum filtration with no grid

a) Agfa CR; b) Kodak CR.

scatter grid.

Relative-filtration SNR values, which showed the change in SNR as a function of added aluminum filtration, were computed as the ratio of the SNR value measured with the high or low filtration conditions compared to the SNR value measured with the standard aluminum filtration in the x-ray beam. Relative-filtration SNR values for the acrylic disk in the lung region of the ABC phantom are shown in Table 5-16.

Because of the similarity in absolute SNR values at different beam qualities, the relative-filtration SNR values were not very different. Relative-filtration SNR values ranged from 0.73 to 1.40, and showed inconsistent changes with differences in beam quality. When the low-HVL condition (-1) was used rather than the standard (0), there was less than a 10% change in SNR values in 9 out of 16 cases. There was improvement in SNR with lower beam quality in 6 out of 16 cases and a decrease in one case. When high-filtration (+1) was used rather than standard filtration (0), there was less than a 10% change in SNR values in 6 out of 16 cases. There was a decrease in SNR with high beam quality in 7 out of 16 cases and an improvement in SNR in 3 out of 16 cases.

Table 5-16 Relative-filtration SNR values for a 4-mm acrylic disk in the lung region of the ABC phantom

kVp	$SNR_{filtration}/SNR_{standard\ filtration}$							
	Grid used				No grid used			
	SNR_{-1}/SNR_0		SNR_{+1}/SNR_0		SNR_{-1}/SNR_0		SNR_{+1}/SNR_0	
	Agfa	Kodak	Agfa	Kodak	Agfa	Kodak	Agfa	Kodak
60	1.00	0.96	0.97	1.34	0.87	1.23	0.77	0.91
80	1.09	1.19	0.76	1.10	0.97	1.15	0.92	0.89
100	1.40	1.29	1.05	1.11	1.17	1.06	1.00	1.11
120	1.09	0.94	0.80	0.89	1.01	1.00	0.88	0.73

Figure 5-10 shows the effect of added aluminum filtration on the SNR of a 4-mm

thick aluminum disk in the heart region of the ABC phantom with use of an anti-scatter

grid. As above, the effects were inconsistent and small.
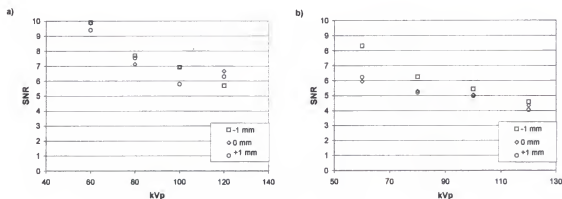
Figure 5-10 SNR as a function of tube potential for a 4 mm-thick aluminum disk in the heart region of the ABC phantom with differing amounts of added aluminum filtration. a) Agfa CR; b) Kodak CR.

Relative-filtration SNR values for the aluminum disk in the heart region of the

ABC phantom are shown in Table 5-17. Relative-filtration SNR values ranged from 0.84

to 1.66. When the low-HVL condition (-1) was used rather than the standard (0), there

was less than a 10% change in SNR values in 8 out of 16 cases. There was improvement

in SNR with lower beam quality in 6 out of 16 cases and a decrease in two cases. When

high-filtration (+1) was used rather than standard filtration (0), there was less than a 10%

change in SNR values in 13 out of 16 cases. There was a decrease in SNR with high beam

quality in 1 case and an improvement in SNR in 2 out of 16 cases.

Table 5-17 Relative-filtration SNR values for a 4-mm aluminum disk in the heart region of the ABC phantom

kVp	$SNR_{filtration}/SNR_{standard\ filtration}$							
	Grid used				No grid used			
	SNR_{-1}/SNR_0		SNR_{+1}/SNR_0		SNR_{-1}/SNR_0		SNR_{+1}/SNR_0	
	Agfa	Kodak	Agfa	Kodak	Agfa	Kodak	Agfa	Kodak
60	1.00	1.40	0.95	1.05	0.87	1.04	0.99	0.96
80	1.08	1.18	1.06	0.98	0.97	1.19	0.99	1.21
100	1.00	1.08	0.84	0.95	0.92	1.20	0.95	1.10
120	0.86	1.05	0.95	0.93	1.66	1.24	1.42	1.04

Figure 5-11 shows the effect of beam filtration on the SNR for a 10-mm thick acrylic disk in the lung region of the LBC phantom imaged without use of an anti-scatter grid. Data from the Agfa CR had inconsistent trends for the images acquired with different kVp settings; however, the low filtration condition improved the overall SNR for most images created with and without the use of an anti-scatter grid. As before, the effect was small.
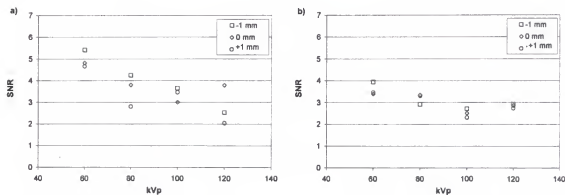
Figure 5-11 SNR as a function of tube potential for a 10 mm-thick acrylic disk in the lung region of the LBC phantom with differing amounts of added aluminum filtration.
a) Agfa CR; b) Kodak CR.

Relative-filtration SNR values for the acrylic disk in the lung region of the LBC phantom are shown in Table 5-18. As a group, relative-filtration SNR values improved ~7% with use of less aluminum filtration, and decreased ~6% with use of more added aluminum filtration; however, individual variations occurred. When the low-HVL condition (-1) was used rather than the standard (0), there was less than a 10% change in SNR values in 5 out of 16 cases. There was improvement in SNR with lower beam quality in 8 out of 16 cases and a decrease in 3 cases. When high-filtration (+1) was used rather than standard filtration (0), there was less than a 10% change in SNR values in 9 out of 16 cases. There was a decrease in SNR with high beam quality in 5 out of 16 cases and an improvement in SNR in 2 out of 16 cases.

Table 5-18 Relative-filtration SNR values for a 10-mm acrylic disk in the lung region of the LBC phantom

kVp	$SNR_{filtration}/SNR_{standard\ filtration}$							
	Grid used				No grid used			
	SNR_{-1}/SNR_0		SNR_{+1}/SNR_0		SNR_{-1}/SNR_0		SNR_{+1}/SNR_0	
	Agfa	Kodak	Agfa	Kodak	Agfa	Kodak	Agfa	Kodak
60	1.38	1.32	1.08	0.95	1.12	1.16	0.97	1.02
80	1.31	0.94	1.28	0.88	1.12	0.87	0.74	0.99
100	0.62	0.94	0.81	0.77	1.22	1.08	1.15	0.92
120	1.29	1.09	0.99	0.95	0.67	1.02	0.54	0.95

Figure 5-12 shows the effect of added aluminum filtration on the SNR of an 18-mm thick aluminum disk in the heart region of the LBC phantom with use of an anti-scatter grid. The low filtration condition significantly decreased SNR values with Agfa-grid images.

Relative-filtration SNR values for the aluminum disk in the heart region of the LBC phantom are shown in Table 5-19. There was a decrease of ~30% in SNR values
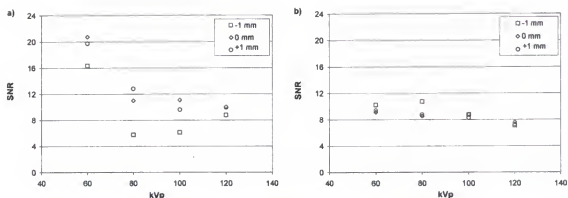
Figure 5-12 SNR as a function of tube potential for an 18-mm thick aluminum disk in the heart region of the LBC phantom with differing amounts of added aluminum filtration.

a) Agfa CR; b) Kodak CR.

measured for Agfa-grid images acquired with the low filtration condition (-1). All other

changes in relative-filtration SNR were inconsistent with changes in beam quality. Half of

the remaining 28 relative values changed by less than 10%.

Table 5-19 Relative-filtration SNR values for a 18-mm aluminum disk in the heart region of the LBC phantom

kVp	$SNR_{filtration}/SNR_{standard\ filtration}$							
	Grid used				No grid used			
	SNR_{-1}/SNR_0		SNR_{+1}/SNR_0		SNR_{-1}/SNR_0		SNR_{+1}/SNR_0	
	Agfa	Kodak	Agfa	Kodak	Agfa	Kodak	Agfa	Kodak
60	0.79	1.12	0.95	1.03	1.20	1.14	0.53	0.97
80	0.52	1.26	1.16	1.03	0.79	0.95	0.98	0.97
100	0.55	0.99	0.87	0.93	1.54	1.08	1.58	1.02
120	0.88	0.93	0.99	0.95	0.95	0.83	0.80	0.60
Average	0.69	1.08	0.99	0.99	1.12	1.00	0.97	0.89

5.4 System Monitoring

A drop in the Exposure Index produced by the Kodak CR system was noticed

clinically during the time period following the collection of SNR data. Selected SNR

measurements were therefore repeated to examine the effect of the apparent loss of efficiency on the SNR of images.

Phantom images exposed with the same x-ray tube at the same technique settings showed a drop in Exposure Index of approximately 70 (from 1780 to 1710 for 80 kVp). The SNR values were lower than initial measurements, as seen in Table 5-20. A calibration procedure was performed on March 14, 2001 to reset the PMT gains on the Kodak CR system, and the SNR experiment was repeated again. The resultant Exposure Indices produced by the newly calibrated system were significantly higher (increasing by ~160), and the SNR values were also improved but not to the levels of 4 months prior.

Table 5-20 SNR results from repeat measurements for the Kodak 400 CR system.

kVp	mAs	[1]Date	Exposure Index	Acrylic disk– lung			Aluminum disk- heart		
				SNR	Signal	Noise	SNR	Signal	Noise
60	5	Date 1	1810	4.08	66	16	4.12	125	30
		Date 2	1610	3.10	57	18	3.55	134	38
		[2]Date 3	1890	3.28	59	18	3.67	113	31
81	1.4	Date 1	1780	3.34	65	20	3.08	96	31
		Date 2	1710	1.91	40	21	2.64	84	32
		[2]Date 3	1870	2.80	59	21	2.63	83	31
99	0.71	Date 1	1770	2.99	64	21	2.80	87	31
		Date 2	1700	1.89	43	23	2.45	80	33
		[2]Date 3	1860	2.78	64	23	2.59	84	32
121	0.56	Date 1	1900	3.18	65	21	2.95	80	27
		Date 2	1850	2.07	44	21	2.65	76	29
		[2]Date 3	1980	3.02	68	22	2.88	81	28

[1]Dates 1, 2 and 3 refer to 11/13/00, 3/13/01 and 3/21/01, respectively.
[2]Post-calibration

SNR images with the same imaging parameters were also repeated for the Agfa ADC Compact. The SNR values for the two measurement dates are shown in Table 5-21. SNR values remained relatively stable for this unit over the 4-month period.

Table 5-21 SNR results from repeat measurements for the Agfa ADC Compact.

kVp	mAs	*Date	Exposure Level	Acrylic disk– lung			Aluminum disk- heart		
				SNR	Signal	Noise	SNR	Signal	Noise
60	5	Date 1	2.69	4.38	105	24	4.13	65	16
		Date 2	2.66	3.95	95	24	4.59	65	14
81	1.4	Date 1	2.66	3.59	90	25	3.50	59	17
		Date 2	2.62	3.41	89	26	3.64	58	16
99	0.71	Date 1	2.66	3.66	98	27	2.96	52	18
		Date 2	2.62	3.43	99	29	2.91	52	18
121	0.56	Date 1	2.72	3.39	83	24	3.35	54	16
		Date 2	2.72	3.71	87	23	3.26	49	15

*Dates 1 and 2 refer to 11/10/00 and 3/13/01, respectively.

The relative SNR performance of the Kodak CR system, such as the effect of kVp, was not affected by the drop in absolute SNR values as is shown by relative-kVp SNR values tabulated in Table 5-22. Relative-kVp SNR values were calculated as the ratio of an SNR value at a particular kVp divided by the SNR value at 80 kVp. With one exception, the tabulated ratios were reproducible within 0.1, showing that the effect of kVp on SNR could be evaluated on one measurement date, even though the absolute SNR values were different.

Table 5-23 shows relative-kVp SNR values measured for the Agfa CR. Calculated ratios were reproducible within 0.1 and again demonstrated that the relative effect of a change in imaging parameter could be evaluated from absolute measurements performed all at one time.

5.5 Effective Dose

As described in Section 4.9, changes in phantom dose as a function of modifications in image quality were assessed. Two sets of measurements of effective dose were made: one for the ABC phantom and one for the LBC phantom.

Table 5-22 Repeat measurements of relative-kVp SNR values for the Kodak CR

kVp	mAs	[1]Date	Exposure Index	Acrylic disk– lung SNR_{kVp}/SNR_{80}	Aluminum disk- heart SNR_{kVp}/SNR_{80}
60	5	Date 1	1810	1.2	1.3
		Date 2	1610	1.6	1.3
		[2]Date 3	1890	1.2	1.4
81	1.4	Date 1	1780	1.0	1.0
		Date 2	1710	1.0	1.0
		[2]Date 3	1870	1.0	1.0
99	0.71	Date 1	1770	0.9	0.9
		Date 2	1700	1.0	0.9
		[2]Date 3	1860	1.0	1.0
121	0.56	Date 1	1900	1.0	1.0
		Date 2	1850	1.1	1.0
		[2]Date 3	1980	1.1	1.1

[1]Dates 1, 2 and 3 refer to 11/13/00, 3/13/01 and 3/21/01, respectively.
[2]Post-calibration

Table 5-23 Repeat measurements of relative-kVp SNR values for the Agfa CR

kVp	mAs	*Date	Exposure Level	Acrylic disk– lung SNR_{kVp}/SNR_{80}	Aluminum disk- heart SNR_{kVp}/SNR_{80}
60	5	Date 1	2.69	1.2	1.2
		Date 2	2.66	1.2	1.3
81	1.4	Date 1	2.66	1.0	1.0
		Date 2	2.62	1.0	1.0
99	0.71	Date 1	2.66	1.0	0.8
		Date 2	2.62	1.0	0.8
121	0.56	Date 1	2.72	0.9	1.0
		Date 2	2.72	1.0	0.9

*Dates 1 and 2 refer to 11/10/00 and 3/13/01, respectively.

5.5.1 ABC Phantom

Table 5-24 summarizes the effect of changes in imaging parameters on the

entrance air kerma and effective dose to the ABC phantom. Entrance air kerma

measurements were made at 70 cm from the x-ray tube focal spot without backscatter.

These measurements were corrected for distance to the entrance plane of the ABC

phantom, which was located at a distance of 74.4 cm from the x-ray tube focal spot in the experimental setup. The effective dose to the phantom increased by a factor of approximately 3 to 4 when an 8:1, 33 lines/cm anti-scatter grid was used to image the ABC phantom, compared to no-grid imaging techniques.

Table 5-24 Summary of effective dose and entrance air kerma to the ABC phantom with and without 8:1 grid as imaging parameters were adjusted to maintain constant exposure to the CR plate

8:1 Grid used	Added filtration (mm)	HVL (mm Al)	kVp	mAs	Output (μGy/mAs) at 70 cm	Entrance air kerma (μGy) for ABC phantom	Effective Dose (μSv)
Yes	-1	2.40	60	20	60	1070	161
Yes	-1	3.18	81	5.6	114	565	115
Yes	-1	3.88	99	2.8	169	417	101
Yes	-1	4.73	121	1.6	246	348	96
Yes	0	2.67	60	20	46	817	133
Yes	0	3.61	80	6.0	92	487	109
Yes	0	4.45	100	3.0	150	400	105
Yes	0	5.29	120	1.8	213	339	100
Yes	+1	3.02	60	21.6	35	678	122
Yes	+1	4.14	80	6.4	75	426	104
Yes	+1	5.11	100	3.2	124	357	102
Yes	+1	5.94	120	2.0	181	322	101
No	-1	2.40	60	5.0	60	270	40
No	-1	3.18	81	1.4	114	139	29
No	-1	3.88	99	0.71	169	104	26
No	-1	4.73	121	0.56	246	122	34
No	0	2.67	60	6.4	46	261	43
No	0	3.61	80	2.0	92	165	36
No	0	4.45	100	1.0	150	130	35
No	0	5.29	120	0.6	213	113	33
No	+1	3.02	60	7.0	35	217	40
No	+1	4.14	80	2.25	75	148	37
No	+1	5.11	100	1.13	124	122	36
No	+1	5.94	120	0.6	181	96	30

Table 5-25 shows the technique factors that were used with a 3:1, 41 lines/cm grid to image the ABC phantom, to maintain an entrance air kerma to the CR plate of approximately 8.7 μGy. Only the low beam quality x-ray unit (Room 9) was used to evaluate the 3:1 grid because the x-ray beam more closely resembled that of the mobile unit at a higher kVp (HVL$_{Room9}$ at 81 kVp = 3.2 mm Al, HVL$_{mobile}$ at 100 kVp = 3.2 mm Al). The effective dose with the use of the 3:1 grid increased by a factor of approximately 2 to 2.5, compared to no-grid imaging techniques.

Table 5-25 Effective dose and entrance air kerma to the ABC phantom with 3:1 grid used for clinical evaluation, maintaining constant exposure to the CR plate

3:1 Grid used	Added filtration (mm)	HVL (mm Al)	kVp	mAs	Output (μGy/mAs) at 70 cm	ESE (μGy) for ABC phantom	Effective Dose (μSv)
Yes	-1	2.40	60	12.5	60	670	101
Yes	-1	3.18	81	3.6	114	365	74
Yes	-1	3.88	99	1.8	169	270	65
Yes	-1	4.73	121	1.1	246	243	66

5.5.2 <u>LBC Phantom</u>

Table 5-26 summarizes the effect of changes in imaging parameters on the effective dose and entrance air kerma to the LBC phantom. Entrance air kerma measurements were made at 70 cm from the x-ray tube focal spot without backscatter. These measurements were corrected for distance to the entrance plane of the LBC phantom, which was located at a distance of 66.8 cm from the x-ray tube focal spot in the experimental setup. The effective dose to the phantom increased by a factor of approximately 6 when an 8:1, 33 lines/cm anti-scatter grid was used to image the LBC phantom, compared to no-grid imaging techniques.

Table 5-26 Summary of effective dose and entrance air kerma to the LBC phantom as imaging parameters were adjusted to maintain constant exposure to the CR plate

Grid used	Added filtration (mm)	HVL (mm Al)	kVp	mAs	Output (μGy/mAs) at 70 cm	ESE (μGy) for LBC phantom	Effective Dose (μSv)
Yes	-1	2.40	60	100	60	7722	528
Yes	-1	3.18	81	22	114	3217	303
Yes	-1	3.88	99	11	169	2383	271
Yes	-1	4.73	121	5.0	246	1583	207
Yes	0	2.67	60	120	46	7087	526
Yes	0	3.61	80	25	92	2957	305
Yes	0	4.45	100	11	150	2122	264
Yes	0	5.29	120	6.0	213	1643	231
Yes	+1	3.02	60	125	35	5678	464
Yes	+1	4.14	80	28	75	2687	306
Yes	+1	5.11	100	11	124	1757	240
Yes	+1	5.94	120	6.0	181	1391	211
No	-1	2.40	60	14	60	1078	74
No	-1	3.18	81	3.6	114	530	50
No	-1	3.88	99	1.8	169	391	44
No	-1	4.73	121	1.1	246	348	46
No	0	2.67	60	16	46	948	70
No	0	3.61	80	4.0	92	470	49
No	0	4.45	100	2.0	150	383	48
No	0	5.29	120	1.2	213	330	46
No	+1	3.02	60	18	35	817	67
No	+1	4.14	80	4.5	75	435	49
No	+1	5.11	100	2.0	124	322	44
No	+1	5.94	120	1.2	181	278	42

Table 5-27 shows the technique factors that were used with a 3:1, 41 lines/cm grid to image the LBC phantom, to maintain an entrance air kerma to the CR plate of approximately 8.7 μGy. The effective dose with the use of the 3:1 grid increased only by a factor of approximately 2.7, compared to no-grid imaging techniques. The techniques used with the LBC phantom and the 3:1 grid are less than half the techniques required with use of the 8:1 grid with the LBC phantom.

Table 5-27 Effective dose and entrance air kerma to the LBC phantom with 3:1 grid used for clinical evaluation, maintaining constant exposure to the CR plate

Grid used	Added filtration (mm)	HVL (mm Al)	kVp	mAs	Output (μGy/mAs) at 70 cm	ESE (μGy) for LBC phantom	Effective Dose (μSv)
Yes	-1	2.40	60	40	60	3087	211
Yes	-1	3.18	81	11	114	1609	151
Yes	-1	3.88	99	4.5	169	974	111
Yes	-1	4.73	121	2.5	246	791	104

5.6 Modulation Transfer Function

The MTFs of CR chest images were measured in the three regions of the ABC phantom using the square wave response method developed by Droege and Morin (47). For the test pattern used, this method produced the system response for spatial frequencies of 0.5 cycles/mm and greater. The MTF at frequencies below 0.5 cycles/mm were not well estimated with this method because of the approximation that was used (47). MTF results were normalized by dividing by the MTF at the lowest spatial frequency. The results shown here pertain to MTF results in the lung and heart regions of the ABC phantom performed with the Agfa CR under various imaging conditions. MTF measurements were also made in the subdiaphragm region of the ABC phantom. As described in Section 5.1, the subdiaphragm region was included in the phantom for the primary purpose of creating the proper histogram for the CR systems to process the phantom images as chest images and not because of clinical interest in this region in chest radiography. The MTF data for this region are presented in Appendix E.

5.6.1 Effects of kVp on MTF

Figure 5-13 shows the overall MTF in the lung and heart regions of the ABC phantom imaged with the Agfa CR and an anti-scatter grid. The curves include
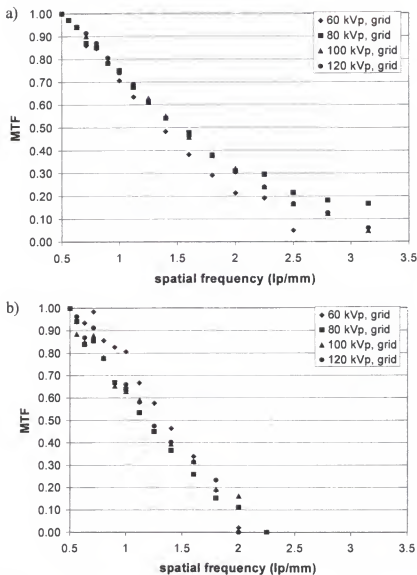
Figure 5-13 MTF measured with the ABC phantom and an anti-scatter grid.
a) lung region; b) heart region

contributions of the phantom material; hence, MTF values are lower in the heart region, where much more scattered radiation is produced. The curves show that the MTF changes are small with variation of x-ray tube potential, especially at low spatial frequencies. The MTF curve imaged with 60 kVp is lower in the lung region than the MTF curves acquired with 80, 100 and 120 kVp. The areas under the MTF curves produced with use of an anti-scatter grid indicate the same result and are presented in Table 5-28.

Table 5-28 Area under the MTF curves measured with the ABC phantom with an anti-scatter grid

X-ray tube potential	Area under MTF curve	
	Lung region	Heart region
60	8.6	7.0
80	11.0	6.6
100	10.3	6.9
120	10.3	6.8

Figure 5-14 shows the MTF for frequencies greater than 0.5 cycles/mm in the lung and heart regions measured without an anti-scatter grid. The changes in these curves are small over the range of kVps evaluated. The image in the lung region taken at 60 kVp has the lowest MTF, particularly at higher spatial frequencies, although the difference is small. The differences can be quantified with the calculated areas under these curves, which are presented in Table 5-29. These areas are very similar to those calculated for the grid MTF curves.

The heart region curves are not smooth and contain systematic humps at every third data point. These discontinuities are due to the position of the cyclic bar pattern in the heart region and the amount of scatter at that position. The lead bar pattern contains 7 rows with 3 groups of lead bar spacings in each row as diagrammed in Figure 5-15. Cyclic bar groups along the right column of the phantom with frequencies (0.5, 0.71, 1.0, 1.4 lp/mm) had an increase in measured pixel value standard deviation, causing an increase in calculated MTF at these frequencies. The pattern was positioned in such a way that this area of the image contained more scattered radiation. This explanation is supported by the fact that similar discontinuities are not seen in images from the lung region, which produces much less scatter than the heart region, nor in the images of the heart region with an anti-scatter grid.
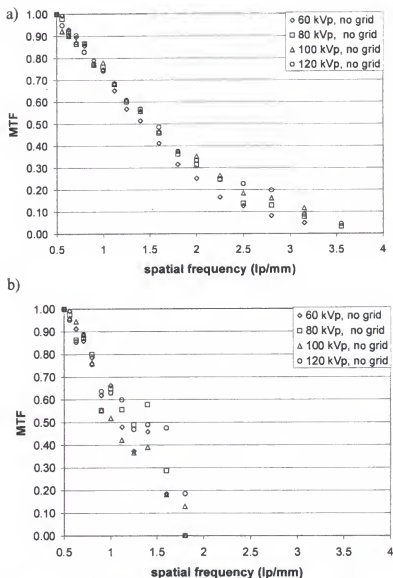
Figure 5-14 MTF measured with the ABC phantom without an anti-scatter grid.
a) lung region; b) heart region

Table 5-29 Area under the MTF curves measured with the ABC phantom without an anti-scatter grid

X-ray tube potential	Area under MTF curve	
	Lung region	Heart region
60	9.4	6.0
80	10.3	6.5
100	10.7	5.9
120	10.9	7.0

0.63	0.56	0.5
0.9	0.8	0.71
1.25	1.12	1.0
1.8	1.6	1.4
2.5	2.24	2.0
3.55	3.15	2.8
5.0	4.5	4.0

Figure 5-15 Diagram of position of cyclic bar groups (lp/mm) in lead bar pattern used for MTF measurements

5.6.2 Effects of Added Aluminum Filtration on MTF

Figure 5-16 shows the MTF in the lung and heart region at 80 kVp as the amount of aluminum filtration was varied. The amount of filtration did not have much affect on the MTF of the CR system. The MTF response in the lung region, with the low filtration condition, was lower than the other MTF filtration curves. This difference is similar to the MTF response at 60 kVp. The decrease in MTF with less aluminum filtration in the lung region is evident in the calculated area under the curve. Areas under MTF curves for each filtration condition are presented in Table 5-30. The areas under the MTF curves measured in the heart region do not vary much, while the area for the reduced filtration condition (-1 mm) in the lung region is lower than other filtration conditions.
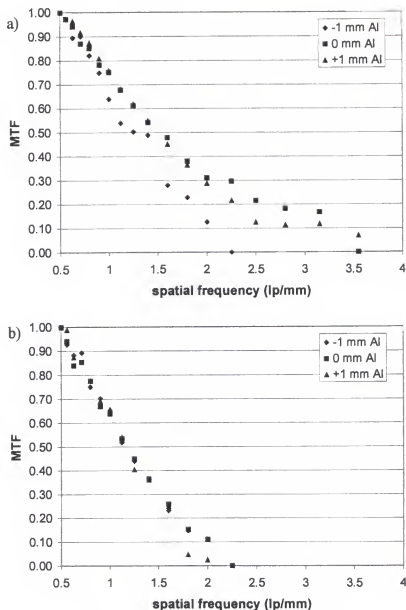
Figure 5-16 MTF measured with the ABC phantom and various amounts of added aluminum filtration in the x-ray beam.
    a) lung region; b) heart region

Table 5-30 Area under the MTF curves measured with the ABC phantom at 80 kVp with an anti-scatter grid and various amounts of added aluminum filtration

Added aluminum filtration	Area under MTF curve	
	Lung region	Heart region
-1 mm	7.2	6.4
0 mm	11.0	6.6
+1 mm	10.5	6.3

5.6.3 <u>Effects of Anti-scatter Grid on MTF</u>

Figure 5-17 shows the MTF measured in the lung and heart regions when the ABC phantom was imaged with 60 and 80 kVp, with and without the use of an anti-scatter grid.
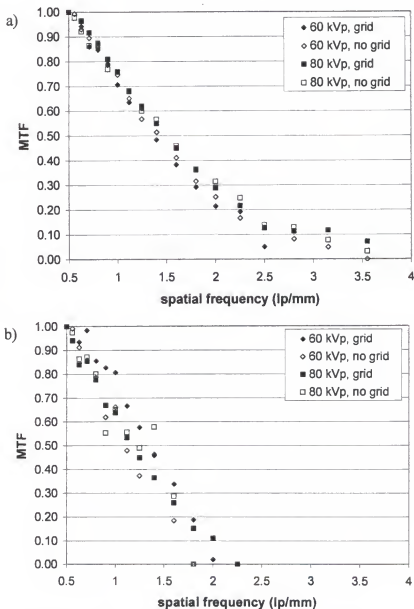
Figure 5-17 MTF measured in the ABC phantom with and without the use of an anti-scatter grid for 60 and 80 kVp
a) lung region; b) heart region

The overall MTF in the lung region was affected very little by the use of an anti-scatter grid. As explained previously, the MTF of the non-grid images in the heart region had a position-related, systematic bump introduced due to scatter that was eliminated by the use of an anti-scatter grid and therefore not seen in the grid images. Table 5-31 lists the areas under the MTF curves produced with and without the grid and again demonstrates that grid-use did not significantly affect the system MTF.

Table 5-31 Area under the MTF curves measured with the ABC phantom with an anti-scatter grid

Chest region	X-ray tube potential (kVp)	Area under MTF curve	
		Grid	No grid
Lung region	60	8.6	9.4
	80	11.0	10.3
	100	10.3	10.7
	120	10.3	10.9
Heart region	60	7.0	6.0
	80	6.6	6.5
	100	6.9	5.9
	120	6.8	7.0

5.7 Clinical Evaluation

A clinical evaluation study was performed with mobile chest CR images of SICU patients in Shands at the UF utilizing a Kodak 400 CR system. Technique settings for mobile chest radiography were varied for comparison with reference technique factors. A 3:1 ratio, 41 lines/cm parallel grid was also evaluated. Radiologists compared the image quality in the lung and heart regions of the adjusted-parameter images with the images of the same patients acquired with typical techniques. A 5-point rating scale, from 5 (much better) to 1 (much worse), was used to indicate the perceived image quality of the adjusted-parameter image as compared to the original image. A score of 3 indicated that

the image quality of the adjusted-parameter image was equivalent to the original image in that region.

5.7.1 Image Collection

Mobile chest radiographs in the AP projection were performed in the SICU on the same patient on consecutive days using different imaging parameters without performing a clinically unnecessary exam. The number of images collected at each adjusted-parameter setting is listed in Table 5-32.

Table 5-32 Number of images collected for each adjusted-parameter setting in the clinical evaluation

Test day	Parameter adjusted	Number of images
Day1	Standard kVp, no grid	12
Day2	Decreased kVp (-10 kVp), no grid	12
Day 3	Standard kVp, grid	8
Day 4	Increased kVp (+15 kVp), no grid	9
Day 5	Increased kVp (+15 kVp), grid	9

5.7.2 Decreased kVp

The effect of lowering the x-ray tube potential on the perceived image quality in mobile chest radiography was evaluated by comparison of images taken at the standard kVp (90 to 95 kVp, depending on patient size) on Day 1 and images taken with a tube potential that was decreased 10 kVp from the original (80 to 85 kVp) on Day 2. The Exposure Index generated by the Kodak CR was used to determine the mAs required for the various patients with the goal of matching the Exposure Index of the original image. The mAs settings were therefore increased by 30-60% when the kVp was decreased by 10 kVp. Table 5-33 summarizes the technique factors used and the corresponding increases in entrance air kerma and effective dose when the kVp was decreased. For dose

calculations, the patient thicknesses were assumed to be 20 cm for average-sized patients

(initial kVp of 90 kVp) and 30 cm for large patients (initial kVp of 95 kVp).

Corresponding patient masses were assumed to be 70.9 kg and 130 kg. Effective dose to

the patient increased by ~17 % with use of the lower kVp. Entrance air kerma values

increased by a larger amount (~29%), which is an indicator of the increase in breast dose

with the lower kVp x-ray beams.

Table 5-33 Summary of low-kVp technique changes used on Day 2 and the resultant
entrance air kerma and effective doses to patients

Number of Patients	Initial kVp	Initial mAs	Entrance air kerma (μGy)	Effective Dose (μSv)	Adjusted kVp	Adjusted mAs	Entrance air kerma (μGy)	Effective Dose (μSv)
4	90	3.2	375	87	80	5	476	101
3	90	4	469	109	80	6.4	609	129
2	95	4	682	73	85	6.4	885	85
3	95	5	852	91	85	6.4	885	85

Tables 5-34 and 5-35 show the image quality ratings assigned by each reader to

the images made at decreased kVp for the lung and heart regions, respectively. Images are

listed in order of increasing patient attenuation. The imaging techniques and the resultant

plate exposure determined patient size order within each group; hence, the order indicates

increasing tissue attenuation rather than physical size.

The average rating for the lung region of images acquired at the decreased kVp

was 3.0, which indicates that the image quality was deemed equivalent to the image

quality in the lung of the original image. Similarly, the average image rating in the heart

region was 2.8, which is nearly equivalent. It should be noted that replicate measurements

would have been required for these patients in order to determine statistical significance

and associated confidence intervals. Replicate measurements were not feasible for this

part of the study. A notable result is that out of 102 individual ratings, 101 were assigned

ratings of 2, 3 or 4. Only once was an image considered "much worse" than the standard-technique image, and never was an image considered "much better."

Table 5-34 Image quality ratings for the lung region of clinical mobile chest CR images acquired at decreased kVp (-10 kVp) on Day 2

Adjusted Techniques		Expo-sure Index	Radiologist							Average Image Rating
kVp	mAs		1	2	3	4	5	6	7	
80	5	1830	4	3	2	2	3			2.8
80	5	1830	4	3	4	2	4			3.4
80	5	1770	3	3	3	2	4	3	2	2.9
80	5	1770	3	3	3	2	3	3	3	2.9
80	6.4	1980	4	3	4	4	4			3.8
80	6.4	1820	3	3	3	2	4	2	2	2.7
80	6.4	1790	3	3	3	4	4	3	3	3.3
85	6.4	2050	4	2	2	2	3			2.6
85	6.4	1970	2	3	4	4	2	4	3	3.1
85	6.4	1820	3	3	4	2	4	4	2	3.1
85	6.4	1800	3	3	3	2	2	3	2	2.6
85	6.4	1760	3	3	4	4	3	4	3	3.4
Average rating for radiologist			3.3	2.9	3.3	2.7	3.3	3.3	2.5	3.0

5.7.3 Increased kVp

The effect of increasing the x-ray tube potential on the perceived image quality in mobile chest radiographs was evaluated by comparison of images taken at the standard kVp setting (85 to 90 kVp, depending on patient size) and images taken with a tube potential that was 15 kVp higher than the original setting (100 to 105 kVp) on Day 4. The Exposure Index generated by the Kodak CR was used to determine the mAs required for the various patients with the goal of matching the Exposure Index of the original image. The mAs values were decreased approximately 40% when the kVp was increased by 15 kVp.

Table 5-35 Image quality ratings for the heart region of clinical mobile chest CR images acquired at decreased kVp (-10 kVp) on Day 2

Adjusted Techniques		Expo-sure Index	Radiologist							Average Image Rating
kVp	mAs	Index	1	2	3	4	5	6	7	Rating
80	5	1830	3	4	3	2	3			3.0
80	5	1830	3	2	2	2	2			2.2
80	5	1770	2	2	3	2	3	3	2	2.4
80	5	1770	4	3	3	4	4	4	3	3.6
80	6.4	1980	3	3	3	4	3			3.2
80	6.4	1820	3	4	4	4	4	2	3	3.4
80	6.4	1790	2	3	2	2	3	3	2	2.4
85	6.4	2050	4	3	2	2	4			3.0
85	6.4	1970	3	3	3	4	3	4	2	3.1
85	6.4	1820	3	3	4	2	2	2	2	2.6
85	6.4	1800	2	3	3	2	3	4	2	2.7
85	6.4	1760	3	2	3	2	2	2	1	2.1
Average rating for radiologist			2.9	2.9	2.9	2.7	3.0	3.0	2.1	2.8

Table 5-36 summarizes both the technique factors used and the corresponding decreases in entrance air kerma and effective dose when the kVp was increased. For dose calculations the patient thicknesses were assumed to be 20 cm for average-sized patients (initial kVp of 85 kVp) and 30 cm for large patients (initial kVp of 90 kVp). Corresponding patient masses were assumed to be 70.9 kg and 130 kg, as previously described. The effective dose to patients decreased by ~7% with the use of higher kVps. Entrance air kerma values, indicators of breast dose, decreased by ~16% for all patients with use of a higher kVp.

Table 5-36 Summary of increased-kVp technique changes used on Day 4 and the resultant entrance air kerma and effective doses to patients

Number of Patients	Initial kVp	Initial mAs	Entrance air kerma (μGy)	Effective Dose (μSv)	Adjusted kVp	Adjusted mAs	Entrance air kerma (μGy)	Effective Dose (μSv)
1	85	2.5	265	59	100	1.6	230	57
5	85	3.2	339	75	100	2	288	71
3	90	4	612	63	105	2.5	489	56

Tables 5-37 and 5-38 show the image quality ratings assigned by each reader to images made at increased kVp for the lung and heart regions, respectively. Images are listed in order of increasing patient size. There were no image quality ratings of 1 or 5 given to images acquired at high kVp, so that no images were deemed "much better" or "much worse". The average lung region rating was 2.9, which means that the image quality was nearly equivalent to the standard-parameter images.

Table 5-37 Image quality ratings for the lung region of clinical mobile chest CR images acquired at increased kVp (+15 kVp) on Day 4

Adjusted Techniques		Exposure Index	Radiologist					Average Image Rating
kVp	mAs		1	2	3	4	5	
100	1.6	1970	3	3	4	2	3	3.0
100	2	2050	3	3	2	2	3	2.6
100	2	1910	4	3	4	4	4	3.8
100	2	1910	3	3	2	2	3	2.6
100	2	1900	3	2	3	2	3	2.6
100	2	1780	2	3	3	2	2	2.4
105	2.5	2050	4	3	2	2	3	2.8
105	2.5	2020	3	3	3	3	3	3.0
105	2.5	1810	4	3	3	3	3	3.2
Average rating for radiologist			3.2	2.9	2.9	2.4	3.0	2.9

The average heart rating was 3.3, demonstrating that the image quality in the heart region was improved for some images with higher kVp. Some heart ratings were as high as 3.8, indicating the images were rated "better" in the heart region by most readers. Ratings were not dependent on patient size.

Table 5-38 Image quality ratings for the heart region of clinical mobile chest CR images acquired at increased kVp (+15 kVp) on Day 4

Adjusted Techniques		Exposure Index	Radiologist					Average Image Rating
kVp	mAs		1	2	3	4	5	
100	1.6	1970	3	2	4	4	4	3.4
100	2	2050	3	3	2	2	3	2.6
100	2	1910	4	3	4	4	4	3.8
100	2	1910	4	3	3	4	4	3.6
100	2	1900	3	2	2	4	4	3.0
100	2	1780	3	4	4	4	4	3.8
105	2.5	2050	3	3	4	3	3	3.2
105	2.5	2020	3	3	2	2	3	2.6
105	2.5	1810	3	3	3	4	4	3.4
Average rating for radiologist			3.2	2.9	3.1	3.4	3.7	3.3

5.7.4 Standard kVp with Grid

The effect of anti-scatter grid use on the perceived image quality in mobile chest radiographs was evaluated by comparison of images taken with and without the use of a 3:1 grid with the standard tube potential setting (90 to 95 kVp). The Exposure Index generated by the Kodak CR was used to determine the mAs required for the various patients with the goal of matching the Exposure Index of the original image. The mAs values were increased by a factor of 2-2.5 when the 3:1 grid was used on Day 3. Table 5-39 summarizes the technique factors used and the corresponding increases in entrance air kerma and effective dose when the anti-scatter grid was used. For dose calculations, the patient thicknesses were assumed to be 20 cm for average-sized patients (initial kVp of 90 kVp) and 30 cm for large patients (initial kVp of 95 kVp), with corresponding patient masses of 70.9 kg and 130 kg, respectively. Because the kVp was not adjusted, the effective dose and entrance air kerma values are directly related to the increase in the

mAs used to produce the image. Both the dose and the entrance kerma for average-sized patients increased by a factor of ~2.3 with the use the 3:1 grid. For large-sized patients, both quantities increased by a factor of approximately 2.5.

Table 5-39 Summary of increases in mAs with anti-scatter grid used on Day 3 and the resultant entrance air kerma and effective doses to patients

Number of Patients	Initial kVp	Initial mAs	Entrance air kerma (μGy)	Effective Dose (μSv)	Adjusted kVp	Adjusted mAs	Entrance air kerma (μGy)	Effective Dose (μSv)
2	90	3.2	375	87	90	6.4	750	174
1	90	4	469	109	90	8	937	217
1	90	4	469	109	90	10	1172	272
2	95	4	682	73	95	10	1704	182
2	95	5	852	91	95	12	2045	218

Tables 5-40 and 5-41 show the image quality ratings assigned by each reader to the lung and heart regions of images acquired with the 3:1 anti-scatter grid. Images are listed in order of increasing patient size. Out of 112 ratings for both lung and heart regions, there were six (three for each region) scores of 5 given, which corresponds to an image which is "much better" than the original. No images were considered "much worse". The average lung region rating was 3.5, with very little variation among radiologists. The rating indicates that there was some improvement noted in the lung region with the use of an anti-scatter grid.

The image quality rating in the lung region had some dependence on patient size; however, there was variation among individual patients. The larger patient image average rating was 3.7, while the average-sized patient average was 3.35. The average heart rating was 3.1, indicating that the image quality in the heart region for all patients was not affected much by the use of the anti-scatter grid. Certain individual images were much

improved. One image received an average heart rating of 4.1, demonstrating that the

image was rated "better" in the heart region by most readers.

Table 5-40 Image quality ratings for the lung region of clinical mobile chest CR images
acquired with the use of the 3:1 grid on Day 3

Adjusted Techniques		Expo-sure	Radiologist							Average Image Rating
kVp	mAs	Index	1	2	3	4	5	6	7	
90	6.4	1750	4	4	2	4	4	4	4	3.7
90	6.4	1710	4	3	2	2	4	2	4	3.0
90	8	1690	3	3	2	4	3	3	3	3.0
90	10	1940	4	4	5	4	3	3	3	3.7
95	10	2130	4	4	4	4	4	3	4	3.9
95	10	1800	4	4	5	4	4	5	4	4.3
95	12	1960	3	3	3	4	4	4	4	3.6
95	12	1970	3	3	3	2	3	4	3	3.0
Average rating for radiologist			3.6	3.5	3.3	3.5	3.6	3.5	3.6	3.5

Table 5-41 Image quality ratings for the heart region of clinical mobile chest CR images
acquired with the use of the 3:1 grid on Day 3

Adjusted Techniques		Expo-sure	Radiologist							Average Image Rating
kVp	mAs	Index	1	2	3	4	5	6	7	
90	6.4	1750	4	3	2	3	4	4	5	3.6
90	6.4	1710	4	3	4	4	4	4	4	3.9
90	8	1690	2	2	3	2	3	3	2	2.4
90	10	1940	2	3	2	2	3	2	2	2.3
95	10	2130	3	4	2	4	3	3	4	3.3
95	10	1800	4	3	3	5	5	4	5	4.1
95	12	1960	2	2	4	2	4	2	2	2.6
95	12	1970	3	2	4	2	3	2	2	2.6
Average rating for radiologist			3.0	2.8	3.0	3.0	3.6	3.0	3.3	3.1

5.7.5 Increased kVp with Grid

The effect of using an anti-scatter grid with increased x-ray beam tube potential (+15 kVp) on the perceived image quality in mobile chest radiographs was evaluated on Day 5. Images made with use of an anti-scatter grid and increased x-ray tube potential were compared for image quality with images taken with the standard technique. The mAs values were also increased by ~63% to match the Exposure Index generated by the Kodak CR to the Exposure Index of the original non-grid, original-kVp image.

Table 5-42 summarizes the technique factors used and the corresponding increases in entrance air kerma and effective dose with use of an anti-scatter grid and increased kVp. For dose calculations the patient thicknesses were assumed to be 20 cm for average-sized patients (initial kVp of 85 or 90 kVp) and 30 cm for large patients (initial kVp of 95 kVp). Corresponding patient masses were assumed to be 70.9 kg and 130 kg. Effective dose to the patient increased by a factor of 2.3 with use of a higher kVp and an anti-scatter grid. This increase in dose is the similar in magnitude to the dose increase needed when the anti-scatter grid was used with the standard kVp. For example the initial techniques of 95 kVp and 5 mAs resulted in an effective dose of 91 μSv. The corresponding standard kVp, grid techniques resulted in an effective dose of 218 μSv, while the increased kVp, grid techniques resulted in a somewhat lower (~5%) effective dose of 208 μSv. Entrance air kerma values increased by a factor of 2.0, which is slightly less than the increase (~2.3) needed with grid use at the standard kVp. Therefore, use of a higher kVp with grid decreased dose to the breast about 15%, as compared to the standard kVp with grid.

Table 5-42 Summary of radiographic techniques with anti-scatter grid used on Day 5 and the resultant entrance air kerma and effective doses to patients

Number of Patients	Initial kVp	Initial mAs	Entrance air kerma (μGy)	Effective Dose (μSv)	Adjusted kVp	Adjusted mAs	Entrance air kerma (μGy)	Effective Dose (μSv)
1	85	2.5	265	59	100	4	575	143
2	85	3.2	339	75	100	5	719	179
1	90	4	469	109	105	6.4	959	245
3	95	4	682	73	110	6.4	1391	166
2	95	5	852	91	110	8	1739	208

Tables 5-43 and 5-44 show the image quality ratings assigned by each reader to the lung and heart regions of images acquired with the 3:1 anti-scatter grid and increased kVp. Images are listed in order of increasing patient size. The average lung region rating was 3.1 and the average heart region rating was 3.2, which indicates that there was very little improvement noted in these regions with the use of an anti-scatter grid at a higher kVp. Some individual images were rated much higher. For example, the image for the smallest patient had an average heart rating of 4.2, indicating the image quality in the heart region was considered "better" than the image acquired without a grid at the original kVp, for that image.

Table 5-45 summarizes the image quality rating results for individual readers and each adjustment of imaging parameters. The highest score given by each radiologist varied in value from 3.3 to 3.7 based on his or her criteria used for comparing images. High scores, including the highest score given and values within 0.1, are highlighted in bold type in Table 5-45. It is notable that the lung region of the image acquired at the original kVp using an anti-scatter grid received high scores from each radiologist.

Table 5-43 Image quality ratings for the lung region of clinical mobile chest CR images acquired with an anti-scatter grid and increased kVp (+15 kVp) on Day 5

Adjusted Techniques		Exposure Index*	Radiologist					Average Image Rating
kVp	mAs		1	2	3	4	5	
100	4	2100	4	2	4	3	3	3.2
100	5	2240	4	3	4	3	3	3.4
100	5	2020	4	2	2	4	4	3.2
105	6.4	2160	4	3	2	2	3	2.8
110	6.4	1950	3	3	2	2	2	2.4
110	6.4	2100	4	3	4	4	3	3.6
110	6.4	1870	2	3	2	2	4	2.6
110	8	2000	3	3	4	3	3	3.2
110	8	2220	4	3	3	4	3	3.4
Average rating for radiologist			3.6	2.8	3.0	3.0	3.1	3.1

* Calibration was performed before this date which increased Exposure Indices by ~180.

Table 5-44 Image quality ratings for the heart region of clinical mobile chest CR images acquired with an anti-scatter grid and increased kVp (+15 kVp) on Day 5

Adjusted Techniques		Exposure Index*	Radiologist					Average Image Rating
kVp	mAs		1	2	3	4	5	
100	4	2100	4	3	4	5	5	4.2
100	5	2240	4	3	3	2	3	3.0
100	5	2020	4	2	2	4	4	3.2
105	6.4	2160	3	3	2	2	2	2.4
110	6.4	1950	3	3	2	2	2	2.4
110	6.4	2100	4	3	4	3	4	3.6
110	6.4	1870	3	2	3	2	4	2.8
110	8	2000	4	3	4	4	3	3.6
110	8	2220	4	3	4	4	3	3.6
Average rating for radiologist			3.7	2.8	3.1	3.1	3.3	3.2

* Calibration was performed before this date which increased Exposure Indices by ~180.

Table 5-45 Average score for different parameters by reader.

Chest region	Parameter adjusted	Sample size n	Average Score for Reader						
			1	2	3	4	5	6	7
lung	kVp lowered by 10 kVp	12	3.3	2.9	**3.3**	2.7	3.3	3.3	2.5
	kVp raised by 15 kVp	9	3.2	2.9	2.9	2.4	3.0		
	Grid used at same kVp	8	**3.6**	**3.5**	**3.3**	**3.5**	**3.6**	**3.5**	**3.6**
	Grid used at high kVp	9	**3.6**	2.8	3.0	3.0	3.1		
heart	kVp lowered by 10 kVp	12	2.9	2.9	2.9	2.7	3.0	3.0	2.1
	kVp raised by 15 kVp	9	3.2	2.9	3.1	**3.4**	**3.7**		
	Grid used at same kVp	8	3.0	2.8	3.0	3.0	**3.6**	3.0	3.3
	Grid used at high kVp	9	**3.7**	2.8	3.1	3.1	3.3		

CHAPTER 6
DISCUSSION

6.1 Phantom Validity

Two phantoms were developed for use in this study. The ABC phantom was

developed to simulate an average chest for chest radiography with uniform regions to

allow measurements of interest in this research. An anthropomorphic phantom was used

as the standard for the development of this phantom. The second phantom, the LBC

phantom, was developed to simulate a large patient for chest radiography; patient-based

criteria were used as the standard for development.

6.1.1 The ABC Phantom

Mean pixel value measurements were made for the ABC phantom and an

anthropomorphic chest phantom in order to ensure that the gross transmittance properties

of the phantoms were similar. The mean pixel values in the lung and heart regions were

very similar (pixel value difference < 66, indicating exposures within 16%) for both the

anthropomorphic chest phantom and the ABC phantom. The mean pixel value in the

subdiaphragm region was lower for the ABC phantom than it was for the

anthropomorphic phantom. The results indicate that there is more exposure reaching the

imaging plate and therefore less attenuation in the subdiaphragm region of the ABC

phantom than the anthropomorphic chest phantom. Because the subdiaphragm region is

not considered critical by radiologists in the review of chest exams, this region was

included in order to provide histogram variability for correct CR processing and to

simulate scatter from a patient. Because of the similarities in the critical regions (lung and heart) for mean pixel values, the ABC phantom was considered to be adequate for the purposes of this research without further modification.

The adequacy of the ABC phantom with respect to scatter was then assessed for chest radiography by comparing S/P values for the ABC phantom with the anthropomorphic phantom to ensure that the scattering properties of the phantoms were similar. S/P measurements showed that the ABC phantom and the anthropomorphic chest phantom were relatively scatter-equivalent in all three regions. However, as shown in Figure 5-2, values of S/P for the anthropomorphic phantom had a larger negative slope as a function of lead beam-stop diameter (0.48, 0.79, 0.95 and 1.9 cm). The areas of the phantoms that were analyzed with ROI measurements increased as the beam-stop diameter increased, because a larger ROI size was possible. Therefore, the S/P values for the ABC phantom had much less variability with beam-stop diameter due to the uniformity of the ABC phantom regions. Data from the 0.48 cm-diameter beam stop were more similar and were used for phantom comparison. For aid in discussion, the S/P values for the lung and heart regions of the two phantoms using the 0.48-cm lead beam stop are summarized in Table 6-1.

The S/P values increased with kVp for both phantoms. The S/P values for the ABC phantom were somewhat higher in the lung region (an average of 27%), somewhat lower in the subdiaphragm (an average of 15%) region and well-matched for the heart region (an average difference of 3%), as compared to the values for the anthropomorphic phantom. The average S/P for the lung region of the ABC phantom was found to be 1.6,

while the average value of S/P, over all kVps tested for the heart region of the ABC

phantom, was found to be 5.4.

Table 6-1 Summary of S/P values obtained with the 0.48-cm beam stop for the ABC and
the anthropomorphic chest phantom

kVp	Lung Region			Heart Region		
	ABC Phantom	Anthropo-morphic Phantom	S/P difference	ABC Phantom	Anthropo-morphic Phantom	S/P difference
60	1.38	0.99	0.39	4.31	5.15	-0.84
80	1.50	1.12	0.38	5.22	5.26	-0.04
100	1.73	1.28	0.45	5.98	5.47	0.51
120	1.79	1.50	0.29	5.97	6.14	-0.17
Average S/P difference			0.38			-0.14

Although the S/P values in the lung region were higher for the ABC phantom than

for the anthropomorphic chest phantom, the differences between the values remained

approximately constant at 0.38±0.06 over the kVp range. Therefore, the difference

between the phantoms would not introduce significant variability over the range of kVps

of interest. S/P values in the heart region from the two phantoms were very similar, with

an average difference in values of 0.14±0.48 over the kVp range. The S/P values in the

subdiaphragm region showed the greatest variability, with an average difference of

0.85±0.17; however, as explained previously, this region was not of concern for clinical

chest imaging and was included because of necessity for CR processing of chest

radiographs.

The S/P ratios measured for the heart region of the ABC phantom were similar in

magnitude and kVp response to those measured by Tucker *et al.* (35). The heart region of

the ABC phantom contains 15 cm of acrylic and 0.41 cm of aluminum. As shown in

Table 6-1, S/P ratios measured in the heart region with a 0.48-cm beam stop were 5.2, 6.0 and 6.0 for 80, 100 and 120 kVp, respectively. These S/P values are similar to and about 15% lower (due to zero-area extrapolation) than the values measured by Tucker *et al.* for a 15 cm thick acrylic phantom. Tucker *et al.* measured zero-area beam stop S/P values of 5.5, 6.8 and 7.1 when their phantom was imaged using x-ray tube potentials of 70, 100 and 120 kVp, respectively.

Values of SDF in the heart region of the ABC phantom compared well with published results of Yip *et al.*, who measured the SDF in a 20-cm water phantom with a 0.6-cm beam stop. Yip measured values with a CR phosphor to be 0.18, 0.15, 0.14 and 0.13 at 60, 80, 100 and 120 kVp, respectively. Using the equation for SDF given in Section 3.2 and the S/P values for the heart region of the ABC phantom with the 0.48-cm beam stop, SDF values were calculated for each kVp. The resultant SDF values were 0.19, 0.16, 0.14 and 0.14, which closely resemble those of Yip *et al.* (37).

6.1.2 The LBC Phantom

The pixel values in three regions of the LBC phantom were compared with pixel values from a sample of images of large clinical patients to ensure that the gross transmittance properties of the LBC phantom were similar to those of a large patient. The averages of the regional (lung, heart and subdiaphragm) mean pixel values from 14 large patient images were chosen to be the target values used to create the LBC phantom. The resultant mean pixel values in the three regions were similar to the average of the large patient pixel values. The differences in pixel value between the large patient images and the LBC phantom in the lung and heart regions were less than 50, which corresponded to exposure differences of less than 11%. Because of the similarities in the critical regions

for mean pixel values, the LBC phantom was considered to be adequate for the purposes of this research without further modification.

6.1.3 Low Contrast Disks

The ABC and LBC phantoms were then used for assessment of the SNR in the three regions. These evaluations first required determining the relevant sizes (thickness) of low contrast disks for use as test objects with the two phantoms. Acrylic and aluminum low contrast disks were used to produce the signal for SNR measurements. The disk materials, acrylic and aluminum, were chosen because of their similarities in attenuation properties to tissue and bone, respectively. Attenuation coefficients and effective atomic numbers are listed for these materials in Table 4-3 of Section 4.2.

A disk diameter of 1.9 cm was used for all low contrast disks because of geometric considerations. Images of a disk with this diameter could be measured with an ROI that covered 63% of the disk area without non-uniformity effects due to focal spot size and edge effects due to disk thickness. A geometric analysis of the contributions of focal spot size and edge effects to a disk located furthest from the central beam in the subdiaphragm region was performed and discussed in Section 4.2.

The threshold thicknesses of acrylic and aluminum disks for each chest region were determined by SNR measurement. The SNRs were measured in each region of the ABC and LBC phantoms as the disk thicknesses were varied. Disk visibility was also rated, based on the visual detection of the edge of each disk. The disk visibility was found to be directly related to the SNR measured. A visibility rating of 4, which corresponded to 75% edge visibility, was chosen as the threshold level for a disk to be visible. An SNR level of 3.5 was found to correspond to this visibility rating of 4. The disk thickness that

produced an SNR closest to 3.5 was therefore chosen as the thickness to be used for further SNR experiments.

This method provided a disk thickness for each region and each disk material that was clinically useful by simulating low contrast pathology, i.e., acrylic simulated nodules in the lung and aluminum simulated vertebral bodies in the mediastinum (heart). Acrylic disk thicknesses used in the lung region were 4 mm and 10 mm in the ABC and LBC phantoms, respectively. Aluminum disk thicknesses used in the heart region were 4 mm and 18 mm in the ABC and LBC phantoms, respectively. These thicknesses represented low contrast pathologic conditions that could reasonably be detected in these regions.

6.2 Image Quality and Dose

The effects of changes in imaging parameters on image quality and phantom dose were evaluated by each individual parameter. The effects of x-ray tube potential (kVp), x-ray beam filtration and use of an anti-scatter grid are discussed in the following subsections.

6.2.1 kVp Effects on Image Quality and Dose

The effect of kVp on SNR in mobile chest radiographs for the phantoms imaged by CR was evaluated by performing SNR measurements as the kVp was varied from 60 to 120 kVp. The relative-kVp SNR results from the ABC phantom averaged over several measurements using different CR systems, both with and without an 8:1 grid, are listed in Table 6-2 for discussion purposes. Similar relative results for the LBC phantom are listed in Table 6-3. These values allow generalization of the effects of kVp on SNR measurements of CR images.

Table 6-2 Summary of relative-kVp SNR results for different kVps in the ABC phantom

kVp	SNR $_{kVp}$/SNR $_{80 kVp}$			
	Lung Region + Acrylic Disk		Heart Region + Aluminum Disk	
	Grid	No grid	Grid	No grid
60	1.08	1.19	1.32	1.29
80	1.00	1.00	1.00	1.00
100	0.99	1.01	0.88	0.92
120	0.89	1.02	0.77	0.98
% change (60 to 120 kVp)	-16%	-14%	-42%	-25%

Table 6-3 Summary of relative-kVp SNR results for different kVps in the LBC phantom

kVp	SNR $_{kVp}$/SNR $_{80 kVp}$			
	Lung Region + Acrylic Disk		Heart Region + Aluminum Disk	
	Grid	No grid	Grid	No grid
60	1.21	1.31	1.10	1.42
80	1.00	1.00	1.00	1.00
100	0.77	0.84	0.83	0.96
120	0.79	0.84	0.71	0.95
% change (60 to 120 kVp)	-35%	-36%	-35%	-37%

In general, the use of a lower kVp improved the disk SNR in the phantom when the exposure indicator was held constant by increasing the mAs. In the lung region of the ABC phantom, the change in SNR for an acrylic disk was small, approximately 15%, as the kVp was increased from 60 to 120 kVp. This result agrees with the measurements described in Section 3.3 of Chotas *et al.*, who found a 15% decrease in measured SNR values of acrylic disks in an average-sized lung phantom with an increase in kVp from 60 to 120 kVp (40). For the aluminum disk in the heart region of the ABC phantom, the change in disk SNR over the range of 60 to 120 kVp was larger (-25% without the grid and -42% with the grid).

The increased amount of scattered radiation in the heart region as compared with the lung region contributed to the greater dependence of disk SNR on kVp in the heart region. S/P measurements of the ABC phantom in these regions showed that the S/P values in the heart region were approximately 3.4 times the S/P values in the lung region (average S/P of 5.4 as compared with 1.6, respectively). S/P values showed some dependence on kVp, most notably for the heart region in the low-energy range. For example, the S/P ratios in the heart region increased 20% from 60 to 80 kVp and 15% from 80 to 100 kVp, while there was no difference between S/P ratios at 100 kVp and 120 kVp. For the lung, the increases were 9% and 15% for the first two intervals and only 3% for the highest kVp interval.

Another contributing factor to the larger change in SNR with kVp in the heart region is the disk material. The probability of photoelectric interactions is highly dependent, not only on the atomic number of the interacting material $\sim Z^3$, but also on the photon energy (E^{-3}). The atomic number of aluminum (Z=13) is higher than acrylic (Z_{eff}=6.5), and therefore, the attenuation coefficient of aluminum is higher at low energies where the photoelectric effect is predominant.

For the LBC phantom, in both the lung and heart regions, the overall decrease in SNR for low contrast disks was approximately 36% as the kVp was increased from 60 to 120 kVp. The LBC phantom was thicker than the ABC phantom in both the lung and heart regions, which greatly increased the incidence of scattering interactions. The contribution of the photoelectric effect and disk material (Z) was therefore smaller, and there was no difference in SNR evident between the lung and heart regions with the LBC phantom as there was with the ABC phantom. The relationships of the changes in SNR to

changes in beam energy, however, were different for grid and non-grid images. These values were similar to the findings for the ABC phantom in the heart region, where the scatter was greater, but not the lung region, where the scatter conditions were less similar.

For images of both phantoms acquired without an anti-scatter grid, the dependence of SNR on tube potential was greater as the kVp changed from 60 to 80 kVp than at the higher kVps tested. Without the grid, the SNR values were relatively independent of kVp from 80 to 120 kVp for the ABC phantom in both regions and for the LBC phantom in the heart region. For the LBC phantom in the lung region, there was also a drop in SNR between 80 and 100 kVp, but not between 100 and 120 kVp.

For images acquired with the grid in the heart region of both the ABC and LBC phantoms, there were small decreases in SNR values over each increasing kVp interval. For example, in the heart region of the LBC phantom, the SNR decreased 15% with each 20 kVp increase.

The SNR improved an average of 22% for the ABC phantom and 28% for the LBC phantom when the kVp was lowered from 80 kVp to 60 kVp. The same change in tube potential caused an average increase in effective dose to the phantom of 24% for the ABC phantom and 52% for the LBC phantom, when effective doses were calculated using the method developed by Gkanatsios and Huda (52, 53).

The amount of increase in effective dose with use of a lower tube potential was also dependent on other imaging parameters. The average increase in dose as the tube potential was lowered from 80 kVp to 60 kVp for the ABC phantom was half that (12%) for the high filtration condition and nearly double (40%) for the low filtration condition. The increase in effective dose to the LBC phantom when the kVp was lowered from 80 to

60 kVp was greater with the use of the 8:1 grid (62%) than without (43%). The increase in effective dose to the LBC phantom when the kVp was lowered from 80 to 60 kVp was smaller with increased aluminum filtration (52%-grid and 37%-no grid) and larger with the low filtration condition (74%-grid and 48%-no grid). It is important to consider all of these parameters in conjunction with one another, and their interrelations are described in a later section.

The MTF was measured for the lung and heart regions of the ABC phantom only. The MTFs in the heart and lung regions were equivalent at all kVps tested with one exception. The MTF in the lung region was lower at 60 kVp compared with other x-ray tube potentials because of an artifact introduced into the measurement process by the processing of the CR image. The kVp has no effect on the MTF of the phantom CR image.

6.2.2 Filtration Effects on Image Quality and Dose

When the filtration was changed by ±1 mm of aluminum, the amount of filtration in the x-ray beam had little effect on the SNR of CR images, and in comparison to kVp and grid changes, the impact of filtration was the least. Evidence of changes in SNR measurements as a function of beam quality was inconclusive. There was some evidence that low beam filtration improved the SNR values for the ABC phantom in isolated cases. For example, the relative-filtration SNR values for aluminum disks in the heart region of the ABC phantom that were measured with the Kodak CR showed an improvement of about 17% with the low filtration condition.

MTF values were measured with the ABC phantom only and did not vary much with changes in x-ray beam filtration. In the lung region the MTF was somewhat lower

with the use of a lower beam quality x-ray unit because of an artifact introduced into the measurement process by the processing of the CR image; however, in the heart region the MTF was equivalent for all filtration conditions. Because neither the MTF nor the SNR had consistent changes relative to the amount of aluminum filtration in x-ray units used for CR imaging of the chest, these findings indicated that filtration should not be changed solely on the basis of image quality.

Changes in the amount of added aluminum filtration (± 1 mm) in the x-ray beam had the least effect of any parameters tested on the effective dose to the phantoms as well. The largest change in effective dose with filtration for the ABC phantom was of the order of 20% for images acquired with the 8:1 anti-scatter grid at 60 kVp. Most changes in effective dose as a function of filtration were smaller. The average change in effective dose with 1 mm less filtration, including data from both phantoms with and without a grid was ~1.4%.

6.2.3 Grid Effects on Image Quality and Dose

The relative-grid SNR results were calculated for the lung and heart regions of both the ABC and LBC phantoms. Because the relative results were approximately independent of kVp and CR system used (average variance only 0.14), the results were averaged over several replicate measurements on different CR systems. The average values are listed in Table 6-4 and allow generalization of the effects of grid use on SNR measurements of CR images.

Relative-grid SNR results showed that all SNR values improved with the use of an anti-scatter grid. As expected, improvements were greater for the thicker regions that

produced more scatter (i.e., heart), and in these regions the SNR ratios improved most

with the 8:1 grid and least with the 3:1 grid.

Table 6-4 Summary of relative-grid SNR results for different grids for both the ABC and the LBC phantom

Grid Ratio	SNR $_{grid}$/SNR $_{no\ grid}$			
	ABC Phantom		LBC Phantom	
	Lung Region + Acrylic Disk	Heart Region + Aluminum disk	Lung Region + Acrylic Disk	Heart Region + Aluminum disk
8:1 [1]	1.26	2.02	2.55	3.84
4:1 [2]	1.40	1.60	2.80	3.38
3:1 [2]	1.62	1.51	1.90	1.96

[1] 41 lines/cm
[2] 33 lines/cm

S/P ratios were measured in the lung and heart regions of the ABC phantom to be

~1.5 and 5, respectively. The relative SNR improvement was calculated from the

equation given in Section 4.10, $\dfrac{1+\left(S/P\right)}{1+\left(S/P\right)T}$, where T was the fractional transmission

through an ideal grid. For an S/P value of 5, as in the heart region of the ABC phantom,

the relative SNR improvement was $\dfrac{6}{1+5T}$. Using the fractional transmission values for

ideal grids that were presented in Figure 1-19 of Section 1.5, the calculated relative-grid

SNR values in the heart region of the ABC phantom for ideal grids with ratios of 3:1, 4:1

and 8:1 were found to be 3, 3.4 and 4, respectively. The experimentally-determined

relative-grid SNR values in the heart region of the ABC phantom were almost exactly

half the ideal values, demonstrating that the grids used attenuated the beam and that the

relationship between relative SNR values and grid ratio followed expected trends.

Ideal relative-grid SNR values for the lung region of the ABC phantom, which

produced much less scatter than the heart region, were found to be 1.9, 2.0 and 2.2 for

3:1, 4:1 and 8:1 grids, respectively. These values did not vary much with grid ratio. The experimentally-determined values, 1.6, 1.4 and 1.3, were also similar to each other in value. However, the greater improvement was seen with the lowest grid ratio grid. This result is likely to be related to the grid type in addition to the grid ratio, rather than the grid ratio alone. The 3:1 grid has very low attenuation properties for primary radiation due to the carbon-fiber interspacing material, thus making it closer to "ideal".

The MTF was measured with the ABC phantom with and without use of the 8:1 grid. Unlike the improvements seen in SNR with use of an anti-scatter grid, the MTF of CR phantom images did not improve with grid use. Table 5-31 demonstrated that the area under the MTF curves measured with and without the grid were essentially equivalent.

Large improvements in SNR were measured with anti-scatter grids but with an associated increase in dose. Table 6-5 lists the effective dose to the ABC and LBC phantom with and without use of 3:1 and 8:1 anti-scatter grids. Effective doses to the phantoms increased by a factor of 3 to 6 when an anti-scatter grid was used. In low scatter body regions, like the lung region of the chest, SNR improvements with use of a 3:1 grid were similar to improvements achieved with use of an 8:1 grid; however, the 3:1 grid required roughly half (0.5-0.6) the phantom dose required with the use of an 8:1 grid.

Table 6-5 Summary of effective dose calculations at 80 kVp for the ABC and LBC phantoms with matched CR exposure indicators with and without grid-use

Phantom	Effective Dose (μSv)		
	No grid	3:1 grid[1]	8:1 grid[2]
ABC	29	74	115
LBC	50	151	303

[1] carbon fiber interspace material, 41 lines/cm
[2] aluminum interspace material, 33 lines/cm

The effects of the adjustment of kVp, filtration and use of an anti-scatter grid on the SNR, MTF and effective dose in phantom studies were measured. Table 6-6 summarizes the average change in image quality or dose to the phantom measured with the indicated adjustment of imaging parameter when compared with standard techniques (80 kVp, no grid, no added aluminum filtration).

Table 6-6 Average change in image quality or dose measured with the ABC phantom (LBC phantom) with the given adjustment in imaging parameter from standard imaging techniques

Parameter adjustment	Effect on SNR	Effect on MTF (area under the MTF curve)	Effect on phantom dose
60 kVp	×1.3 (×1.4)	**	×1.4 (×1.5)
100 kVp	** (×0.9)	**	×0.9 (×0.9)
3:1 grid	×1.6 (×2.0)	*	×2.6 (×3.0)
8:1 grid	×1.6 (×3.2)	**	×4.0 (×6.0)
Low beam filtration (-1)	inconsistent	inconsistent	× 0.8 (**)

* Not measured
** Change was less than 10% from measurements with standard imaging techniques

Comparison of these results with the original hypotheses showed that as expected the use of a lower kVp improved SNR for both the ABC and LBC phantom with an increase in effective dose. However, the use of lower beam filtration did not improve the SNR as hypothesized. It was predicted that grid use would improve the SNR for the LBC phantom only and would not have much of an effect on the SNR of the ABC phantom. SNR measurements showed that the use of a grid improved SNR for both the ABC and LBC phantom with an increase in phantom dose. The 3:1 grid improved SNR by a factor of 1.6 and 2.0 for the ABC and LBC phantoms, respectively, with an increase in phantom dose by a factor of 2.6 and 3.0. For the ABC phantom, the 8:1 grid provided no greater improvement in SNR than the 3:1 grid but required a phantom dose which was 1.5 times

greater. For the LBC, the improvement in SNR measured with the 8:1 grid was 1.6 times greater than the improvement measured with the 3:1; however, the phantom dose with the 8:1 grid was twice the phantom dose with the 3:1 grid. As expected, none of the parameter adjustments affected the MTF by more than 10%.

6.3 Clinical Evaluation

The results of the phantom studies indicated possible changes in imaging parameters based on SNR and phantom dose, including decreasing the kVp and using a grid. It was important to evaluate the impact of these potential changes in the clinical environment. The phantom measurements were performed with fixed x-ray units that had a higher beam quality than the mobile x-ray unit. As discussed in Section 4.3, the HVL of the mobile x-ray unit at a partiular kVp was similar to the HVL for the fixed units at a kVp that was 20 kVp lower. Mobile chest radiographs in the SICU for an average-sized patient were performed with a kVp of 90 kVp. In order to predict the effect of changes in kVp on the SNR of a clinical image performed with a mobile unit at 90 kVp, phantom SNR measurements performed with the fixed unit at ~70 kVp were examined for comparison. Phantom SNR measurements were performed at 60 and 80 kVp, and significant improvement in SNRs occurred when the kVp was decreased from 80 to 60 kVp on the fixed x-ray unit.

Because SNR improved with a change from 80 to 60 kVp with the fixed unit(s), the first clinical evaluation involved a decrease in peak tube potential. In addition, because SNR improved for the phantom with the use of a grid, the clinical evaluation also involved the use of a grid. The clinical evaluation study was performed with mobile chest

radiography with the Kodak 400 CR system for SICU patients in Shands at UF who received mobile chest radiography on at least a daily basis. The initial evaluation was performed over a 3-day period, with the Day 1 technique factors selected independently for 12 patients by the technologist. On Day 2, the x-ray tube potential was decreased by 10 kVp (with a 30-60% increase in mAs); on Day 3, a 3:1 anti-scatter grid was used without a change in tube potential (with an increase in mAs by a factor of 2.3). Radiologists compared the image quality in the lung and heart regions of the adjusted-parameter images with the images of the same patients acquired with standard techniques. A 5-point rating scale, from 5 (much better) to 1 (much worse), was used to indicate the perceived image quality of the adjusted-parameter image compared with the original image. A score of 3 indicated that the image quality of the adjusted-parameter image was equivalent to the original image in that region.

The initial study compared decreasing the kVp and using the 3:1 grid independently. As expected, grid use improved image quality in the lung region. The results of the initial study did not have the expected finding with a 10 kVp decrease in kVp. Unlike the phantom evaluation predictions for improvement in SNR, no improvement in image quality was perceived with the lower kVp for patients (perhaps related to the increased time and patient motion). Furthermore, because the exposure indicator was held constant, there was a cost in terms of patient dose (+17%) and exposure time (+30-60%) with the reduced kVp.

To investigate a possible savings in patient dose and exposure time, an additional evaluation was performed with the kVp increased by 15 kVp, both without and with the use of the 3:1 anti-scatter grid (Days 4 and 5, respectively).

Table 6-7 lists the average scores assigned by different radiologists to the lung and heart regions of clinical images acquired with adjusted imaging parameters. The highlighted scores include the highest average scores given by each radiologist. Most average ratings were not very different from 3.0, i.e., equivalent to the original images.

Table 6-7 Average image quality ratings for different parameters by reader, with a 3.0 rating indicating equivalent image quality

Chest region	Parameter adjusted	Sample size n	Average Score for Reader							
			1	2	3	4	5	6	7	Avg
Lung	-10 kVp	12	3.3	2.9	**3.3**	2.7	3.3	3.3	2.5	3.0
	+15 kVp	9	3.2	2.9	2.9	2.4	3.0			2.9
	Same kVp, grid	8	**3.6**	**3.5**	**3.3**	**3.5**	**3.6**	**3.5**	**3.6**	**3.5**
	+15 kVp, grid	9	**3.6**	2.8	3.0	3.0	3.1			3.1
Heart	-10 kVp	12	2.9	2.9	2.9	2.7	3.0	3.0	2.1	2.8
	+15 kVp	9	3.2	2.9	3.1	**3.4**	**3.7**			**3.3**
	Same kVp, grid	8	3.0	2.8	3.0	3.0	**3.6**	3.0	3.3	3.1
	+15 kVp, grid	9	**3.7**	2.8	3.1	3.1	3.3			3.2

All the radiologists agreed that there was an improvement in image quality in the lung region of clinical images acquired with a 3:1 grid, with an average score of 3.5. The heart region of the same images did not improve as much as a group (average score 3.1). When the 3:1 anti-scatter grid was used at the original kVp, the mAs was increased by a factor of 2.3 to produce comparable Kodak Exposure Indices to images produced with standard techniques. Increasing the mAs by a factor of 2.3 also caused a comparable increase in the effective dose to the patient and the exposure time compared with original imaging techniques.

For the heart region the most improvement was noted when the kVp was increased by 15 kVp while the mAs was decreased by 37% to maintain a comparable Exposure Index. The average score was 3.3. The effective dose to the patient decreased

by ~7% with the use of a higher kVp (and lower mAs), compared with doses at the standard kVp. For example, the effective dose to an average patient (20 cm thick, 70.9 kg) was calculated to be 75 µSv with 85 kVp and 71 µSv with 100 kVp. The entrance air kerma also decreased by about 16% with the use of a higher kVp, which indicated that breast dose could by lowered with the utilization of higher kVp techniques. The relevant SNR phantom measurements in the heart region showed very little decrease in SNR with increased kVp above 80 kVp without the use of the anti-scatter grid. For example, the average relative-kVp SNR at 120 kVp was 0.98 for the heart region of the ABC phantom and 0.95 for the heart region of the LBC phantom. The improvements in image quality noted in clinical images were possibly due to the 37% reduction in exposure time, which correspondingly reduced patient motion, although no motion artifacts were obvious.

6.3.1 Effect of kVp on Perceived Image Quality

When the kVp was decreased from 80 kVp to 60 kVp for SNR measurements made with the ABC and LBC phantoms with the fixed unit, the SNR measurements increased by 20-40%. No corresponding improvement in image quality was noted when clinical images were acquired when the peak tube potential for the mobile unit was decreased by 10 kVp. The mAs settings and therefore the exposure times were increased 30-60% when the kVp was decreased by 10 kVp. Perhaps the increase in patient motion may have had a negative impact and couteracted the predicted positive effects on SNR.

The effect of kVp on perceived image quality is summarized in Table 6-8. In the lung region there was very little change in perceived image quality with change in kVp. In the heart region there was a small improvement in perceived image quality with increasing kVp. The reduction in patient dose (~7%) and exposure time (~40%)

associated with the increase in kVp, with no detrimental effects on image quality, indicated that increased kVp could be considered for mobile chest radiography with CR. The reduction in breast dose, especially important for AP chest exams, is indicated by the entrance air kerma which was reduced by ~16% with a 15 kVp increase in kVp.

Table 6-8 Average image quality ratings as a function of kVp

Parameter adjusted	Lung	Heart
-10 kVp	3.0	2.8
Standard kVp	3.0	3.0
+15 kVp	2.9	3.3

6.3.2 Effect of Grid Use on Perceived Image Quality

In phantom measurements, the use of a 3:1 grid without changing kVp improved SNR values measured with both phantoms by a factor of 1.5 to 2. The measured SNRs also increased when the grid was used at a higher kVp by a factor of 1.3 to 1.8. The SNR improvements were generally lower with the 3:1 grid than the SNR improvements measured with an 8:1 grid for the phantoms. SNR improvements for the 8:1 grid ranged from 1.3 to 3.8, with corresponding phantom effective dose increases of 3.5-6×. In the lung region of the ABC phantom the 3:1 grid improved SNR values as well as the 8:1 grid with much less dose to the phantom (8:1 dose/3:1 dose =1.5).

Unlike the 8:1 grid, which greatly improved SNR values in high-scatter conditions, the 3:1 grid improved SNR values in high and low-scatter conditions similarly for both phantoms and both the lung and heart regions (ranging from 1.5-2.0). This fact would explain why there was little relationship between patient size and the perceived image quality improvement when the 3:1 grid was used for clinical mobile chest radiographs.

The effect of a 3:1 grid, with an increase in mAs by a factor of ~2.3, on perceived image quality is summarized in Table 6-9. In the lung region there was a significant improvement in perceived image quality with use of the grid at the standard kVp, and no improvement seen with use of the grid at increased kVp. In the heart region there was only a slight improvement in perceived image quality with grid use. Both the effective dose to the patient and the entrance air kerma, which indicates breast dose, increased by a factor of ~2.3 with the use of the 3:1 grid. The significant improvement in SNR in the lung region with grid use indicated that a 3:1 grid could be considered for mobile chest radiography with CR with an increase in patient dose.

Table 6-9 Average image quality ratings as a function of kVp and grid

Parameter adjusted	Lung	Heart
Standard kVp, no grid	3.0	3.0
Standard kVp, grid	3.5	3.1
+15 kVp, grid	3.1	3.2

CHAPTER 7
SUMMARY AND CONCLUSIONS

7.1 Summary

Even with the emergence of sophisticated imaging technologies like CT and MRI, x-ray projection radiography remains the most common radiological procedure. Chest radiography, in particular, is the radiological exam performed most frequently. Screen-film systems have been used as the image receptor in projection radiography for decades. The screen-film systems currently in use were selected because of their image capture abilities, namely, detection efficiency and x ray-to-light conversion characteristics.

The demands of various clinical applications impose requirements on the x-ray spectra and scatter conditions that can be utilized with these screens to generate images with appropriate spatial resolution and contrast characteristics for the required diagnostic tasks. Projection radiography parameters that affect the x-ray spectra and the amount of scattered radiation reaching the phosphor are critical to the quality of the images produced with these screen-film systems. These parameters include x-ray tube potential, added aluminum filtration and the use of an anti-scatter grid.

Radiography of the chest involves technical difficulties due to the wide range of tissue attenuation in the thorax. This variation in attenuation of the chest presents difficulty in obtaining a screen-film chest image that is optimized for both the lung and the mediastinum. Mobile chest radiography has added further technical challenges to the production of a quality chest image. In particular, mobile exams are performed on

seriously ill patients at their bedsides with a mobile x-ray unit rather than in the radiology department with fixed equipment. The absence of automatic exposure control often results in inconsistent film densities in mobile screen-film radiography. Consistency is especially important for mobile chest imaging because of the reliance on image comparisons to assist in monitoring patient conditions.

Screen-film projection radiographs are displayed on viewboxes for radiologist interpretation. The displayed images present patterns corresponding to differences in x-ray transmission through the patient's body. Radiologists interpret these patterns using a free search method to recognize patterns that are abnormal.

Computed radiography (CR), a new approach to x-ray projection radiography, is now widely available. CR utilizes photostimulable phosphors to capture the x-ray image. Upon exposure to x rays, photostimulable phosphors trap incident energy that is later emitted as visible light upon stimulation with a scanning laser beam. The light emitted is collected by a photomultiplier tube, which generates an electronic signal that is digitized to create the digital image file.

The photostimulable phosphor most commonly used in computed radiography is barium fluorohalide, doped with europium. Photostimulable phosphors have different responses to incident x-ray spectra than screen-film combinations. The absorption efficiency of photostimulable phosphors is highest just above the K-edge of barium (37.4 keV). The K-edge of barium is approximately 13 keV lower than the K-edge of gadolinium (50.2 keV), the primary absorbing element in rare-earth intensifying screens. CR phosphors are, therefore, more efficient at detecting a lower range of x-ray energies

than rare-earth intensifying screens. Therefore, imaging parameters used for screen-film radiography may not be ideal for CR.

Because of its digital nature, CR separates the image capture function from the image storage and image display functions. The appearance of CR images is not determined solely by the radiation exposure and characteristic curve of a screen-film detector but may be modified by manipulation of the digital CR data. The interactions of transmitted x-ray beam spectra with the CR phosphor determine the intrinsic image quality in terms of SNR and MTF achievable in CR.

CR has the potential to overcome the difficulties in optimally displaying the widely varying tissue attenuations in the chest that are associated with screen-film chest imaging. Not only does CR offer the opportunity for window and level adjustments in the image display as a whole, CR also offers image processing capabilities such as dynamic range compression (DRC), in which the mapping of output pixel values and consequently the contrast are changed in a region of an image with a particular density level. In this way the contrast in the low-density mediastinum region of a chest CR image can be enhanced without overenhancing the lung fields (7). Other advantages of CR for mobile chest radiography are the wide latitude and automatic gain control capabilities that compensate for inappropriate exposures and maintain consistent image density levels.

Despite all the advantages of CR, radiologists at Shands at UF have noticed frequent suboptimal chest images, most notably with mobile chest radiographs of large patients. An investigation of the effect of imaging parameters, such as x-ray tube potential, added aluminum filtration and use of anti-scatter grids on measurements of image quality, was performed in order to identify the parameters that improve image

quality in mobile chest radiographs. The effects of these parameters on effective dose and entrance air kerma, as an indicator of breast dose, to average and large patients was determined, in order to evaluate the risks involved with changes in imaging parameters.

Image quality measurements involved SNR and MTF measurements of two sizes of acrylic and aluminum block chest phantoms, ABC and LBC, that were developed with x-ray attenuation and scatter properties similar to the chest of an average and a large patient. The phantoms contained uniform regions simulating the lung, heart and subdiaphragm regions of the chest.

SNR measurements were made with 1.9-cm diameter acrylic and aluminum disks in the three chest regions of the phantoms. Analysis of the SNR results obtained with the acrylic disk in the lung region simulated lung nodules and the aluminum disk in the heart region simulated vertebral bodies behind the mediastinum. Acrylic and aluminum are similar in attenuation properties to tissue and bone, respectively.

Image quality results of these disks showed an improvement in SNR of 10-40% with a decrease in kVp from 80 to 60 kVp. The relationship between SNR and kVp at higher kVp levels, 80 to 120 kVp, was not as significant, showing decreases in SNR of 0-26% across this 40 kVp range. The SNR improved an average of 22% for the ABC phantom and 28% for the LBC phantom when the kVp was lowered from 80 kVp to 60 kVp. The same change in tube potential caused an average increase in effective dose to the phantom of 24% for the ABC phantom and 52% for the LBC phantom. Entrance air kerma to the phantoms, which is an indicator of breast dose, increased by 69% for the ABC phantom and 110% for the LBC phantom as the kVp was decreased from 80 to 60 kVp.

The use of an 8:1 anti-scatter grid increased SNR values by a factor of 1.3 to 2.6 in the lung region and increased SNR values by a factor of 2.0 to 3.8 in the heart region. When a grid ratio of 3:1 was used, the relative improvements in SNR were 1.6 to 1.9 in the lung region and 1.5 to 2.0 in the heart region. Effective doses to the phantoms increased by a factor of 3 to 6 when an anti-scatter grid was used. In low scatter body regions, like the lung region of the chest, SNR improvements with use of a 3:1 grid were similar to improvements achieved with use of an 8:1 grid; however, the 3:1 grid required roughly half (0.5-0.6) the phantom dose required with use of an 8:1 grid.

There was not a consistent change in SNR with changes in added aluminum filtration. Use of a low beam quality x-ray unit (-1) resulted in increases in SNR as great as 18% and decreases in SNR as great as 31%. Use of a high beam quality x-ray unit (+1) also resulted in mixed SNR response, with increases of 12 % and decreases of 15% measured.

The MTF at spatial frequencies greater than 0.5 cycles/mm was measured using an approximation to the square wave response function. The MTF of a system using CR is affected by exam-dependent image processing, such as unsharp mask enhancement, which can produce MTF values which are greater than 1. MTF values were therefore normalized to the system response at the lowest measured frequency. The measured MTFs of the CR did not change significantly with adjustments in imaging parameters. The effects of scatter on the MTF were apparent, as the MTF measured in the lung region was greater than the MTF measured in the heart region. Scatter in the phantom also contributed a position-dependent decrease in MTF for the non-grid heart region images.

The results of the phantom studies indicated some possible changes in imaging parameters which improved the measured SNR, including decreasing the kVp and the use of a grid. It was important to evaluate the impact of these potential changes in the clinical environment. A clinical evaluation study was performed with mobile chest CR images of SICU patients at Shands at UF utilizing a Kodak 400 CR system with technique settings, including kVp and use of a grid, which differed from those typically used for the same patients. Seven radiologists compared the image quality in the lung and heart regions of the adjusted-parameter images with the images of the same patients acquired with typical techniques. A score of 3 indicated that the image quality of the adjusted-parameter image was equivalent to the original image in that region.

The initial study compared decreasing the kVp and using the 3:1 grid independently. As expected, grid use improved image quality in the lung region. The results of the initial study did not have the expected finding with a 10 kVp decrease in kVp. Unlike the phantom evaluation predictions for improvement in SNR, no improvement in image quality was perceived with the lower kVp for patients. Furthermore, because the exposure indicator was held constant, there was a cost in terms of effective dose to the patient (+17%) and exposure time (+30-60%) with the reduced kVp.

To investigate a possible savings in patient dose and exposure time, an additional evaluation was performed with the kVp increased by 15 kVp, both without and with the use of the 3:1 anti-scatter grid (Days 4 and 5, respectively).

The clinical evaluation showed that small improvements (30-40%) in SNR of mobile chest radiographs performed with CR did not translate to improvements in

perceived image quality. Larger improvements in measured SNR (50-100%) did correlate with increased image quality in some instances, namely, in the lung region. The lack of correlation of small changes in measured SNR with perceived image quality in clinical images might be due to the negative impact of patient motion as exposure times are increased. Another possible explanation is that the ability of CR to separate the functions of image capture, processing and display might compensate for small differences in the image quality of the captured image.

7.2 Conclusions

The goal of this dissertation was to perform a systematic study of the effects of several x-ray parameters on mobile chest radiography image quality for 3 CR systems. The parameters included: x-ray tube potential, beam filtration and the use of anti-scatter grids. Because these parameters affected dose, it was necessary to study the effects on patient doses. Three different CR systems (Kodak, AGFA and Fuji) were evaluated for mobile chest radiographic image quality in terms of SNR and MTF. The resultant image quality measurements were evaluated to provide clinically useful guidelines for mobile chest radiography image acquisition with CR. The applicability of these results to the image quality of clinical images was determined by an evaluation of perceived image quality changes in mobile chest images performed with various techniques.

For the phantoms, SNR results for the acrylic disk in the lung region, representing lung nodules, and the aluminum disk in the heart region, representing vertebral bodies, improved with lower x-ray tube potential and use of an anti-scatter grid. No consistent changes in SNR were observed with adjustment of the amount of added aluminum

filtration. MTF results demonstrated very little variation with changes in imaging parameters.

The clinical evaluation showed that small improvements in SNR (30-40%) measured with phantoms with the use of a lower kVp did not translate to improvements in perceived image quality of clinical mobile chest radiographs performed with CR. In addition the use of a higher kVp, which had a negative effect on phantom SNR measurements, did not have a detrimental effect on perceived image quality in clinical mobile chest images. This finding indicates that the higher kVp settings could be used clinically to perform mobile chest exams with a savings in patient dose and a reduction in exposure times.

Improvements in SNR of 50-100% were measured with phantoms with the use of a 3:1 anti-scatter grid. The use of the 3:1 grid for clinical mobile chest images improved the perceived image quality, most notably in the lung region. There was a corresponding increase in effective dose to the patient and entrance air kerma, indicating breast dose, by a factor of 2.3, when the 3:1 anti-scatter grid was used.

Based on the results of the SNR measurements of the block phantoms and the clinical evaluation of patient mobile chest radiographs summarized above, the use of a 3:1 parallel anti-scatter grid is recommended for mobile chest radiography with CR at Shands at UF. This type of grid can be used without some of the technical problems associated with the use of 8:1 focused grids currently in use at Shands at UF, including the occurrence of artifacts from patient motion and grid cut-off. The benefit of improved image quality at the cost of increased patient dose that results from grid use, is justified,

especially for the more severely ill patients who commonly undergo mobile chest radiography in the intensive care unit.

Some obstacles to the institution of this recommendation exist including the number of grids required and the cost of this type of grid, which is substantial. The use of grids also requires an additional step in the exam procedure for technologists, and grid use may be difficult with some soft hospital beds often used for patients who require extended stays.

If grid use is not feasible, it is recommended that kVp settings used for mobile chest radiographs be increased from the typical kVp settings that are currently used. There are many benefits to use of a higher kVp in mobile chest radiography, without loss of image quality. Use of a higher kVp allows a reduction in mAs while maintaining the exposure to the imaging plate. Therefore, the patient dose, both effective dose and breast dose, are reduced. The exposure time is also reduced which might correspond to reduced patient motion.

GLOSSARY OF ABBREVIATIONS

ABC – average block chest
AEC – automatic exposure control
AP – anteroposterior
CDRH - Center for Devices and Radiological Health
CR – computed radiography
DRC – dynamic range compression
HR – high resolution
HVL – half-value layer
ICRP – International Commission on Radiological Protection
kerma – kinetic energy released in matter
kVp – peak x-ray tube potential (peak kV)
LBC – large block chest
LSF – line spread function
LUT – look-up table
MICU – medical intensive care unit
MTF – modulation transfer function
MUSICA – multiscale image contrast amplification
NCRP – National Council on Radiation Protection and Measurement
OD – optical density
PA – posteroanterior
PACS – picture archival communication system
PMT – photomultiplier tube
ROI – region-of-interest
SDF – scatter degradation factor
SICU – surgical intensive care unit
SID – source-to-image receptor distance
SNR – signal-to-noise ratio
S/P – scatter-to-primary ratio
UF – University of Florida

REFERENCE LIST

(1) Exposure of the U.S. population from diagnostic medical radiation. Burr WW, Moseley RD, Jr., Mettler FA, Jr., editors. 100, 1-76. 1989. Bethesda, MD, National Council on Radiation Protection and Measurements. Recommendations of the National Council on Radiation Protection and Measurements.

(2) Gamsu G. Imaging the pleura. In: Margulis AR, Gooding CA, editors. Diagnostic Radiology 1989. Philadelphia, PA: J.B.Lippincott Company, 1989: 505.

(3) Bushberg JT, Seibert JA, Leidholdt EMJ, Boone JM. Projection radiography. The Essential Physics of Medical Imaging. Baltimore, MD: Williams and Wilkins, 1994: 139-168.

(4) Rottenberg GT, Chin RJ, Allen CM, Maggs P, Kessel D. Portable chest radiology in intensive care: a comparison of a new dual characteristic film-screen system (InSight) incorporating a flexible grid with a standard film-screen system. Clin Radiol 1996; 51(7):494-498.

(5) Glazer HS, Muka E, Sagel SS, Jost RG. New techniques in chest radiography. Radiol Clin North Am 1994; 32(4):711-729.

(6) Hendee WR. Characteristics of the human visual system. Hendee WR, Trueblood JH, editors. AAPM Medical Physics Monograph No. 22, 197-211. 1993. Madison, WI, Medical Physics Publishing. Medical Physics Monograph No.22.

(7) Vuylsteke P, Dewaele P, Schoeters E. Optimizing computed radiography imaging performance. The Expanding Role of Medical Physics in Diagnostic Imaging, 3-41. 1997. 1997 AAPM International Summer School.

(8) Ter-Pogossian MM. Interaction of x-rays with matter. The Physical Aspects of Diagnostic Radiology. Hagerstown, Maryland: Harper and Row, Publishers, Inc., 1967: 64-95.

(9) Evans RD. Radiative collisions of electrons with atomic nuclei. The Atomic Nucleus. Malabar, Florida: Robert E. Krieger Publishing Company, Inc., 1985: 600-610.

(10) Evans RD. Stopping of electrons by thick absorbers. The Atomic Nucleus. Malabar, Florida: Robert E. Krieger Publishing Company, Inc., 1985: 611-631.

(11) Evans RD. Photoelectric effect and pair production. The Atomic Nucleus. Malabar, Florida: Robert E. Krieger Publishing Company, Inc., 1985: 695-710.

(12) Evans RD. Compton scattering and absorption. The Atomic Nucleus. Malabar, Florida: Robert E. Krieger Publishing Company, Inc., 1985: 672-694.

(13) Ter-Pogossian MM. The radiologic examination- the x-irradiation and the generation of information. The Physical Aspects of Diagnostic Radiology. Hagerstown, Maryland: Harper and Row, Publishers, Inc., 1967: 150-184.

(14) Hubbell JH. Photon mass attenuation and energy-absorption coefficients from 1 keV to 20 MeV. International Journal of Applied Radiation and Isotopes 1982; 33(11):1269-1290.

(15) 1990 Recommendations of the International Commission on Radiological Protection. Smith H, editor. 60, 1-201. 1991. Elmsford, NY: Pergamon Press Inc. Annals of the ICRP.

(16) Brateman L. Radiation safety considerations for diagnostic radiology personnel. Radiographics 1999; 19(4):1037-1055.

(17) Bushberg JT, Seibert JA, Leidholdt EMJ, Boone JM. Generation and control of x rays. The Essential Physics of Medical Imaging. Baltimore, MD: Williams and Wilkins, 1994: 65-108.

(18) Curry TS, III, Dowdey JE, Murry RC, Jr. Filters. Christensen's Physics of Diagnostic Radiology. Philadelphia, PA: Lea and Febiger, 1990: 87-92.

(19) Ter-Pogossian MM. The radiographic image. The Physical Aspects of Diagnostic Radiology. Hagerstown, Maryland: Harper and Row, Publishers, Inc., 1967: 241-292.

(20) Ter-Pogossian MM. The radiologic examination- the radiologic image and the retrieval of information. The Physical Aspects of Diagnostic Radiology. Hagerstown, Maryland: Harper and Row, Publishers, Inc., 1967: 185-240.

(21) Bogucki TM, Trauernicht DP, Kocher TE. Characteristics of a storage phosphor system for medical imaging. [6], 1-35. 1995. Rochester, NY, Kodak Health Sciences. Technical and Scientific Monographs.

(22) Bushberg JT, Seibert JA, Leidholdt EMJ, Boone JM. Image quality. The Essential Physics of Medical Imaging. Baltimore, MD: Williams and Wilkins, 1994: 109-137.

(23) Barnes GT. Digital x ray image capture with image intensifier and storage phosphor plates: imaging principles, performance and limitations. Hendee WR, Trueblood JH, editors. AAPM Medical Physics Monograph No. 22, 25-48. 1993. Madison, WI, Medical Physics Publishing. Medical Physics Monograph No.22.

(24) Webb WR. The solitary pulmonary nodule. In: Margulis AR, Gooding CA, editors. Diagnostic Radiology 1989. Philadelphia, PA: J.B.Lippincott Company, 1989: 479-490.

(25) Alfidi RJ, MacIntyre WJ, Haaga JR. The effects of biological motion on CT resolution. Am J Roentgenol 1976; 127(1):11-15.

(26) Margulis AR, Marco RP, Lipsy RD. Impact of new technology on radiologic practice. In: Margulis AR, Gooding CA, editors. Diagnostic Radiology 1989. Philadelphia, PA: J.B.Lippincott Company, 1989: 3-5.

(27) Ingenito EP, Drazen JM. Mechanical ventilatory support. In: Fauci AS, Braunwald E, Isselbacher KJ, Wilson JD, Martin JB, Kasper DL et al., editors. Harrison's Principles of Internal Medicine. New York, NY: McGraw-Hill Companies, Inc., 1998: 1486-1490.

(28) Kato H. Photostimulable phosphor radiography:design considerations. Seibert JA, Barnes GT, Gould RG, editors. AAPM Medical Physics Monograph No. 20, 731-770. 1991. Washington D.C., AAPM.

(29) Huda W, Rill LN, Bruner AP. Relative speeds of Kodak computed radiography phosphors and screen-film systems. Med Phys 1997; 24(10):1621-1628.

(30) Sorenson JA, Phelps ME. Radiation detectors. Physics in nuclear medicine. Philadelphia, PA: W.B. Saunders Company, 1987: 56-83.

(31) Miettunen RH, Korhola OA. The effect of digital unsharp-mask filtering on the signal-to-noise ratio in computed radiography. Eur J Radiol 1991; 13(3):225-228.

(32) Cowen AR, Workman A, Price JS. Physical aspects of photostimulable phosphor computed radiography. Br J Radiol 1993; 66(784):332-345.

(33) Conway BJ, Butler PF, Duff JE, Fewell TR, Gross RE, Jennings RJ, Koustenis GH, McCrohan JL, Rueter FG, Showalter CK. Beam quality independent attenuation phantom for estimating patient exposure from x-ray automatic exposure controlled chest examinations. Med Phys 1984; 11(6):827-832.

(34) Conway BJ, Duff JE, Fewell TR, Jennings RJ, Rothenberg LN, Fleischman RC. A patient-equivalent attenuation phantom for estimating patient exposures from automatic exposure controlled x-ray examinations of the abdomen and lumbo-sacral spine. Med Phys 1990; 17(3):448-453.

(35) Tucker DM, Souto M, Barnes GT. Scatter in computed radiography. Radiology 1993; 188(1):271-274.

(36) Yip KL, Whiting BR, Kocher TE, Trauernicht DP, Van Metter RL. Understanding the relative sensitivity of radiographic screens to scattered radiation. Med Phys 1996; 23(10):1727-1737.

(37) Yip KL, Whiting BR, Kocher TE, Trauernicht DP, Van Metter RL. Sensitivity of radiographic screens to scattered radiation. SPIE 1995; 2432:33-52.

(38) Dobbins JT, Rice JJ, Beam CA, Ravin CE. Threshold perception performance with computed and screen-film radiography: implications for chest radiography. Radiology 1992; 183(1):179-187.

(39) Giger ML, Doi K. Investigation of basic imaging properties in digital radiography. 3. Effect of pixel size on SNR and threshold contrast. Med Phys 1985; 12(2):201-208.

(40) Chotas HG, Floyd-CE J, Dobbins JT, Ravin CE. Digital chest radiography with photostimulable storage phosphors: signal-to-noise ratio as a function of kilovoltage with matched exposure risk [see comments]. Radiology 1993; 186(2):395-398.

(41) Miettunen RH, Korhola OA. The effect of scatter reduction on the signal-to-noise ratio in computed radiography. Eur J Radiol 1991; 12(3):167-170.

(42) Huda W, Bissessur K. Effective dose equivalents, HE, in diagnostic radiology. Med Phys 1990; 17(6):998-1003.

(43) Jing Z, Huda W. Image contrast and noise in computed radiography. Poster: 1993 Annual AAPM Meeting, Charlottesville, VA.

(44) Sanada S, Doi K, Xu XW, Yin FF, Giger ML, MacMahon H. Comparison of imaging properties of a computed radiography system and screen-film systems. Med Phys 1991; 18(3):414-420.

(45) Dobbins JT, III, Ergun DL, Rutz L, Hinshaw DA, Blume H, Clark DC. DQE(f) of four generations of computed radiography acquisition devices. Med Phys 1995; 22(10):1581-1593.

(46) Coltman JW. Specification of imaging properties by response to a sine wave input. J Opt Soc Am 1954; 44(6):468.

(47) Droege RT, Morin RL. A practical method to measure the MTF of CT scanners. Med Phys 1982; 9(5):758-760.

(48) Hillen W, Schiebel U, Zaengel T. Imaging performance of a digital storage phosphor system. Med Phys 1987; 14(5):744-751.

(49) Tucker DM, Rezentes PS. The relationship between pixel value and beam quality in photostimulable phosphor imaging. Med Phys 1997; 24(6):887-893.

(50) Giger ML, Doi K. Investigation of basic imaging properties in digital radiography. I. Modulation transfer function. Med Phys 1984; 11(3):287-295.

(51) Appendix A: Specifications. FCR5000 Operation Manual. Fuji Photo Film Co.,Ltd., 1998: A-1.

(52) Gkanatsios NA, Huda W. Computation of energy imparted in diagnostic radiology. Med Phys 1997; 24(4):571-579.

(53) Huda W, Gkanatsios NA. Effective dose and energy imparted in diagnostic radiology. Med Phys 1997; 24(8):1311-1316.

(54) Ott RL. Inferences about μ_1-μ_2. An Introduction to Statistical Methods and Data Analysis. Belmont, CA: Wadsworth, Inc., 1993: 260-329.

APPENDIX A
TABULATED SNR RESULTS FOR ABC PHANTOM

Table A-1 SNR results for the ABC chest phantom in the lung region

kVp	Grid used	Added Al filtration (mm)	Agfa CR system		Kodak CR system		Fuji CR system	
			Acrylic disk	Aluminum disk	Acrylic disk	Aluminum disk	Acrylic disk	Aluminum disk
60	Yes	-1	4.58	5.14	4.37	4.84	6.06	4.71
80	Yes	-1	4.54	3.65	5.23	4.74	4.72	4.70
100	Yes	-1	4.57	3.31	4.66	2.68	5.35	4.17
120	Yes	-1	4.27	3.24	3.26	1.83	4.23	3.41
60	No	-1	4.38	4.55	4.08	4.84	3.96	4.65
80	No	-1	3.59	3.18	3.34	3.48	3.41	3.05
100	No	-1	3.66	2.68	2.99	3.08	3.86	3.11
120	No	-1	3.39	2.96	3.18	3.05	3.28	2.90
60	Yes	0	4.60	4.16	4.56	4.34		
80	Yes	0	4.17	2.75	4.40	2.68		
100	Yes	0	3.26	2.77	3.61	2.06		
120	Yes	0	3.91	3.12	3.48	2.14		
60	No	0	5.04	4.81	3.31	3.81		
80	No	0	3.72	3.52	2.91	2.67		
100	No	0	3.12	2.44	2.82	2.43		
120	No	0	3.35	2.74	3.17	1.81		
60	Yes	1	4.46	3.95	6.09	5.07		
80	Yes	1	3.16	3.14	4.82	3.67		
100	Yes	1	3.42	2.85	4.01	3.01		
120	Yes	1	3.12	2.70	3.08	2.48		
60	No	1	3.90	4.36	3.05	3.24		
80	No	1	3.43	3.14	3.15	3.27		
100	No	1	3.13	2.71	2.38	1.61		
120	No	1	2.96	2.00	2.83	2.41		

Table A-2 SNR results for the ABC phantom in the heart region

kVp	Grid used	Added Al filtration (mm)	Agfa CR system		Kodak CR system		Fuji CR system	
			Acrylic disk	Aluminum disk	Acrylic disk	Aluminum disk	Acrylic disk	Aluminum disk
60	Yes	-1	8.90	9.91	7.63	8.32	7.58	7.64
80	Yes	-1	8.87	7.69	5.73	6.26	7.24	6.2
100	Yes	-1	8.24	6.92	6.31	5.43	6.23	5.5
120	Yes	-1	7.14	5.69	5.56	4.58	5.28	4.77
60	No	-1	3.99	4.13	3.75	4.12	3.57	4.33
80	No	-1	3.20	3.50	3.18	3.08	3.93	3.59
100	No	-1	3.63	2.96	3.05	2.80	3.84	3.74
120	No	-1	4.04	3.35	3.30	2.95	3.57	3.36
60	Yes	0	9.50	9.87	5.48	5.95		
80	Yes	0	8.34	7.12	6.53	5.30		
100	Yes	0	7.55	6.93	6.51	5.04		
120	Yes	0	6.90	6.65	5.68	4.35		
60	No	0	4.20	4.74	3.54	3.95		
80	No	0	3.63	3.59	2.86	2.58		
100	No	0	3.55	3.21	2.93	2.33		
120	No	0	3.25	2.02	2.28	2.38		
60	Yes	1	9.20	9.40	5.54	6.23		
80	Yes	1	8.53	7.54	5.51	5.20		
100	Yes	1	6.84	5.79	5.57	4.97		
120	Yes	1	7.80	6.29	4.89	4.04		
60	No	1	4.34	4.68	3.63	3.80		
80	No	1	3.30	3.55	3.42	3.12		
100	No	1	3.37	3.06	3.16	2.57		
120	No	1	3.28	2.86	2.90	2.47		

Table A-3 SNR results for the ABC phantom in the subdiaphragm region

kVp	Grid used	Added Al filtration (mm)	Agfa CR system		Kodak CR system		Fuji CR system	
			Acrylic disk	Aluminum disk	Acrylic disk	Aluminum disk	Acrylic disk	Aluminum disk
60	Yes	-1	6.07	6.90	8.29	9.75	7.76	12.44
80	Yes	-1	5.90	5.83	7.23	6.77	7.51	8.95
100	Yes	-1	5.52	5.45	6.35	6.43	8.05	7.20
120	Yes	-1	5.12	4.81	5.84	5.18	6.59	5.65
60	No	-1	3.59	4.35	4.93	5.78	5.63	6.19
80	No	-1	3.27	3.41	4.01	4.23	4.69	4.84
100	No	-1	2.77	2.83	3.70	3.71	4.69	4.35
120	No	-1	3.08	3.04	4.03	3.87	4.86	4.31
60	Yes	0	7.91	8.42	8.89	8.71		
80	Yes	0	6.82	6.76	7.63	7.42		
100	Yes	0	6.48	5.50	7.51	6.65		
120	Yes	0	6.68	5.59	6.75	5.59		
60	No	0	3.89	4.58	4.57	5.34		
80	No	0	3.41	3.59	3.81	4.18		
100	No	0	3.14	3.06	3.48	3.17		
120	No	0	3.09	2.80	2.81	2.61		
60	Yes	1	7.06	8.03	7.87	8.37		
80	Yes	1	6.54	6.84	7.11	7.52		
100	Yes	1	6.53	5.74	6.43	5.75		
120	Yes	1	5.94	3.79	7.01	5.78		
60	No	1	3.69	4.31	4.71	5.50		
80	No	1	3.58	3.31	4.21	4.48		
100	No	1	3.24	2.92	3.60	3.64		
120	No	1	2.63	2.31	3.41	3.35		

APPENDIX B
TABULATED RESULTS FOR LBC PHANTOM

Table B-1 SNR results for the LBC phantom in the lung region

kVp	Grid used	Added Al filtration (mm)	Agfa CR system		Kodak CR system		Fuji CR system	
			Acrylic disk	Aluminum disk	Acrylic disk	Aluminum disk	Acrylic disk	Aluminum disk
60	Yes	-1	11.09	10.61	11.75	11.59	11.85	12.95
80	Yes	-1	8.68	10.84	9.26	7.02	10.28	9.14
100	Yes	-1	5.20	4.20	7.85	6.03	8.49	6.18
120	Yes	-1	8.56	6.20	7.09	5.16	7.74	5.59
60	No	-1	5.41	5.72	3.94	4.64	4.27	3.73
80	No	-1	4.24	3.45	2.91	3.13	3.67	3.00
100	No	-1	3.65	2.94	2.71	1.67	2.82	2.41
120	No	-1	2.53	2.25	2.92	1.80	2.96	2.77
60	Yes	0	8.03	9.03	8.90	10.94		
80	Yes	0	6.65	6.45	9.86	6.93		
100	Yes	0	8.42	5.59	8.32	6.06		
120	Yes	0	6.63	4.50	6.49	4.73		
60	No	0	4.82	4.99	3.39	4.04		
80	No	0	3.80	3.44	3.35	3.27		
100	No	0	3.00	2.28	2.51	2.53		
120	No	0	3.79	2.99	2.86	2.57		
60	Yes	1	8.69	10.00	8.45	10.66		
80	Yes	1	8.50	7.34	8.71	6.43		
100	Yes	1	6.86	6.20	6.44	4.74		
120	Yes	1	6.55	5.27	6.17	4.30		
60	No	1	4.66	4.17	3.46	4.12		
80	No	1	2.80	3.10	3.31	3.19		
100	No	1	3.46	2.93	2.31	2.45		
120	No	1	2.04	2.61	2.73	2.33		

Table B-2 SNR results for the LBC phantom in the heart region

kVp	Grid used	Added Al filtration (mm)	Agfa CR Aluminum disk	Kodak CR Aluminum disk	Fuji CR Aluminum disk
60	Yes	-1	16.33	10.25	11.64
80	Yes	-1	5.76	10.74	9.34
100	Yes	-1	6.12	8.74	8.63
120	Yes	-1	8.76	7.10	7.42
60	No	-1	3.63	2.88	3.8
80	No	-1	2.35	2.03	2.42
100	No	-1	2.10	2.10	2.62
120	No	-1	2.51	1.65	2.25
60	Yes	0	20.73	9.13	
80	Yes	0	10.98	8.54	
100	Yes	0	11.08	8.83	
120	Yes	0	10.00	7.60	
60	No	0	3.02	2.52	
80	No	0	2.96	2.14	
100	No	0	1.36	1.94	
120	No	0	2.63	1.98	
60	Yes	1	19.73	9.41	
80	Yes	1	12.79	8.78	
100	Yes	1	9.59	8.25	
120	Yes	1	9.94	7.23	
60	No	1	1.59	2.45	
80	No	1	2.91	2.08	
100	No	1	2.15	1.98	
120	No	1	2.11	1.19	

Table B-3 SNR results for the LBC phantom in the subdiaphragm region.

kVp	Grid used	Added Al filtration (mm)	Agfa CR Aluminum disk	Kodak CR Aluminum disk	Fuji CR Aluminum disk
60	Yes	-1	9.11	7.27	15.21
80	Yes	-1	7.38	7.08	12.30
100	Yes	-1	3.00	7.80	10.69
120	Yes	-1	5.52	5.78	9.21
60	No	-1	3.05	3.47	4.79
80	No	-1	2.54	2.85	3.79
100	No	-1	2.27	2.74	3.63
120	No	-1	2.22	2.07	3.43
60	Yes	0	10.77	10.00	
80	Yes	0	9.19	8.35	
100	Yes	0	8.25	10.51	
120	Yes	0	7.30	8.58	
60	No	0	3.21	4.17	
80	No	0	2.43	2.77	
100	No	0	2.23	3.28	
120	No	0	2.28	2.25	
60	Yes	1	10.61	10.47	
80	Yes	1	14.54	9.66	
100	Yes	1	7.56	9.87	
120	Yes	1	7.07	8.09	
60	No	1	2.81	4.16	
80	No	1	1.88	2.74	
100	No	1	2.14	3.08	
120	No	1	2.00	2.05	

APPENDIX C
PAIRED T TEST RESULTS FOR ABC PHANTOM

Table C-1 Probability values p that $t \leq t_{0.05}$ from a paired t test, comparing samples of SNR values acquired in the lung region of the ABC phantom under different imaging conditions.

Parameters compared	Sample 1	Sample 2	Agfa ADC Compact		Kodak 400	
			Acrylic disk	Aluminum disk	Acrylic disk	Aluminum disk
kVp	60	80	0.017	0.000095	0.41	0.024
	60	100	0.016	0.00013	0.048	0.000043
	60	120	0.0051	0.00056	0.052	0.0011
	80	100	0.23	0.039	0.0052	0.026
	80	120	0.011	0.092	0.079	0.029
	100	120	0.82	0.66	0.46	0.47
Grid	yes	no	0.016	0.35	0.00064	0.22
Filtration	0	+1	0.033	0.23	0.056 *	0.19 *
	-1	0	0.3	0.012	0.08	0.01
	-1	+1	0.0056	0.015	0.49	0.016

*Indicates negative t value

Table C-2 Probability values p that $t \le t_{0.05}$ from a paired t test, comparing samples of SNR values acquired in the heart region of the ABC phantom under different imaging conditions.

Parameters compared	Sample 1	Sample 2	Agfa ADC Compact		Kodak 400	
			Acrylic disk	Aluminum disk	Acrylic disk	Aluminum disk
kVp	60	80	0.0074	0.004	0.37	0.0031
	60	100	0.017	0.0023	0.35	0.003
	60	120	0.016	0.0029	0.047	0.0042
	80	100	0.21	0.029	0.69	.00098
	80	120	0.19	0.016	0.028	0.022
	100	120	0.69	0.32	0.034	0.1
Grid	yes	no	6.3×10^{-10}	1.9×10^{-8}	7.0×10^{-8}	1.4×10^{-7}
Filtration	0	+1	0.85	0.58	0.55	0.53
	-1	0	0.48	0.99	0.32	0.026
	-1	+1	0.5	0.57	0.1	0.029

*Indicates negative t value

Table C-3 Probability values p that $t \le t_{0.05}$ from a paired t test, comparing samples of SNR values acquired in the subdiaphragm region of the ABC phantom under different imaging conditions.

Parameters compared	Sample 1	Sample 2	Agfa ADC Compact		Kodak 400	
			Acrylic disk	Aluminum disk	Acrylic disk	Aluminum disk
kVp	60	80	0.027	0.00014	0.00056	.0013
	60	100	0.0036	0.00076	0.011	0.01
	60	120	0.00029	0.0025	0.016	0.0099
	80	100	0.0059	0.006	0.0082	0.0077
	80	120	0.014	0.023	0.027	0.0017
	100	120	0.03	0.16	0.41	0.088
Grid	yes	no	6.3×10^{-10}	4.2×10^{-8}	4.6×10^{-9}	2.1×10^{-8}
Filtration	0	+1	0.08	0.13	0.57	0.63
	-1	0	0.015*	0.057*	0.64*	0.32
	-1	+1	0.027*	0.77*	0.98	0.53

*Indicates negative t value

Table D-1 Probability values p that $t \leq t_{0.05}$ from a paired t test, comparing samples of SNR values acquired in the lung region of the LBC phantom under different imaging conditions.

Parameters compared		Agfa ADC Compact		Kodak 400	
Sample 1	Sample 2	Acrylic disk	Aluminum disk	Acrylic disk	Aluminum disk
grid	no grid	6.1×10^{-7}	5.3×10^{-6}	2.1×10^{-8}	7.7×10^{-6}
0	+1	0.66	0.27	0.07	0.05
-1	0	0.48	0.21	0.41	0.99*
-1	+1	0.15	0.34	0.07	0.22
60	80	0.0075	0.015	0.44	0.014
60	100	0.063	0.0047	0.022	0.0054
60	120	0.00092	0.0016	0.028	0.0079
80	100	0.4	0.14	0.0084	0.0012
80	120	0.086	0.036	0.04	0.0023
100	120	0.92	0.92	0.42	.012

*Indicates negative t value

Table D-2 Probability values p that $t \leq t_{0.05}$ from a paired t test, comparing samples of SNR values acquired in the heart region of the LBC phantom under different imaging conditions.

Parameters compared		Agfa CR	Kodak CR
Sample 1	Sample 2	Aluminum disk	Aluminum disk
grid	no grid	2.6×10^{-5}	2.1×10^{-11}
0	+1	0.56	0.27
-1	0	0.072*	0.31
-1	+1	0.14*	0.065
60	80	0.084	0.097
60	100	0.046	0.0078
60	120	0.067	0.0067
80	100	0.16	0.28
80	120	0.72	0.058
100	120	0.30*	0.017

*Indicates negative t value

Table D-3 Probability values p that $t \leq t_{0.05}$ from a paired t test, comparing samples of SNR values acquired in the subdiaphragm region of the LBC phantom under different imaging conditions.

Parameters compared		Agfa CR	Kodak CR
Sample 1	Sample 2	Aluminum disk	Aluminum disk
grid	no grid	1.7×10^{-5}	5.0×10^{-9}
0	+1	0.62*	0.91*
-1	0	0.077*	0.016*
-1	+1	0.13*	0.020*
60	80	0.77	0.007
60	100	0.04	0.25
60	120	0.015	0.00013
80	100	0.14	0.11*
80	120	0.16	0.03
100	120	0.76*	0.0017

*Indicates negative t value

MTF MEASUREMENTS IN THE SUBDIAPHRAGM REGION

Figure E-1 shows the overall modulation transfer function in the subdiaphragm region of the ABC phantom when an 8:1 ratio anti-scatter grid was used. The curves show that the MTF did not change very much with variation of x-ray tube potential, especially at low spatial frequencies. The MTF curve for 60 kVp is somewhat lower than the MTF curves acquired with 80, 100 and 120 kVp.
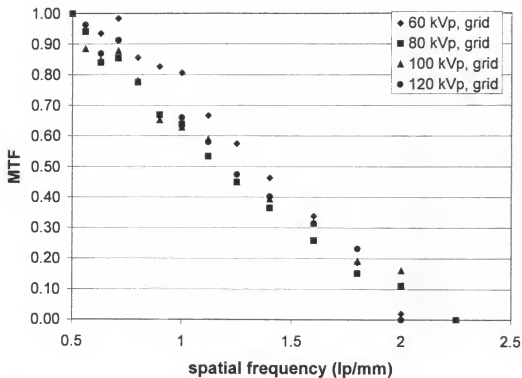
Figure E-1 MTF measured in the subdiaphragm region of the anthropomorphic phantom with use of an anti-scatter grid.

Figure E-2 shows the MTF in the subdiaphragm region measured without use of an anti-scatter grid. The curves again did not change very much with adjustment of kVp. Again, the MTF was lowest at 60 kVp, particularly at higher spatial frequencies, although the difference is small.
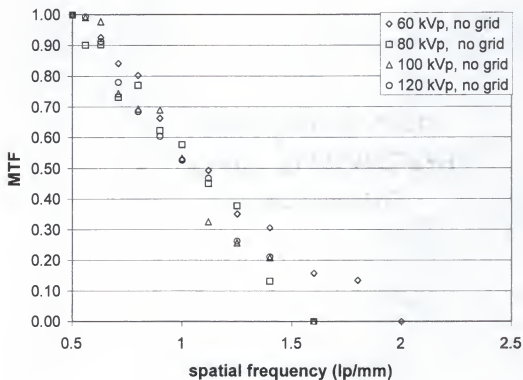
Figure E-2 MTF in the subdiaphragm region measured without use of an anti-scatter grid.

Figure E-3 shows the MTF in the subdiaphragm region as the amount of aluminum filtration was varied. The amount of filtration did not have much effect on the MTF of the CR system. The MTF response in the subdiaphragm region when 1 mm of aluminum filtration was removed from the x-ray beam was slightly lower than the other MTF filtration curves. This is very similar to the MTF response at 60 kVp. Figure E-4

shows the MTF measured in the subdiaphragm region when the ABC phantom was

imaged with 60 and 80 kVp, with and without the use of an anti-scatter grid. The overall

MTF was not affected by the use of an anti-scatter grid.
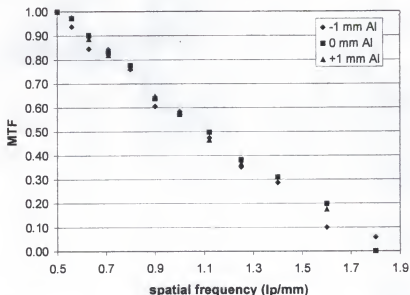
Figure E-3 Modulation Transfer Function in the subdiaphragm region measured
various amounts of added aluminum filtration in the x-ray beam.
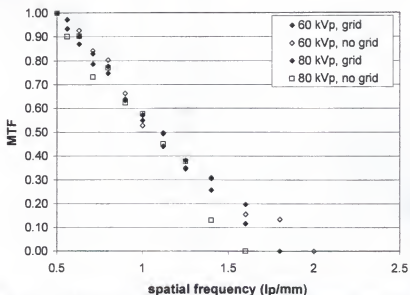
Figure E-4 Modulation Transfer Function in the subdiaphragm region measured with
and without the use of an anti-scatter grid. 60 and 80 kVp data are shown.

BIOGRAPHICAL SKETCH
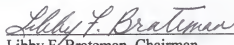
The author, Lynn Neitzey Rill, was born on March 13, 1970, in Washington, D.C., to Sharon and Frank Neitzey, who are both in education. She spent her childhood growing up with her brother and sister in Waldorf, Maryland.

She attended Wake Forest University in Winston-Salem, North Carolina, where she completed her Bachelor of Arts degree in physics in 1991 and her Master of Science in physics in 1993. Her master's thesis project, under the direction of Dr. George Holzwarth, was entitled *The Angle Dependence of DNA Velocity during Pulsed Field Gel Electrophoresis*.

In August of 1994 she began her doctoral studies in the Medical Physics Program of the Department of Nuclear and Radiological Engineering at the University of Florida in Gainesville, Florida. Her primary interest is in diagnostic imaging. She worked as a graduate assistant in the Department of Radiology at Shands Hospital at UF, under the supervision of Dr. Walter Huda until August, 1999. She then began her dissertation work in computed radiography with advisers, Drs. Libby Brateman and Manuel Arreola. Her dissertation topic work focused on improving the image quality of mobile chest images using computed radiography.
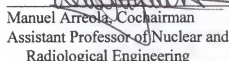
She currently resides in Jacksonville Beach, Florida, with her husband, Matthew Rill, and her two dogs, Shelby and Kamper.

I certify that I have read this study and that in my opinion it conforms to acceptable standards of scholarly presentation and is fully adequate, in scope and quality, as a dissertation for the degree of Doctor of Philosophy.
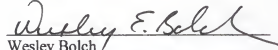
Libby F. Brateman, Chairman
Associate Professor of Nuclear and
 Radiological Engineering

I certify that I have read this study and that in my opinion it conforms to acceptable standards of scholarly presentation and is fully adequate, in scope and quality, as a dissertation for the degree of Doctor of Philosophy.

Manuel Arreola, Cochairman
Assistant Professor of Nuclear and
 Radiological Engineering

I certify that I have read this study and that in my opinion it conforms to acceptable standards of scholarly presentation and is fully adequate, in scope and quality, as a dissertation for the degree of Doctor of Philosophy.

Wesley Bolch
Professor of Nuclear and Radiological
 Engineering

I certify that I have read this study and that in my opinion it conforms to acceptable standards of scholarly presentation and is fully adequate, in scope and quality, as a dissertation for the degree of Doctor of Philosophy.

Shailendra Shukla
Research Assistant Professor of Nuclear
 and Radiological Engineering

I certify that I have read this study and that in my opinion it conforms to acceptable standards of scholarly presentation and is fully adequate, in scope and quality, as a dissertation for the degree of Doctor of Philosophy.
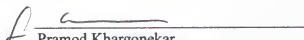
Janice Honeyman
Associate Professor of Radiology

I certify that I have read this study and that in my opinion it conforms to acceptable standards of scholarly presentation and is fully adequate, in scope and quality, as a dissertation for the degree of Doctor of Philosophy.

Irvin Hawkins
Professor of Radiology

This dissertation was submitted to the Graduate Faculty of the College of Engineering and to the Graduate School and was accepted as partial fulfillment of the requirements for the degree of Doctor of Philosophy.

August 2001

Pramod Khargonekar
Dean, College of Engineering

Winfred Phillips
Dean, Graduate School